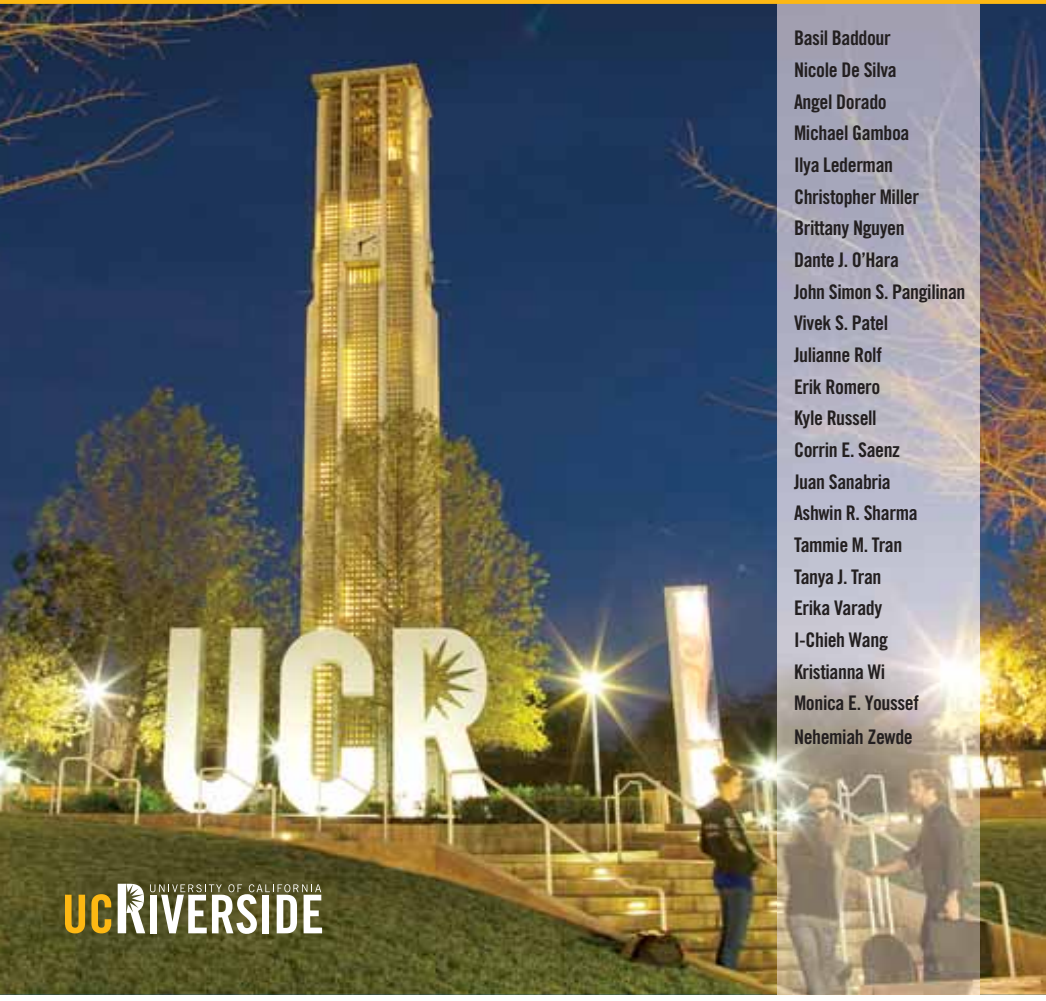University of California, Riverside

Undergraduate Research Journal

Basil Baddour
Nicole De Silva
Angel Dorado
Michael Gamboa
Ilya Lederman
Christopher Miller
Brittany Nguyen
Dante J. O'Hara
John Simon S. Pangilinan
Vivek S. Patel
Julianne Rolf
Erik Romero
Kyle Russell
Corrin E. Saenz
Juan Sanabria
Ashwin R. Sharma
Tammie M. Tran
Tanya J. Tran
Erika Varady
I-Chieh Wang
Kristianna Wi
Monica E. Youssef
Nehemiah Zewde

UNIVERSITY OF CALIFORNIA
UC RIVERSIDE

University of California, Riverside
Undergraduate Research Journal

Table of Contents

From the Administration

Across the sciences, social sciences and humanities, the opportunity to participate in undergraduate research and creative activities can open magical new worlds for students at the University of California, Riverside.

These students have the chance to explore new concepts, investigate complex questions and advance and test their own hunches as they learn the rigor of the scientific method, the creativity of experimental design, the joy of scholarly research and personal expression, and the discipline and hard work of writing. We are proud that by the time they graduate, more than 50 percent of UC Riverside undergraduates will have participated in faculty-mentored research or creative projects.

It is a pleasure to present this year's *Undergraduate Research Journal*, which showcases the academic discoveries and creative endeavors of some of our talented undergraduates. I invite youto share the journeys they detail here. I know you will be inspired, as I am, by the quality of the work they have achieved.

Kim A. Wilcox
Chancellorr

You hold in your hands the eighth annual UC Riverside Undergraduate Research Journal. It provides a selective, peer-reviewed venue featuring the very best faculty-mentored undergraduate research and scholarship on our campus. The peer-review process has been very ably led by our Student Editorial Board, with advice as needed from the Faculty Advisory Board. I would like to thank Veronique Rorive, our director of the Office of Undergraduate Research, for able and timely organizational work that helped to bring this inspiring journal to fruition. Thanks also to Nancy Kameya who assisted in this work.

I want to congratulate the young scholars whose work appears here in. The process of discovery can be filled with excitement but also with frustration, as we search for the golden threads that tie together the ideas we have been pursuing and the findings that have emerged from our work. During this process, we travel a path that no one has been on before. The journal article is the culmination of that process—a formal presentation to our community of peers and mentors of what we found on that journey. Place this volume on your bookshelf. Pull it down occasionally from the shelf to re-read and to remind yourself of the journey you traveled. I wish you many more such journeys in the future.

Best regards,

Steven G. Brint
Vice Provost for Undergraduate Education
Professor of Sociology

First row (front/bottom row): Stephanie Tran, Anissa Gastelum, Danielle Bacon
2nd row: Colette King, Alexandra Villamor, Fallon Fowler
3rd row: Claire Tran, Tina Kim, Winnie Jeng
4th row: Amber Fountain, Victoria Tejera, Ashley Wong
5th row: Scott Manifold, Gabriel Grajeda, Joseph Bulone
6th (top) row: Christopher Miller, Ashwin Sharma, Blake Riser
not pictured: Marzieh Tousi, Michael Turcios

From the Student Editorial Board

It is with great enthusiasm and pride that we present you with Volume VIII of the UCR Undergraduate Research Journal. This undergraduate student peer-reviewed journal reflects the diversity of research and creative activity projects taking place on this campus. We appreciate all of the hard work from our student authors, their faculty mentors, the Student Editorial Board and the Faculty Advisory Board. We thank each of you for your research contributions and your commitment to excellence.
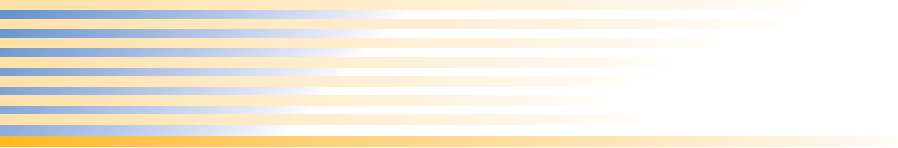
Electrostatic Analysis of Complement Factor D

Basil Baddour, Ronald D. Gorham Jr., and Dimitrios Morikis

Department of Bioengineering

ABSTRACT

The alternative pathway of the complement system is a part of the innate immune system which acts as a persistent line of defense against pathogens. Its activation undergoes an amplification step whose propagation is limited by the cleavage of the C3b-FB complex by complement Factor D (FD). The interaction of FD with the C3b-FB complex is an essential, rate limiting factor to the activation of the alternative pathway. Over-activation of the alternative pathway has been shown to be strongly linked to autoimmune diseases such as dense deposit disease, macular degeneration, and atypical hemolytic uremic syndrome. Here the C3b-FB-FD interaction is analyzed using electrostatic free energy calculations and electrostatic clustering to identify the electrostatic contribution to binding for each charged amino acid in FD. The computational framework AESOP (Analysis of Electrostatic Similarities Of Proteins) was utilized to perform computational alanine scan mutagenesis for all charged residues. Free energy calculations were performed on each mutant and hierarchical clustering was used to group mutants based on their deviation from the parent structure. Results highlight the extent to which charged residues are critical to binding of FD to the C3b-FB proconvertase. Understanding the electrostatic contribution of each charged residue provides insight into FD's unique specificity to Factor B (FB). This analysis aids to further delineate characteristics critical for FD's binding and cleavage, in addition to characterizing differences from other serine proteases. This knowledge is useful for designing FD inhibitors as target therapeutics for autoimmune disease suppression.

Keywords: complement system alternative pathway; factor D; autoimmunity; Poisson-Boltzmann electrostatics; protein design; AESOP.

AUTHOR

Basil Baddour

Department of Bioengineering

Basil Baddour is a fourth year bioengineering student at UCR, and has been doing research in BioMoDeL (Biomolecular Modeling and Design Lab) for two years. He finds his scientific inspiration in the mechanisms of nature and hopes to pursue a PhD investigating plant and other naturally derived proteins as a basis for the development of biomimetic therapeutics.

FACULTY MENTOR

Dimitrios Morikis

Department of Bioengineering

Professor Morikis' work focuses on immune system function and regulation, structure-dynamics-activity/function relations, design of peptides and proteins with tailored properties, structure-based drug discovery, and development of structural bioinformatics and in *silico* diagnostic methods. His research is predominantly computational, with emphasis on molecular dynamics simulations, electrostatic calculations, free energy calculations, pharmacophore modeling, virtual screening, and protein-ligand docking, and has an experimental component, with emphasis on binding and biochemical assays and NMR spectroscopy.

Basil Baddour

INTRODUCTION

Complement Factor D (FD) is a serine protease of the complement system alternative pathway, an essential component of the innate immune system. Inception of the complement system is mediated by the cleavage of the central complement protein, C3, into C3a and C3b. Complement protein C3b, an intermediate activation product, tags pathogen surfaces for elimination by macrophages, and leads to the formation of the membrane attack complex C5b-9, which targets and lyses tagged pathogenic surfaces. In addition, C3b plays a vital role in the activation of the alternative pathway through the formation of convertase enzyme, C3b-Bb, which amplifies C3b production on pathogen surfaces. C3b forms an initial complex with Factor B (FB) which must then be cleaved by FD to form the active convertase, enabling continuation of the pathway until formation of C5b-9 complex, resulting in pathogen lysis and death [3][4][6][8]. Cleavage of FB by FD is the rate limiting step of alternative pathway activation. Over-activation of the alternative pathway has been correlated to autoimmune diseases such as age-related macular degeneration, dense deposit disease, and atypical hemolytic uremic syndrome [26][27]. Previous efforts to create target pharmaceuticals to inhibit FD activity has been proven challenging due to the similarity of FD with other serine proteases [1][2][23]. Recent work has elucidated the molecular structures of the proenzyme form of the alternative pathway C3 convertase, C3b-FB-FD [6]. This structural information has renewed interest in alternative pathway-mediated therapeutic design. Analyzing the electrostatic basis of its interaction and comparing it to that of other common serine proteases can help differentiate its mode of cleavage from other serine proteases. The aim of this work is to understand the electrostatic properties of the C3b-FB-FD interaction through the use of molecular modeling, Poisson-Boltzmann electrostatic calculations, and electrostatic similarity clustering. These results give insight to electrostatic and structural characteristics specific to binding and catalysis of FD to the C3b-FB complex. From this, new approaches can be taken to design pharmaceuticals that specifically target the C3b-FB-FD interaction.

METHODS

Electrostatic properties of proteins play a critical role in long range protein-protein interactions and short range catalytic activity; this was incentive for analyzing the electrostatic contribution of each charged amino acid residues to binding of FD to C3b-FB. This was done through utilization of the AESOP computational framework, which performs alanine scan mutagenesis of all ionizable residues of FB and FD, calculates electrostatic potential using Poisson-Boltzmann electrostatics, and clusters mutants based on their spatial distribution of electrostatic potential. Through analyzing the electrostatic perturbations of mutated residues, the electrostatic contribution of their overall functionality can be assessed [9][10][11].

Preparation of Molecular Structure for In-Silico Computational Analysis: Atomic structure of C3b-FB-FD (PDB ID: 2XWB) was taken from the RCSB website in the form of a protein data bank file (PDB), obtained through X-ray diffraction techniques at 3.49Å resolution. PDB2PQR software was used to assigning partial charges and radii to atoms within the PDB, in addition to adding hydrogen atoms[24][25]. This enables calculation of electrostatic distributions. Prior to computational analysis, PDB structure was modified to improve integrity of the structure. Original structure contains mutation at the active site of FD to enable crystallization, which was corrected by switching back Ala183 to Ser183. Chains A, B, F, J were deleted, leaving Chains C, D, H, I. Chain H is complement FB, Chain I is FD, and Chains C and D, are the two chains of C3b. The crystallographic structure contains missing positional information of residues in flexible surface loops[13][6]. All of the gaps were reconstructed using MODELLER[14][15]. The most critical deficiency in the structure was the missing residue configuration of FB's scissile bond loop, residues 224-239 [6]. This was modeled using a trypsin bound to tryptase inhibitor (PDB ID: 2UUY). Structures were aligned, scissile bond loop of the tryptase inhibitor contained a Lys39 residue in proximity of the active site of FD. This aligned with Lys235 in the sequence of FB. Proximity of Lys39 was used as a keystone to fill in the rest of the gaps. Putative interactions between FB and FD—Glu230 of FB with Arg202 of FD and Arg234

of FB with Asp177 of FD—were manually moved into close proximity to one another, and Lys235 was angled towards the P1 pocket of FD. Residues 225-238 and 345-351 on FB as well as residues 76-77, 1350-1358, and 1501-1502 on C3b were filled in via MODELLER. A protein structure file (PSF) was generated using CHARMM22 force parameters, with all disulfide bridges and ionized residues accounted for. Realistic ionization states of residues were determined based on model pKa values as well as apparent pKa values, accounting for residues with shifted ionization states due to protein environment. Apparent pKa calculations were performed via PropKa software which calculates the pKa values of the residues in a PDB protein structure using heuristic methods (16) (17) (12). The protein structure file (PSF) was generated under these conditions. Energy minimization was performed via molecular dynamics simulations software NAMD at 300K for 50,000 minimization steps. Minimization optimizes atom positions allowing residues in the reconstructed loop to normalize to an energetically favorable position with respect to their environment. This step provides integrity to the newly constructed loop and primes the protein model for appreciable electrostatic calculations. The minimized model shows that the Arg202 formed a salt bridge with Glu230 of FB at 2.64 Å, and hydrogen bonding with Arg234-Asp177 formed a salt bridge of 2.70 Å. The integrity of the catalytic site of FD—Asp89-His41-Ser183—was maintained, with contacts between

His41-Ser183 at 3.48Å, Asp89-His41 at 1.74Å (Figure 1). Arrangement of catalytic triad, in consonance with the position of the scissile bond of FB, lends integrity to the predicted conformation of the active site. C3b was not considered in the AESOP calculation because it is distant from the FB-FD interface. All analysis and visualizations were done using UCSF Chimera and VMD [18] [19].

Electrostatic Analysis using AESOP: Computational framework AESOP (Analysis of Electrostatic Similarities Of Proteins)—written in R programming language—performs theoretical alanine scan mutagenesis, coupled with electrostatic similarity clustering and free energy calculations to delineate the role of each charged amino acid in binding. AESOP localizes each ionizable amino acid (Glu, Lys, Arg, Asp, His) and one by one truncates them into an alanine by reducing all side chain atoms down to the beta carbon, correcting bond length and charge. Alanine is a small and non-polar residue, because of this replacing a charged species with alanine creates a mutant protein with a perturbed electrostatic profile, while preserving structural integrity. This is done for each charged residue in both FD and FB. AESOP writes a PQR file for each alanine scan mutant and stores it for electrostatic calculation. It then utilizes APBS (Adaptive Poisson Boltzmann Solver) to calculate the distribution of electrostatic potential with respect to the surrounding solution [20]. The linear Poisson-Boltzmann equation (PBE), in equation 1, is used to perform electrostatic calculations with appreciable approximation under physiological conditions.

$$-\varepsilon_0 \nabla \cdot \varepsilon_r(r)\nabla\varphi(r) + \varepsilon_0\varepsilon_r(r)\kappa^2(r)\varphi(r) = \sum_{i=1}^{N} Q_i\delta(r - r_i)$$

(eq. 1)

Electrostatic calculations produce the electrostatic potential (φ) (Units: $k_B T/e$), and they depend on the atomic charges, dielectric environment, and solution ionic strength. The ion accessibility parameter (κ^2) accounts for the distribution of mobile ions, thus representing the solution ionic strength. The dielectric environment is modeled by the electrostatic permittivity of vacuum (ε_0), and electrostatic permittivity of the medium relative to vacuum (ε_r), where $\varepsilon_0\varepsilon_r$ expresses distance-dependent electrostatic permittivity of the medium. For this computation, ε_r represents the dielectric coefficient. Summation of fixed charges (Q_i) of
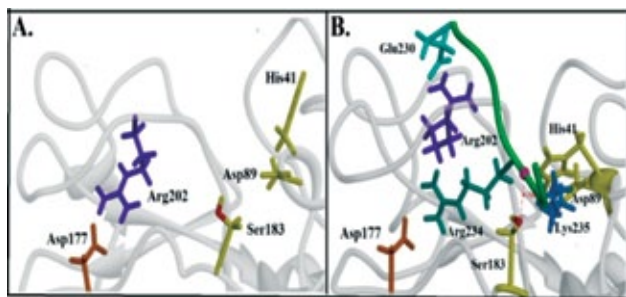
Figure 1: *In FD's free form, Asp177 and Arg202 form a salt bridge, blocking the active site of FD, resulting in a self inhibited state as shown in Panel A. Upon interaction with FB the Arg202-Asp177 salt bridge breaks and Arg202 and Asp177 form salt bridges to Glu230 and Arg234 respectively. Lys235 is inserted into the active site, positioning the scissile bond (Pink) within proximity of the hydroxyl oxygen on Ser183 for nucleophilic attack (4.79Å), as shown in panel B.*

all atom positions is denoted by $\sum_{i=1}^{N} \delta Q_i (r - r_i)$. APBS utilizes electrostatic potential calculations to calculate free energies based on equation 2.

$$G_{elec} = \frac{1}{2} \sum q_i \varphi_i \qquad (eq.\ 2)$$

where q_i = charge. Because free energy is dependent on the surrounding protein environment, free energies of association are calculated for each species alone and for the interacting protein complex. Using the thermodynamic cycle of association and solvation as shown in Figure 2, association free energies in solution can be calculated [9] [10]. Effects of solvation are incorporated into free energy calculations through performing free energy calculations on interacting species in both desolvation state and in ionic solution, to solve for $\Delta\Delta G^{solvation}$. APBS also calculates $\Delta G^{coulomb}$, the free energy of each protein with respect to coulombic potential. This allows for calculation of $\Delta G^{solution}$ with respect to $\Delta\Delta G^{solvation}$, as shown in the equation 3 and 4:

$$\Delta\Delta G^{solvation} = \Delta G_{B-D}^{solvation} - \Delta G_B^{solvation} - \Delta G_D^{solvation} =$$
$$\Delta G^{solution} - \Delta G^{Ref} \qquad (eq.\ 3)$$

$$\Delta G^{solution} = \Delta\Delta G^{solvation} + \Delta G^{coulombic} \qquad (eq.\ 4)$$

Proteins were embedded in a 161×161×129 grid, with dimensions of 155×150×104 Å³. Each grid point i of the model was assigned a charge, dielectric coefficient, and ionic strength. Charges were based on atomic structure. Calculations in solution were done using an ionic strength of 0.150 mM, and a pH of 7.4. Solvent and ion accessibility were determined using probes with radii of 1.4 and 2.0 Å for water molecules and ions respectively. In solution, protein was assigned a dielectric coefficient of 20 and 78.50 for the
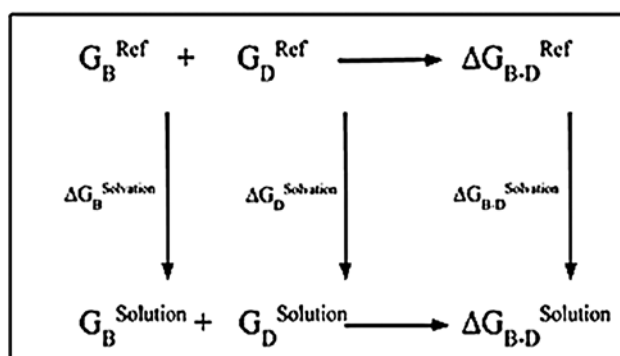
Figure 2: *Thermodynamic cycle of used to calculate free energy of association and solvation.*
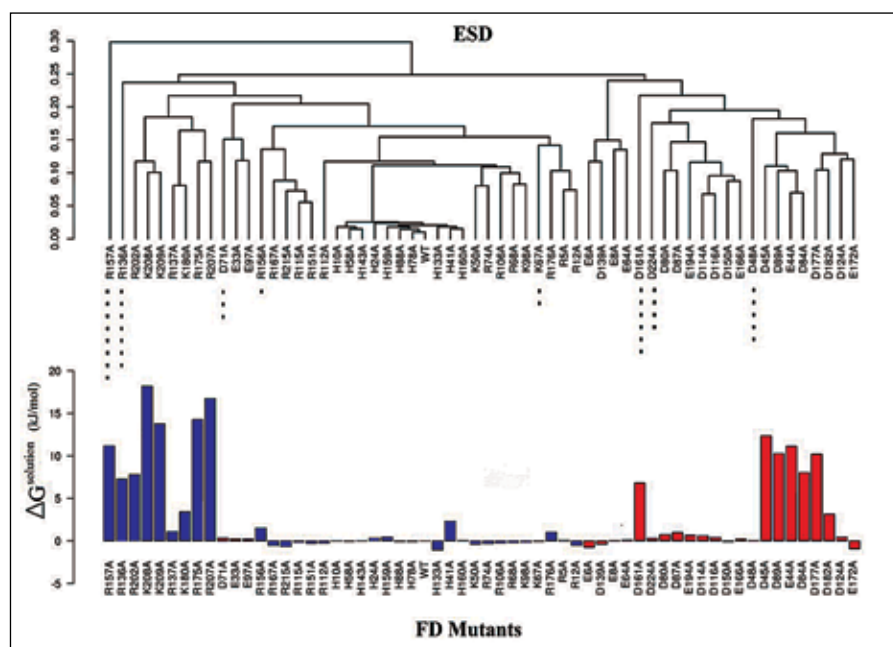
Figure 3. *Dendrogram shows the electrostatic similarity distance (ESD) based on equation 5. Bar graph on the bottom shows the free energy of association of each alanine mutant in solution, relative to the parent protein ($\Delta G^{solution} = \Delta G_{mutant}^{solution} - \Delta G_{WT}^{solution}$). Residues are labeled based on: single letter residue notation followed by the residue number and "A" indicating an alanine mutation. Negatively and positively charged residues are colored red and blue, respectively. Asterisks (*) indicate increasing deviation from parent.*

protein and solvent, respectively. This accounts for the dielectric screening, solvent-protein interactions that naturally occur in physiological solutions. The desolvated reference state, ΔG^{Ref}, was assigned a dielectric coefficient of 20 for both protein and solvent and ionic strength of 0 mM. Free energy calculations were then performed on each mutant and then clustered based on their electrostatic similarity distance (ESD). Hierarchical clustering of the calculated electrostatic potentials was performed using the average linkage method to classify the mutants according to similarities of the spatial distributions of their electrostatic potentials. ESD was determined by averaging the calculated potential difference at each grid point, and was calculated using equation 5:

$$ESD = \frac{1}{N} \sum_{N} \frac{\left(\varphi_a(i,j,k) - \varphi_b(i,j,k) \right)}{\max\left(|\left(\varphi_a(i,j,k) \right)|, |\varphi_b(i,j,k)| \right)} \quad \textbf{(eq.5)}$$

In equation 5 $\varphi_a(i,j,k)$ and $\varphi_b(i,j,k)$ represent the electrostatic potential at some position (i,j,k) of two proteins (a and b), and N represents the number of mutants being compared. Hierarchical clustering was used to group mutants based on their electrostatic similarity distance and visualized in the form of a dendrogram. Through this analysis, the electrostatic contribution of each amino acid is assessed [9] [10].
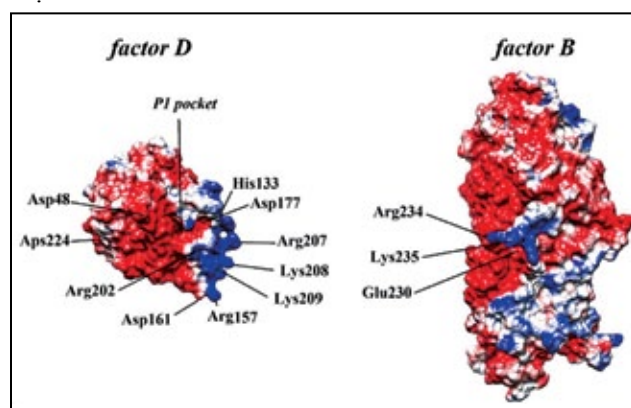
Figure 4: Coulombic potential distribution on the surface of the FB-FD interface. *FB and FD are shown rotated +90 and -90 degrees around a vertical axis to show complimentarily within the FB-FD interface. Surfaces colored blue and red indicate isopotential contours of +1 and -1 (kBT/e), respectively, and white indicates neutrality. Corresponding regions between FD and FB can be visualized, for instance the P1 active site is located in a largely negative pocket, where as the scissile bond loop is positive.*

Results: We utilized AESOP to generate dendrograms and free energy plots for $\Delta\Delta G^{solvation}$, $\Delta G^{Coulombic}$, and $\Delta G^{solution}$, for both FD and FB. For this report only $\Delta G^{solution}$ of FD will be analyzed since it describes association of protein complexes in physiological solution. Electrostatic clustering of alanine scan mutants is shown in the dendrogram of Figure 3. Each line represents a single alanine mutant, and electrostatic similarity is determined by the length of each line, with similarity distance of each mutant quantified by the first horizontal line from the bottom. Hierarchical clustering of mutant families is based on similarities of their electrostatic potential profile with respect to the parent structure. Proteins with ESD=0 are electrostatically identical, and values greater than 0 indicate increasing dissimilarity, with ESD = 0.30 indicating greatest deviation. Eight mutants most deviant from parent are shown in Figure 3, with asterisks (*) indicating greatest deviation from parent. The dendrogram provides useful information regarding the electrostatic contribution of each charged amino acid to its overall functional electrostatic profile (and long-range recognition process), while the free energy of association plot contains information that can assess the extent to which residues are critical to binding (through short-range pairwise interactions). A mutation that results in an increase in free energy (loss of binding) indicates that the residue was critical for protein binding. Similarly, a decrease in free energy indicates that the mutation is favorable, and enhances binding.

Analysis: Data shows that mutation of Arg157 results in the greatest electrostatic perturbation, with a significant increase in , indicating its importance to both binding and catalysis. This result is supported by mutagenesis studies that report complete loss of activity upon mutation [6]. Arg157 is on the edge of a large negatively charged region in close proximity to Asp161, both of these mutations show great electrostatic deviance from the parent, as well as increases values upon mutation (Figure 4). Its location on the edges of FD suggests that this region is important for specific docking of FD to FB. Past studies have shown that alanine mutation at His133 results in loss of activity [6]. This data shows that mutation at His133 results in a more energetically favorable interaction. This suggests that His133, has a role in mediating attractive forces to

maintain particular conformations, or possibly contributes to the release of FD from FB. Residues Lys208, Arg207 and Lys209 show the highest change in respectively, suggesting that these three residues play a critical role in binding. Studies have shown that perturbation of Lys208 via biotinylation causes loss of activity and was speculated to be due to blockage of the binding interface [7]. This observation is consistent with the AESOP results which show that residues Lys208, Arg207 and Lys209 are most essential to binding (Figure 3). These residues are located in a largely positive region on the FB-FD interface, suggesting that this motif is critical for recognition (Figure 4). When compared to homologous proteases—homologies used: human pro-granzyme K (PDB 1MZD), human kallikrein 6 (hK6; PDB 1LO6), human chymotrypsin (PDB 4H4F), and human trypsin (PDB 1TRN)—it can be observed that residues Lys208, Arg207 and Lys209 are not entirely unique to FD. The motif is preserved in chymotrypsin, and Lys209 is conserved in all compared homologies, this implies that although the Lys208, Arg207 and Lys209 motif is critical for binding, it is not unique to FD. Residues Asp177 and Arg202 form a salt bridge in FD's self inhibited state. The Arg202-Asp177 salt bridge blocks the catalytic active site, inhibiting FD in its free form. Upon interaction with FB the Arg202-Asp177 salt bridge breaks to form salt bridges between Arg202 of FD to Glu230 of FB, and Asp177 of FD to Arg234 of FB, a position that allows exposure of the FB's cleavage site (Arg234-Lys235) to orient towards the catalytic Ser183 (Figure 1). Lys235 is under 5 Å from catalytic residues, forming a salt bridge and hydrogen bonding with backbone carbonyl of Ser183 and Arg137 respectively, indicating its role in conformation stabilization. The results show that mutation of Asp177 and Arg202 result in a significant loss of binding and exhibit considerable dissimilarity from parent. Comparison between FD wild type proteins (PDB 1HFD and 1DSU) and an enhanced FD mutant (PDB 1DST) [22], show that Asp177-Arg202 salt bridge appears to be blocking the catalytic site in the FD wild type, while FD mutant with enhanced catalytic activity shows that this salt bridge is broken. It has previously been deduced that the Asp177-Arg202 salt bridge plays an important role in FD's activation [4][5][6], this is supported by detachment of the 202-177 salt bridge in the free form of the enhanced mutant. While Asp177 is conserved in the homologous proteins

mentioned above, Arg202 is unique to FD. In addition to this, it has been shown that mutation at Arg202 increases peptide cleavage three fold. However, it reduced cleavage of FB to 20%, while a mutation of Arg202 and Val203 resulted in essentially no activity [21]. This salt bridge is not present in close homologies and is broken in the enhanced mutant. Together, this can imply that Arg202 is important to the specificity of FD to FB, while contacts with Val203 likely aid to mediate the position of the cleavage site to undergo proteolysis by FD. This suggests that Arg202 and Asp177 are important for self activation by positioning the FB cleavage site in the correct proximity of the active site. Of the eight mutants with greatest ESD, Arg157, Asp161, Asp224, and Asp48, were unique to FD, and the remaining residues were conserved in at most one structure. All of these are located on the surface distant from the active site, suggesting that these residues can be potential candidates for inhibitory drugs.

CONCLUSION

Our work shows that the AESOP computational framework is effective in making predictions accurate enough to be used for effective experimental design. Data provided by AESOP provide mechanistic foresight into the critical components of protein-protein interactions, ultimately allowing for more efficient execution of *in vitro* studies. Understanding the residual components of FD that contribute to its specificity, as well as delineating the difference between FD and other common serine proteases, is critical for designing FD specific inhibitors as therapeutics for autoimmune and inflammatory disease suppression. Our results provide information regarding the importance of all charged residues on FD, in addition to mapping its electrostatic characteristics. The data can be utilized to design drugs that effectively target FD. Future work will be focused on further understanding the dynamics of the FB-FD interaction through the use of molecular dynamics simulations. In addition, AESOP results can be compared with pharmacophore models compatible with FD which can help identify ligand structures ideal for FD specific inhibition.

REFERENCES

1. A. Sahu, D. Morikis, J.D. Lambris (2000) Complement inhibitors targeting C3, C4, and C5, in *Contemporary Immunology: Therapeutic Interventions in the Complement System, pp 75-112*, J. D. Lambris and V. M. Holers, Eds*., Humana Press Inc*.

2. D. Ricklin, J.D. Lambris, (2007). Complement-targeted therapeutics. *Nature Biotech. 25:1265 –1275*.

3. J.E. Volanakis, S.V. Narayana, (1996). Complement factor D, a novel serine protease. *Prot. Sci. 5:553–564.*

4. D. Morikis, J.D. Lambris, Eds. (2005) *Structural Biology of the Complement System*, CRC Press.

5. H. Jing, Y.S. Babu, D.Moore, J.M. Kilpatrick, X.Y. Liu, J.E. Volanakis, S.V. Narayana, (1998). Structures of native and complexed complement factor D: implications of the atypical His57 conformation and self-inhibitory loop in the regulation of specific serine protease activity. *J. Mol. Biol. 282:1061-1081.*

6. F. Forneris, D. Ricklin, J. Wu, A. Tzekou, R.S. Wallace, J.D. Lambris, P. Gros, (2010). Structures of C3b in complex with factors B and D give insight into complement convertase formation. *Science 330:1816-1820.*

7. F.R. Taylor, S.A Bixler, J.I. Budman, D.Wen, M. Karpusas, S.T. Ryan, G.J. Jaworski, A. Safari-Fard, S. Pollard, A.Whitty, (1999). Induced fit activation mechanism of the exceptionally specific serine protease, complement factor D. *Biochemistry 38:2849-2859.*

8. H. Jing, K.J. Macon, D. Moore, L.J. DeLucas, J.E. Volanakis, S.V.Narayana, (1999). Structural basis of profactor D activation: from a highly flexible zymogen to a novel self-inhibited serine protease, complement factor D. The *EMBO Journal 18:804–814.*

9. R.D. Gorham Jr., C.A. Kieslich, D. Morikis, (2011). Electrostatic Clustering and Free Energy Calculations Provide a Foundation for Protein Design and Optimization. *Ann. Biomed. Eng. 39:1252-1263.*

10. C.A. Kieslich, D. Morikis, J. Yang, D. Gunopulos, (2011). Automated computational framework for the analysis of electrostatic similarities of proteins. *Biotech. Progress, 27:316–325.*

11. A. Voet, F. Berenger, K.Y.J. Zhang, (2013). Electrostatic Similarities between Protein and Small Molecule Ligands Facilitate the Design of Protein-Protein Interaction Inhibitors. *PLoS ONE 8(10).*

12. Li, A.D. Robertson, J.H. Jensen, (2005). Very Fast Empirical Prediction and Interpretation of Protein pK$_a$ Values. *Proteins. 61:704-721.*

13. Krieger, S.B. Nabuurs, G. Vriend, (2005). Homology Modeling. *Struct. Bioinform. 44:514.*

14. Sali, T.L. Blundell (1993). Comparative protein modelling by satisfaction of spatial restraints. *J. Mol. Biol. 234:779-815.*

15. Fiser, R.K. Do, A. Sali. (2000). Modeling of loops in protein structures. *Prot. Sci. 9:1753-1773.*

16. D.C. Bas, D.M. Rogers, J.H. Jensen (2008). Very Fast Prediction and Rationalization of pK$_a$ Values for Protein-Ligand Complexes. *Proteins. 73:765-783.*

17. M.H.M. Olsson, C.R. Søndergard, M. Rostkowski, J.H. Jensen (2011). PROPKA3: Consistent Treatment of Internal and Surface Residues in Empirical pK$_a$ predictions. *J. Chem. Theory Comp. 7:525-537.*

18. W. Humphrey, A. Dalke, K.Schulten, (1996). VMD - Visual Molecular Dynamics. *J. Molec. Graph. 14:33-38.*

19. E.F. Pettersen, T.D. Goddard, C.C. Huang, G.S. Couch, D.M. Greenblatt, E.C. Meng, T.E. Ferrin, (2004). UCSF Chimera--a visualization system for exploratory research and analysis. *J Comput Chem. 25:1605-12.*

20. APBS: N.A. Baker, D.Sept, S.Joseph, M.J. Holst, J.A. McCammon, (2001). Electrostatics of nanosystems: application to microtubules and the ribosome. *Proc. Natl. Acad. Sci. USA 98:10037-10041.*

21. S.Kim, S.V. Narayana, J.E. Volanakis, (1994). Mutational analysis of the substrate binding site of human complement factor D. *Biochemistry 33:14393-14399.*

22. Kim, S.V. Narayana, J.E. Volanakis, (1995). Crystal structure of a complement factor D mutant expressing enhanced catalytic activity. *J.Biol.Chem. 270: 24399-24405.*

23. V.M. Holers, (2008). The spectrum of complement alternative pathway-mediated diseases. *Immunol Rev.223:300-316.*

24. T.J. Dolinsky, P. Czodrowski , H.Li, J.E. Nielsen, J.H. Jensen, G. Klebe, N.A. Baker, (2007). PDB2PQR: Expanding and upgrading automated preparation of biomolecular structures for molecular simulations. *Nucleic Acids Res 35:522-525.*

25. T.J. Dolinsky, J.E. Nielsen, J.A. McCammon, N.A. Baker, (2004). PDB2PQR: an automated pipeline for the setup, execution, and analysis of Poisson-Boltzmann electrostatics calculations. *Nucleic Acids Res 32:665-667.*

26. C.M. Stanton, J.R.Yates, A.I. den Hollander, J.M. Seddon, A. Swaroop, D. Stambolian , S. Fauser , C. Hoyng , Y. Yu, K. Atsuhiro , K. Branham , M. Othman , W. Chen, E. Kortvely , K. Chalmers, C. Hayward, A.T. Moore, B. Dhillon, M. Ueffing , A.F. Wright . (2011) Complement factor D in age-related macular degeneration, *Invest Ophthalmol Vis Sci., 52: 8828-34.*

27. G.B. Appel, H.T. Cook, G. Hageman, J.C Jennette, M.Kashgarian, M. Kirschfink, J.D. Lambris, Et. Al., (2005), Membranoproliferative Glomerulonephritis Type II (Dense Deposit Disease): An Update, *JASN, 16:1392-1403.*

Clothes Make the Woman; Women Make the Clothes: A Glimpse Into the Homemade Wardrobes of Two Sisters in Nineteenth-Century Rural New Hampshire

Nicole De Silva and Molly McGarry

Department of History

ABSTRACT

My larger project, "Cottage on the Hill," threads together a collection of nineteenth-century personal artifacts owned by a rural New Hampshire family, the Hayes. Using a material culture approach, the analysis weaves together the textures and patterns that the Hayes family both encountered and created during America's market revolution. The research is motivated by an attempt to fit the Riverside Museum's Hayes Collection within a larger historical context. Within this excerpt, "Clothes Make the Woman; Women Make the Clothes," I examine a series of dresses created by Phebe and Annie Hayes from the late 1850s through the 1880s. Through the eye of each woman's needle, I explore the personal and material ramifications of the shift from a commodity-based household economy to a cash-based system of market capitalism. The movement of work outside the home and the introduction of wage-based labor challenged the provincial, Anglo-American middle-class woman to re-assert the value of her unpaid housework. Even as rural capitalism transformed the home from a place for production to a hub for consumption, I argue that homemade clothing maintained the economic relevance of the woman and of her household labor.

Keywords: commodity culture, American market revolution, women's costume (1850-1880), New England, household economy, rural capitalism

FACULTY MENTORS

Molly McGarry

Department of History

Molly McGarry is an associate professor of history. Her interests include cultural histories of gender and sexuality, public history, and museum studies. She is the author of *Ghosts of Futures Past*, co-author of *Becoming Visible*, and co-editor of the Blackwell *Companion to LGBT/Q Studies*. She has also curated exhibits at the California Museum of Photography, the New York Public Library, the Jewish Museum, and the Chinatown History Project.

AUTHOR

Nicole De Silva

Department of History

Nicole De Silva is a third year honors student with a dual major in American History and Business Administration. Both areas of study strengthen Nicole's ability to interpret cultural artifacts and engage in local public history. Nicole's role as a docent at the Riverside Heritage House gives her an opportunity to study Riverside's late 19th century material culture, and her association with the Riverside Metropolitan Museum (RMM) offers her the chance to explore rich archival collections, including the Hayes Family Respository. The author thanks RMM curators Brenda Focht and Lynn Voorhies along with archivist Kevin Hallaran for their assistance through the research process.

America's market revolution of the nineteenth century changed the way that emerging middle-class families valued labor and understood personal status and identity. The agricultural Hayes family of Farmington, New Hampshire was itself gradually swept up into the capitalist economy. The Hayes Family Collection of dresses, paper ephemera, and reading material housed within the Riverside Metropolitan Museum's archives provides a lens through which changes in personal ideals, labor valuations, and senses of aesthetic style can be observed. The family's two youngest daughters exemplify rural middle-class women at the threshold of a series of transformations from rural to urban, household to industrial, and artisan to professional. I argue that the dresses produced and worn by Phebe (1837-1917) and Annie (1845-1919) Hayes allowed them to navigate, interact within, and even explain a changing provincial middle-class culture from the 1850s-1880s. As the work of their husbands moved outside of the home, provincial women were no longer able to define themselves as productive laborers within a self-contained family farm. The emergence of a nuanced cult of dress, enabled by the expanded commodity culture, allowed women like Phebe and Annie to assert both personal excellence and economic worth from the vantage point of their own domestic sphere.

My analysis employs a material culture approach. This method reads artifacts, including photographs, decorative household items, and clothing, as historical texts. The approach borrows from both history and archaeology. History provides a rich written record; archaeology fleshes out the literature by giving a glimpse into moments that were never recorded in document form. As public, physical representations of social and personal identity, clothing has the power to reveal unspoken details about its wearers. In this analysis, I attempt to situate the physical wardrobe pieces of Phebe and Annie Hayes within the women's surrounding experiences.

The clothing items are best viewed in light of family literature, contemporary fashion manuals, and information about the women's personal lives. Such sources reveal the surrounding ideologies that charged the wardrobes with meaning. If, for example, young Phebe or Annie had leafed through her father's issue of *The Saturday Courier* on October 15, 1847, she may very well have come across the weekly Featured Story. In

this narrative, the character Rosa Newell was drawn as a symbol of pastoral simplicity. Orphaned and desperately poor, Rosa was nevertheless happy in her innocence[2]. Her wealthy cousin Edna, however, was burdened by aristocratic pretension. When the two girls met the dashing and noble Sir Henrick de Lisle at a ball, his "truly noble heart" was able to see clearly through Edna's bourgeois display. Rosa's "sweet timidity and natural modesty shut out all fears of rivalry from… vanity-enthralled Edna[3]."

The moral of the story was explicitly divulged in its concluding sentence: "the artless Rosa Newell won, without an effort, a truly noble heart, while the brilliant heiress, the unblushing coquette, lived to regret her mistaken wiles, and to mourn over the wreck of her brightest hopes upon the shore of vanity."[4] These characters can be seen as metaphors for rural and urban style. They act as part of a parable designed to instruct and elevate the pastoral simplicity of the country. The rural style was, for the parable's anonymous author, simply in better taste than the gaudy commodity culture of urban areas. The story also has a far more direct interpretation. For sentimental authors in the 1840s and 1850s, the ideal woman was equipped with lasting virtue, not fleeting charm. Ideally, this virtue was communicated through both her actions and the symbolism of her simple and practical dresses.[5] This was the provincial ideal of middle-class womanhood to which the Hayes daughters would aspire. Indeed, it was the cultural legacy that they hoped to receive from both their parents and their community.

Annie's own sense of pastoral virtue was cultivated during her stay at Wolfeboro Academy at the age of 12 in 1857.[6] Rural academies such as Wolfeboro aimed to create a physical space for the study of self-control, temperance, and individual determination. Such ethics were essential for both self- and community improvement. By preparing students to lead their own virtuous lives, school historian Rev. John Hayley believed that Wolfeboro Academy might develop its "noble men and saintly women" into missionaries of cultural values for others.[7] Wolfeboro sought to infuse pupils with the tenets of the Congregational church as well as with an understanding of basic academic subjects.

Situated in rural New Hampshire, the academy was located about 20 miles away from Annie's native Farmington. While she would likely find herself among rural pupils from similar backgrounds, they were not the same companions with whom she had grown up in her own small town. In this expanded sphere, Annie was given the chance to somehow test, prove, or reaffirm her personal identity. Her homemade school wardrobe likely created the visual foundation for her reaffirmed sense of pastoral self.

Annie attended Wolfeboro in the simple, homemade, turquoise/tan ensemble pictured here in Figure 1. This dress, documented as being worn to the Academy in 1857, indicates a certain rural plainness and pragmatism.[8] At the same time, fashion trends that were typical of the 1850s were followed. The pagoda sleeves, bright-colored striped fabric, and low-set shoulder reveal a desire to follow the current fashions while simultaneously adapting them to provincial life and village standards. *Godey's Lady's Book* itself noted the popularity of fabric with horizontal stripes of conspicuous colors in 1854.[8] The circular skirt could support the popular cage crinoline of 1856 or the mass of petticoats aimed at creating a fan shape.

Figure 1. Handmade Dress worn by Annie Hayes to Wolfboro Academy, circa 1857

The design of the dress reveals an awareness of current trends. At the same time, it offers a far simpler variation on fashionable themes. Ultimately, the dress reveals a sense of self as defined by part of a rural and school community, and it also indicates a degree of personal autonomy. By constructing her own clothing within her own style, Annie asserted independence from both the fashion press as well as from expensive dressmakers. In this way, her material symbolism echoed the self-sufficient dreams of the household economy as a whole: those of honest toil, proud craftsmanship, and simple practicality.[10]

The tendency to both personalize and localize fashion trends was not a distinctly rural behavior. Dress historian Alison Gernsheim argues that most affluent people modified the main trend of fashion, rather than following fashion plates to the letter.[11] Fashion plates were, says Gernsheim, fantasies or ideals. They were the exception, and hardly the general trend.[12] Fashion publications such as *Godey's Lady's Book* and *Harper's Bazaar* provided guidelines for a wardrobe that could ultimately function as a showcase of individual qualities.[13] Natural modesty as typified by the symbolic character of Rosa Newell, seems to be one of the leading qualities that Annie hoped to project. An identity within a self-sufficient, pastoral community also shines through her colorful, home sewn school dress.

In the early 1860s, through marriage, both Annie and her sister Phebe found the opportunity to develop new, adult identities. Phebe wed John Cate, a storeowner and Union soldier. Annie married local resident Orrin Tenny Fall.[14] While Annie and Orrin remained in Farmington, NH; Phebe relocated to Wakefield, MA near Boston. With these new civil statuses came opportunities for material expression. No longer were the women tied to their father's household. Through the 1870s and 1880s, the updated wardrobes of these two wives adhered to a national standard of fashion far more closely than had their 1850s school dress. Despite an overall compliance with cosmopolitan style, the homemade dresses of Phebe and Annie continued to indicate a certain degree of personalization and customization. Their vision of urban fashion was inflected by local availabilities and tastes.

After the Civil War, railroads enabled the unprecedented movement of people and goods between regions, allowing for a more national commodity culture. New England's rapidly growing industrial landscape likely contributed to the desire to reinvent rural style in the vision of urban fashion. John Cate, Phebe's husband, supplied this demand with his fabric store in Wakefield, MA.[15] Opened in 1870, the store revealed a far more direct participation within the cash-based economy. Such a commercial center also granted women like Phebe local access to the newest styles and patterns of textiles.

As the wife of a suburban businessman, Phebe likely encountered neighbors who were culturally distinct from those in her native Farmington. Subsequently, the new Mrs. Phebe Cate adopted cosmopolitan styles to keep up appearances. As Dress Historian Joan Severa notes, many rural women likely felt very out of place in cityscapes had they not been fixed up.[16] An up-to-date wardrobe became a necessary passport between the rural and urban communities. With this new influx of fashionable options, the tension between two bourgeois styles—town and country—played out in the lives (and the wardrobes) of women in the 1870s and 1880s.[17]

The dark brown, beige, and grey suit pictured here (Figure 2) is very characteristic of the 1870s.[18] The hip-length bodice, nicknamed a "cuirass" for its armor-like form-fitting shape, was worn with the long-waisted corset that had become popular by 1874. The piece is constructed of a woven silk textile known as taffeta. The piece subscribes to contemporary literature almost exactly. In 1877, fashion publication *The Queen* suggests that at least two fabrics be selected and intertwined through any dress' construction.[19] In this piece, the solid color textile is carried into the skirt with dark brown facings, bows, and bands along the bottom. Alison Gernsheim notes the particular popularity of contrasting sleeves as well as a "plastron" or band set in the front of the bodice to give a waistcoat effect.[20]

Figure 2. Dress constructed by the Hayes women in a typical 1870s style.

The thin bustle, long and fitted bodice, and elaborate sleeve trimmings follow the major styles of the 1870s. The piece also leaves room for personalization. The choice of fabric here is somewhat more drab and austere than what would have been available. At the same time, the folksy print of the principal material gives a pastoral feel. City and country are not binary opposites; instead, urban style meets rural taste in the wardrobes of these women.

The 1870s were one of the most complex eras of fashion design, defined by an intricate mixing of colors, long, tight bodices, and ornate bustles. By 1879, the interest in mixing textiles evolved into a more subtle tendency: fashion manuals prescribed the use of a dull-surfaced and a glossy material of the same color, or shades

Figure 3. Gown from the 1880s illustrating the shift to dull-surfaced and glossy-materials.

of the same color.[21] A brown cotton-and-silk bustle gown (Figure 3) from the 1880s illustrates this shift. While still very ornate in construction, the piece does not feature the heavily contrasting fabrics of the 1870s. This three-piece ensemble was constructed of silk taffeta and lined in cotton.[22] A silk velvet pile-weave ornamented the bodice with rosettes, self-bows, and a v-trim along the buttoned front. The taffeta and silk velvet matched in color but differed in shade and luster, creating a visually interesting contrast. A popular dress magazine, *Peterson's,* prescribed in 1882 that "a street or visiting costume [should] match in color, though [each part] may be of different materials."[23] Taffeta and velvet were particularly popular.[24]

The skirts were intricately pleated by hand. The rosettes, bows, and trims were affixed with careful handwork. At the same time, this dress offered a prime example of the use of the home sewing machine. This increasingly affordable device allowed women to create complex masterpieces for themselves. Joan Severa calls the sewing machine a "matter of some social importance" among the middle class, both

urban and rural.[25] These machines did not simplify the work of the woman; rather, they increased expectations, allowing the middle class to have extensive and elaborate wardrobes.[26] Coupled with the revolution of fashion information—such as new, easy to follow Butterick patterns—the well-dressed woman faced higher expectations and a heavier workload than ever before.[27]

In the 1880s, provincial New England became even further entrenched in market capitalism: as a result, its women had more time to indulge in fashion and enjoyed greater access to fabric in stores like that of John and Phebe Cate. In 1886, the deep back-bustle paired with the

Figure 4. Dress from mid-1880s depicting the deep back-bustle paired with the new shorter waist.

new, shorter waist of the 1880's created a dramatic hour-glass figure (Figure 4). Such a combination can be seen in the two-piece blue silk walking gown.[28] The iridescent taffeta fabric combines tan and blue silk fibers for a very sleek and glossy effect, which is offset beautifully by medium-blue silk velvet lining. The eye is drawn directly to the intricate pleating down the skirt front, which was done in three layers, each separated by a band of velvet. The back features the dramatic bustle of the mid-1880s. Such intricate work reveals that in the 1880s, women spent more time and effort constructing their wardrobes than ever before.

Several factors worked in tandem to produce the transformation seen in the wardrobes of Phebe and Annie. Rapid technological improvements, including new patterns and sewing machines, certainly played a role in creating a change in commodity culture. These developments in the methods of clothing construction were accompanied by a slow and uneven shift from household to market economy. Such a transformation resulted in the increased separation of the gendered spheres. Historian Katherine Kelly asserts that as the century progressed rural capitalism undermined old social and economic structures.[29] The household economy had offered flexibility within divisions of labor; however, as the male world of work shifted outside of the home, the domestic sphere

became increasingly feminized.[30] Within rural capitalism, commitment to the urban bourgeois style deepened: women who sought a place within a growing, national middle class needed to assert their position visually with the performance of fashion.[31] Productive labor within a dying household economy no longer served as a sufficient means of self-definition.

In a cash-based economy, a woman's housework became harder to value than the wage labor of her husband. "It is so seldom that women make money," writes one contemporary, "they do not count their time as worth anything."[32] Likely, this devaluation of women's unpaid household labor and the cynical feelings that accompanied it undergirded the development of the city's aesthetic style. Tight corsets, heavy skirts, and restrictive designs cast the wife as a domestic ornament rather than as a direct monetary contributor to the household. She was no longer expected to make a contribution of direct cash value; instead, it was her duty to be as attractive as possible.[33] However, the savvy woman could use this complex symbolism of dress to communicate inner worth, personal aesthetic style, and social class.

The influx of fashion information and affordable materials gave the industrious woman no excuse to neglect popular styles. A failure to adhere to fashion was merely a representation of personal inattentiveness and an idle nature. In fact, this personal carelessness could indicate further character faults: "no excellence of mind or soul can be hoped from an idle woman" who was incapable of keeping up appearances.[34] Furthermore, an attractive dress acted as a bridge between the home and the world outside. It served as a passport to almost anywhere that provided strangers with a quick criterion of a title to consideration.[35] A woman well-versed in the subtle language of fashion could quickly reveal personal leading qualities to any unfamiliar neighbor. This cult of fashion, however, is riddled with paradox. Indeed, it required a careful balancing act. In order to communicate her domestic industriousness and social usefulness, the woman needed to construct a fashionable wardrobe without suggesting an overly frivolous obsession with her appearance.

The pride that the Hayes women exhibited in their sewing indicates that these items were more than mere necessities—they were markers of self, means of artistic expression, and

methods of exploring changing roles and definitions. The homemade clothing of Phebe and Annie formed the bridge between their parlors and the evolving communities outside. As the women ventured into new social spaces and outside villages, their wardrobes served as passports. The dresses drew paths between traditional provincial aesthetics and a growing commodity culture, allowing the women to move between country and city. Both Annie Hayes' plain 1850s school dress and the complex 1870s silk suits of her sister illustrate an independent aesthetic style and an attempt to express a certain ideal of feminine excellence. At the same time, the visual differences between these pieces highlight changing ideals of womanhood, shifting methods of labor valuation, transforming aesthetic values, and growing material availabilities. Even as styles changed through the 1850s, 60s, 70s, and 80s, clothing remained a placard upon which women such as Phebe and Annie Hayes might display both personal senses of self and value as industrious members of the household.

REFERENCES

Cate, Crawford. "Letter to the Riverside Metropolitan Museum," Archived October 29, 1999. Riverside Metropolitan Museum Archives, File A420.

Gernsheim, Alison. *Victorian and Edwardian Fashion: A Photographic Survey*. New York: Dover Publications, 1981.

Halttunen, Karen. *Confidence Men and Painted Women.* New Haven: Yale University Press, 1982.

Hayley, John W. Rev. *Wolfeboro and Tuftonborough Academy, 1821-1887*, Wolfeboro: Myron G.F. Roberts, n.d.

Kelly, Katherine. *In the New England Fashion: Reshaping Women's Lives in the Nineteenth Century.* Ithaca: Cornell University, 1999

Kimmel, Michael. *Manhood in America: A Cultural History*. New York: Free Press, 1996.

Riverside Metropolitan Museum Archives, The Hayes Family Collection, Box #2, Donor A420, "Rolled Up Register of the Hayes Family." Archived October 19, 1999.

----------. The Hayes Family Collection, Donor A381, Items # 46, 55, 62, 191: Dresses of Phebe and Annie Hayes.

Severa, Joan. *Dressed for the Photographer: Ordinary Americans and Fashion, 1840-1900*. Kent: Kent State University Press, 1997.

Unknown. "Featured Story" The Saturday Courier, 15 October 1847.

FOOTNOTES

[1] Riverside Metropolitan Museum Archives, Located at 3580 Mission Inn Avenue, Riverside, CA, 92501.

[2] Anonymous. "Featured Story" in *The Saturday Courier*, 15 October 1847

[3] Anonymous. "Featured Story" in *The Saturday Courier*, 15 October 1847

[4] *Ibid*

[5] Karen Halttunen. *Confidence Men and Painted Women*, (New Haven: Yale University Press, 1982), 90

[6] Katherine A. Fall, Handwritten Note within *Wolfeboro and Tuftonborough Academy*, Riverside Metropolitan Museum Archives, Hayes Family Collection, Box #1.

[7] John W. Hayley, Rev. *Wolfeboro and Tuftonborough Academy, 1821-1887*, (Wolfeboro: Myron G.F. Roberts), 20.

[8] Riverside Metropolitan Museum, "The Hayes Family Collection," Donor A381, Item 191.

[9] Joan Severa. *Dressed for the Photographer: Ordinary Americans and Fashion, 1840-1900* (Kent State University Press, 1997), 95.

[10] Michel Kimmel. *Manhood in America: A Cultural History.* (Free Press: New York, 1996), 16.

[11] Alison Gernsheim, *Victorian and Edwardian Fashion: A Photographic Survey.* (New York: Dover Publications, 1981), 21.

[12] *Ibid*, 22.

[13] Gernsheim, *Victorian and Edwardian Fashion*, 31.

[14] Crawford Cate. "Letter to the Riverside Metropolitan Museum," Archived October 29, 1999. RMM Archives. File A420.

[15] Cate. "Letter to the Riverside Metropolitan Museum," RMM Archives.

[16] Severa, *Dressed for the Photographer*, 296.

[17] Kelly, *In the New England Fashion*, 231.

[18] RMM Archives, The Hayes Family Collection, Donor A381, Item #55.

[19] Gernsheim, *Victorian and Edwardian Fashion*, 61.

[20] *Ibid*, 62.

[21] *Ibid*, 63.

[22] RMM Archives, The Hayes Family Collection, Donor A381, Item #62

[23] Severa, *Dressed for the Photographer*, 378.

[24] *Ibid*, 390.

[25] Severa, *Dressed for the Photographer*, 293.

[26] *Ibid*, 295.

[27] *Ibid*, 296.

[28] RMM Archives, Hayes Family Collection, Donor A381, Item #46

[29] Kelly, *New England Fashion*, 35.

[30] *Ibid*, 39.

[31] Severa, *Dressed for the Photographer*, 228.

[32] Severa, *Dressed for the Photographer*, 374.

[33] Kelly, *In the New England Fashion*, 190.

[34] Severa, *Dressed for the Photographer*, 10.

[35] Gernsheim, *Victorian and Edwardian Fashion*, 40.

How Prejudice Differs by Outgroup Contact in a Diverse College Environment

Michael Gamboa, Joshua Meadors, and Carolyn Murray

Department of Psychology

ABSTRACT

Social Positive outgroup contact (e.g., friendship with someone from another cultural or ethnic background) is generally considered to be a significant factor in reducing prejudice. Intergroup contact theory literature tends to focus on only two ethnic groups at a time, while the present study investigates the relationships between prejudice and intergroup contact among several combinations of four ethnic groups who regularly interact on a college campus. Participants completed the Quick Discrimination Index as an attitude measure regarding prejudice, and self-reported the percentage of their friends belonging to different ethnic groups as a measure of outgroup contact. Results indicate that outgroup contact is significantly related to lower levels of prejudice. However, outgroup contact is differentially related to prejudice for specific combinations of ethnic groups. Contact with Latinos tends to be related to less affective prejudice for all groups. In contrast, ingroup contact and affective prejudice (i.e., disliking) appear to be negatively related among the Asian and Black group participants. These and other observed differences suggest that intergroup contact may work differently depending on the ethnic groups involved.

Keywords: outgroup, prejudice, stereotypes, discrimination, intergroup contact theory

FACULTY MENTOR

Carolyn Murray

Department of Psychology

Professor Carolyn Murray's research centers upon academic underachievement in nonwhite ethnic minorities. She is a recipient of a NIH grant to study the dynamics of the African American family, specifically the socialization practices employed by African American families and to understand the processes which African American children are prepared to participate successfully in the society-at-large.
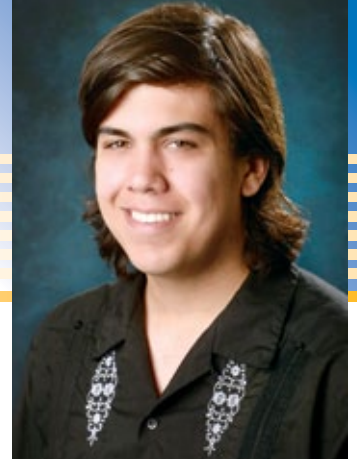
AUTHOR

Michael Gamboa

Department of Psychology

Michael Gamboa is a 4th year student that is majoring in Psychology, Spanish, and Ethnic Studies. He has diverse research interests within social psychology that include prejudice, intergroup contact, and nonverbal bias. Michael is currently completing his honors thesis for the University Honors Program. He plans to continue his studies in graduate school after finishing up at UCR. He would like to acknowledge his faculty and graduate student mentors that have provided valuable feedback and demonstrated great patience along this journey.

Michael Gamboa

INTRODUCTION

People often hold negative attitudes towards those who are different from themselves and consider such people as members of an "outgroup". These attitudes tend to consist of three separate components: (1) stereotypes, the mental images or beliefs that an individual holds of another group; (2) prejudice, the negative affective component or dislike for the outgroup, and (3) discrimination, the behavioral component of how they treat members of an outgroup differently from their ingroup (Allport 1954; Stangor 2009). Intergroup contact theory suggests that positive interaction with outgroup members (i.e., outgroup contact) such as a friendship tends to reduce prejudice. The present study examines the relationship between expressed prejudices and outgroup contact among several ethnic groups to determine if there are comparable patterns of intergroup contact effects among these various ethnicities.

The inherent resistance to change in stereotypes and prejudices presents a difficult obstacle for their reduction. This difficulty notwithstanding, intergroup contact theory provides promising findings (Pettigrew, Christ, Wagner, & Stellmacher 2006; Pettigrew & Tropp 2006; Tropp & Pettigrew, 2005). By positing that individual prejudice can be reduced by increased contact with outgroup members, this research additionally seeks to understand the specificities and contexts which allow outgroup contact to mitigate prejudice. Pettigrew and Tropp's (2006) meta-analysis took a comprehensive look at the effects of outgroup contact on prejudice and concluded that, generally, it tends to reduce prejudice. It is important to note, however, that not all intergroup contact has this effect. The most beneficial outgroup contact involves equal status among the two parties and/or shared values or goals (Allport 1954). Thus, a friendship represents an ideal form of outgroup contact for the elimination of stereotypes and the reduction of prejudice because most friendships are positive relationships with cooperative tendencies (Levin, van Laar, & Sidanius 2003; Turner & Feddes 2011).

Typically, intergroup contact research has focused solely on how contact between majority and minority ethnic groups might lead to reductions in prejudice (Pettigrew & Tropp 2006). The present study, however, investigates the relationship between outgroup contact and prejudice among several ethnic groups on a college campus in an attempt to compare the effects of intergroup contact across groups. According to Allport (1954), prejudicial attitudes develop out of an individual's need or tendency to categorize the world in an effort to simplify and understand it. The categories people create inform not only their prejudices but also the stereotypes they develop (Campbell 1969). These stereotypes are considered the cognitive component of the attitude—mental shortcuts that represent ideas or images of what a person believes a group should look and act like (Stangor 2009). These stereotypes tend to be self-confirming and resistant to change (Stangor 2009), and maintaining a stereotype represents the path of least cognitive resistance (Allport 1954). Campbell (1969) proposed that people who experience only minimal personal contact with an outgroup are more likely to form stereotypes of the "other". However, stereotypes are prone to be erroneous and may misjudge their target, which may influence how an individual feels and acts toward other groups of people (Campbell 1969; Stangor 2009). Based on intergroup contact theory (Pettigrew & Tropp 2006), we predict individuals with less outgroup contact will report more prejudice towards outgroups in general, and we examine the ethnic group differences in the patterns of these relationships in a more exploratory manner.

METHODS

Participants

In exchange for course credit, a total of 812 undergraduate students (286 males and 524 females; M_{age} = 19.44 years) were recruited from the University of California Riverside's research subject pool to participate in a larger experiment from which the present study is adopted. Of these participants, 121 identified as Black/African American, 243 participants as Asian American/Pacific Islander, 134 participants as Caucasian/White, 185 participants as Hispanic/Latino, 58 participants as mixed ethnic background, 61 participants as other, and 10 participants declined to state, or identify themselves, under a specific ethnic background.

Materials

The Quick Discrimination Index (QDI; Ponterotto et al. 1995), a self-report measure of attitudes about racial diversity, multiculturalism, and women's equality, was employed as a measure of prejudice. The QDI was selected because it provides an overall measure of prejudice in addition to subscales measuring both cognitive and affective prejudice that are complementary to the behavioral component of outgroup contact. The QDI uses a Likert scale (ranging from 1 to 5 as "strongly disagree" to "strongly agree") to gauge the extent to which participants agree with thirty statements divided into three subscales regarding multiculturalism (i.e., the cognitive aspect of ethnic prejudice), racial intimacy (i.e., the affective component of ethnic prejudice), and women's equality (i.e., composite prejudice against women). A higher score on the QDI indicates that a person professes less prejudice towards minority ethnic groups and women.

A self-report measurement of outgroup contact was also provided to the participants. This measure asked participants to indicate what percentage of their friends at the university belonged to different ethnic groups (i.e., Asian/Pacific Islander, Black/African American, Latino/Hispanic, and White/Caucasian).

Procedure

The present study was adopted from a larger experimental study dealing with responses to criminal stereotypes. Prior to engaging in the experimental procedure not relevant for the purposes of the present study, the participants filled out a packet of questionnaires providing demographic information, measures of prejudice and out-group contact. The questionnaire packet included both the QDI and the measure of outgroup contact, which we used as the primary variables of interest in the subsequent analyses.

RESULTS

To investigate the relationship between outgroup contact and prejudice, Pearson product correlation tests were conducted. The data obtained indicate that outgroup contact with particular ethnic groups is related both

positively and negatively to scores on the QDI and this differs both by magnitude and direction according to the ethnic group the participant belongs to. Table 1 depicts the overall correlations between contact with a specific group and prejudice, and Table 2, shows the outgroup contact and prejudice correlations within a given ethnic group.

Table 1. *Correlations between group contact and responses to the quick discrimination index (QDI). Pearson Product correlations between measures of prejudice and contact with ethnic groups. Positive correlations indicate more contact is related to higher QDI scores (i.e., less prejudice). Negative correlations indicate more contact is related to lower QDI scores (i.e., more prejudice). + p< .10.* p<.05.** p<. 001.*

Contact with...	QDI	Multicultural	Intimacy
Whites (N = 754)	-.065 +	-.192**	-.005
Latinos (N= 743)	.159**	.114*	.137**
Asians (N=759)	-.108*	-.151**	-.090
Blacks (N= 718)	.025	.251**	-.047

Table 2. *Correlations between group contact and responses to the quick discrimination index (by ethnicity) Pearson product correlations between measures of prejudice and contact with ethnic groups (categorized by ethnicity). Positive correlations indicate more contact is related to higher QDI scores (i.e., less prejudice). Negative correlations indicate more contact is related to lower QDI scores (i.e., more prejudice). + p< .10.* p<.05.** p<. 001.*

Contact	QDI	Multicultural	Intimacy
Black Contact with...			
Asians (N=115)	-.051	-.234*	.213*
Whites (N=113)	.120	-.187*	.318**
Latinos (N=111)	.152	-.098	.365**
Blacks (N= 117)	-.139	.290*	-.554**
White Contact with...			
Asians (N= 123)	-.064	.029	-.117
Whites (N= 129)	-.096	-.148+	-.094
Latinos (N= 123)	.247*	.124	.240*
Blacks (N= 121)	.260*	.187*	.333**
Latino Contact with...			
Asians (N= 168)	-.098	-.102	-.072
Whites (N= 170)	-.090	-.035	-.076
Latinos (N= 177)	.143+	.062	.113
Blacks (N= 158)	-.058	.018	-.047
Asian Contact with...			
Asians (N=232)	-.379**	-.167	-.440**
Whites (N=220)	.063	-.121+	.314**
Latinos (N=214)	.259**	.255**	.155*
Blacks (N= 205)	.274**	.176	.206*

Michael Gamboa

Overall QDI scores were moderately and positively related to contact with Latinos and weakly and negatively related to contact with Asians. The relationship between contact with Whites and respondents' overall QDI score was weak, negative, and marginally significant. Multiculturalism was positively and moderately related to contact with Blacks, positively and weakly related to contact with Latinos, and negatively and moderately related to contact with Whites and Asians. Racial intimacy was weakly and positively related to contact with Latinos.

Contact with Latinos is positively and moderately related to overall QDI scores and racial intimacy for Whites and Asians. Multiculturalism was positively and moderately related to contact with Latinos for Asians. For Blacks, a strong and positive relationship was observed for racial intimacy and contact with Latinos. Contact with Blacks is positively and moderately related to overall QDI scores for Whites and Asians. Multiculturalism was positively and moderately related to contact with Blacks for White respondents. A strong and positive effect was observed for racial intimacy and contact with Blacks for Whites. Also, Black ingroup contact was moderately and positively related to multiculturalism and strongly negatively related to racial intimacy. Contact with Asians was negatively and moderately related to multiculturalism for Black respondents. A moderate and positive relationship was observed for racial intimacy and contact with Asians for Blacks. Asian ingroup contact was strongly negatively related to overall QDI scores and racial intimacy. Contact with Whites was negatively and moderately related to multiculturalism for Blacks. A strong and positive relationship was observed for racial intimacy and contact with Whites for Blacks and Asians. The implications for these varied relationships are discussed in the next section.

DISCUSSION

The results of the present study generally support the hypotheses regarding outgroup contact and reduced prejudice with some noteworthy variations. Though intergroup contact theory suggests that outgroup contact should reduce prejudice in general (e.g., Pettigrew & Tropp, 2006), the data from this study indicate that the

mechanism may be more complex. Contact with particular groups tends to be associated with higher QDI scores (i.e., less prejudice) though contact with other groups show the opposite effect and these effects tend to vary based on the individual's ethnic background. Although intergroup contact theory suggests that positive outgroup contact causally reduces prejudice, the data collected in the present study are strictly correlational. That is, people may seek out certain friendships with certain groups of people based on their level of prejudice, or friendships with different groups of people may influence their prejudice differently.

People with Asian friends

It appears that people who have more Asian contact tend to express more prejudice (score lower on all scales of QDI: overall, multiculturalism, and racial intimacy), at least among the present study's sample of participants. This finding does not support intergroup contact theory, but if Asians or their friends subscribe to the "model minority" stereotype (Chao et al. 2013), they may tend to view other ethnicities in a more negative light, reducing the effectiveness of positive outgroup contact. The negative correlations observed for Asian ingroup contact may be illustrative of the possible negative effects of ingroup contact on a person's prejudice (Allport 1954); members of the in-group typically reinforce and insulate the values and attitudes of other ingroup members from change regarding prejudicial attitudes.

People with White Friends

That people who report having more White contact tend to be more cognitively prejudiced (hold more stereotypical views) may be due to the fact that the group with more status in society may be more likely to have simplified views of other groups. It may be easier for White people to view others in terms of stereotypes because they themselves are not caricatured or portrayed stereotypically as often. People who are friends with Whites may learn such stereotypical ways of thinking from their friends, or cognitively prejudiced people might naturally have more friendships with Whites. Blacks or Asians with more White contact tended to report less affective (i.e., disliking) and more cognitive prejudice. In general, friendships with outgroup members for Blacks or Asians are related to

more favorable feelings toward other ethnic groups yet more White contact may lead them to internalize negative thought patterns and stereotypes concerning these other groups (or even their own). It also may be that these Blacks and Asians have already internalized such views and seek out more White friends as a result.

People with Latino Friends

The correlations for contact with Latinos and prejudice could strongly support the hypothesis for the effect of outgroup contact and strengthen the claim of intergroup contact theory; overall contact with Latinos was related to positive scores on all the relevant measures of the QDI (i.e. less affective, cognitive, and overall prejudice). Cultural constructs of familism, *simpatía*/friendliness, *respeto*/respect (Holloway, Waldrip, & Ickes 2009), and collectivism (Gaines et al. 1997) that appears to be common among Latinos and their friends may be the reason why participants who reported contact with them tended to have less affective prejudice. Likewise, racial discrimination directed against Latinos may encourage solidarity with other oppressed racial/ethnic groups since they have a direct understanding of the negative effects of prejudice (Craig & Richeson 2011). People with more Latino friends may tend to be less prejudiced via internalization of this attitude or people who understand such experiences in general may tend to have more Latino friends. Since Latinos are less racially homogenous than other ethnic groups they perhaps do not benefit from out-group contact as would be expected.

People with Black Friends

More interaction with Black people most likely leads people to perceive more variability within the ethnic group (Allport 1954) and, hence, subscribe less to stereotypes (i.e., higher multiculturalism). However, people with less cognitive prejudice may have more Black friends since stereotypical views do not prevent them from interacting. A similar effect was also observed for Black ingroup contact though it also seems to lead to more negative feelings (i.e., lower racial intimacy) about other ethnic groups perhaps as a defensive mechanism that results from their historic or present mistreatment by other groups in society. They perhaps know and understand that variation exists

among members of other ethnic groups but have acquired negative feelings toward non-Black people because of past and present injustices. For Whites and Asians, Black people may encourage anti-prejudicial attitudes in their social contexts based on their personal experience with discrimination (Craig & Richeson 2011); or Asian and White people who have an understanding of the negative experience of discrimination may tend to have more Black friends. Likewise, Black people and their friends may adhere to the values of collectivism and familism (e.g., Gaines, 1997), which may lead them to promote anti-prejudicial attitudes.

Limitations

Clearly, the cultural values and norms offered as a possible explanation to the observations do not apply to the same extent to all people that choose to identify with a certain ethnicity; such an approach replicates stereotypical and prejudicial thinking. Even positive stereotypes such as the idea of a "model minority" can be damaging to the people in question (Kim & Lee 2013). A generalization about a group of people can lead to the denial of different experiences of individuals within those groups. In other words, both the denial of and the assertion of cultural differences between ethnic groups can be the bases of negative stereotyping and it is this social reality that increases the social complexities involved and the possibility of confounding statistical analysis.

On another note, it is possible that some of the phenomena observed are influenced by peculiarities of this specific student population or campus culture. On the college campus where the present study was conducted, ethnic groups usually considered "minorities" are in the majority, and Whites are a minority on campus. Such a diverse campus climate may have facilitated the effects of outgroup contact and/or strengthened ingroup contact effects.

Although the QDI has been used in relatively few studies and has not been tested for ethnically diverse populations such as the participants in this study, it was chosen because it measures overall prejudice as well both cognitive and affective prejudice. While social desirability bias is not likely to have affected the QDI scores (Ponterotto et al., 1995), the measure of outgroup contact used in this study

can be subject to desirability biases since students may want to appear as though they are accepting of diverse groups of people by reporting that their friends belong to various ethnic groups. There is no way to verify that they reported truthfully the proportion of their friends belonging to different groups or test the reliability of the measure. Further research should attempt to design a more valid and reliable measure of outgroup contact. Lastly, and probably the larger limitation, is the use of correlational data since (the direction of) causality cannot be inferred. Contact with different ethnic groups clearly relates to prejudice but it is not certain if contact, prejudice, or some other factor is the driving force.

CONCLUSION

Despite some general limitations, the present study provides evidence to support the notion that one's outgroup contact is related to their prejudice. That is, more outgroup contact tends to be related to less prejudice. It seems, however, that contact with different ethnic groups can have varied effects yet it is not clear why these differences were observed. Further research should investigate how contact with certain ethnic outgroups may influence a person's prejudice differently. In our current multiethnic society, it is important to find how different kinds of intergroup contact and related social or cultural mechanisms influence prejudice.

REFERENCES

Allport, Gordon. (1954). *The Nature of Prejudice.* Palo Alto: Addison-Wesley Publishing Co.

Campbell, Donald T. (1969). Stereotypes and the perception of group differences. *American Psychologist,* 22(10), 817-829.

Craig, Maureen A. and Richeson, Jennifer A. (2011). Coalition or derogation? How perceived discrimination influences intraminority intergroup relations. *Journal of Personality and Social Psychology,* 1-19.

Gaines, S.O., Marelich, W.D., Bledsoe, K.L., Steers, N.W., Henderson, M.C., Granrose, C.S., Page, M.S. (1997). Links between race/ethnicity and cultural values as mediated by racial/ethnic identity and moderated by gender. *Journal of Personality and Social Psychology,* 72(6), 1460-1476.

Holloway, Renee A., Waldrip, Amy M., & Ickes, William. (2009). Evidence that a *simpatico* self-schema accounts for differences in the self-concepts and social behavior of Latinos versus Whites (and Blacks). *Journal of Personality and Social Psychology,* 96(5), 1012-1028.

Kim, Paul Youngbin and Lee, Donghun. (2013). Internalized model minority myth, Asian values, and help-seeking attitudes among Asian American students. *Cultural Diversity and Ethnic Minority Psychology,* 1-9.

Levin, Shana, van Laar, Colette, & Sidanius, Jim. (2003). The effects of ingroup and outgroup friendships on ethnic attitudes in college: A longitudinal study. *Group Processes & Intergroup Relations*, 6(1), 76-92.

Pettigrew, Thomas F., Christ, Oliver, Wagner, Ulrich, & Stellmacher, Jost. (2006). Direct and indirect intergroup contact effects on prejudice: A normative interpretation. *Intercultural Journal of Intercultural Relations*, 31(4), 411-425.

Pettigrew, Thomas F. & Tropp, Linda R. (2006). A meta-analytic test of intergroup contact theory. *Journal of Personality and Social Psychology*, 90(5), 751-783.

Ponterotto, J.G., Burkard, A., Rieger, B.P., Grieger, I., D'Onofrio, A., Dubuisson, A., Sax, G. (1995). Development and initial validation of the quick discrimination index (QDI). *Educational and Psychological Measurement,* 55(6), 1016-1031.

Stangor, Charles. (2009). The study of stereotyping, prejudice, and discrimination within social psychology: A quick history of theory and research. In Nelson, Todd D. (Ed.), *Handbook of prejudice, stereotyping, and discrimination* (1-22). New York: Psychology Press.

Turner, Rhiannon N. & Feddes, Allard R. (2011). How intergroup friendship works: A longitudinal study of friendship effects on outgroup attitudes. *European Journal of Social Psychology,* 41(7), 914-923.

Tropp, Linda R. & Pettigrew, Thomas F. (2005). Relationships between intergroup contact and prejudice among minority and majority status groups. *Psychological Science*, 16(12), 951-957.

Welch, Kelly. (2007). Black criminal stereotypes and racial profiling. *Journal of Contemporary Criminal Justice*, 23(3), 276-28.

Network Analysis of Intra-Molecular Interactions of the HIV-1 gp120 V3 Loop

Ilya Lederman and Dimitrios Morikis

Department of Bioengineering

ABSTRACT

The V3 loop is a contact point for the attachment of HIV to target cells, via interactions with co-receptors CCR5 or CXCR4. Despite the fact that the V3 loop is constantly mutating in sequence and is highly flexible in structure, it is capable of recognizing the co-receptors and switching co-receptor as the disease progresses. It has been proposed that the mechanism of recognition involves charge complementarity between the V3 loop and the extracellular domains of CCR5/CXCR4, and that co-receptor switch is mediated by positive charge increase. This study utilizes network theory to analyze networks of intra-molecular interactions within the V3 loop. Contact maps and hydrogen bond analysis throughout the trajectories of molecular dynamics simulations have been used to construct networks of amino acid interactions in two V3 loops with similar sequences but different structures. The underlying hypothesis of our study is that one of the V3 loop structures has selection preference for CCR5 and the other for CXCR4. Community analysis has been used to identify intra-molecular communication within and between the different structural sections of the V3 loops, the base, the stem, and the tip. The network analysis confirms previous studies and provides new insights on the role of critical amino acids for the V3 loop stability and co-receptor selection, and suggests possible allosteric signaling. This work provides mechanistic understanding of viral entry at molecular level, and may be useful for the development of co-receptor-specific anti-HIV drugs for use in personalized treatment of HIV infection.

Keywords: network analysis, HIV-1, gp120, V3 loop, CCR5, CXCR4

AUTHOR

Ilya Lederman

Department of Bioengineering

Ilya Lederman is a Senior in Bioengineering. With an interest in how computation can be implemented for biological research, he joined the Biomolecular Modeling and Design Lab under Professor Dimitrios Morikis in January 2013. He has developed a stronger interest for the process of drug development and how this can be achieved through a computational approach. His research focuses on the protein gp120 of HIV. Specifically, the mechanism by which the V3 loop in gp120 recognizes the CCR5 and CXCR4 receptors of immune cells in the body, despite constant mutation in HIV.

FACULTY MENTOR

Dimitrios Morikis

Department of Bioengineering

Professor Morikis' work focuses on immune system function and regulation, structure-dynamics-activity/function relations, design of peptides and proteins with tailored properties, structure-based drug discovery, and development of structural bioinformatics and *in silico* diagnostic methods. His research is predominantly computational, with emphasis on molecular dynamics simulations, electrostatic calculations, free energy calculations, pharmacophore modeling, virtual screening, and protein-ligand docking, and has an experimental component, with emphasis on binding and biochemical assays and NMR spectroscopy.

INTRODUCTION

The V3 loop is part of the glycoprotein 120 (gp120) located on the outside of HIV-1 and plays an important role in viral entry into host cells by attaching itself to the co-receptors that mark its target cells, which it infects and replicates in[1]. HIV-1 entry into host cells occurs through the adsorption of the surface envelope glycoprotein (comprising subunits gp41 and gp120) on HIV-1 to the host cell membrane through interaction with the primary receptor CD4 and co-receptors CCR5 and CXCR4. After initial contact of gp120 with CD4, a structural rearrangement occurs in gp120 that exposes the V3 loop in order to interact with co-receptor CCR5 or CXCR4, depending on the stage of infection[2]. This causes further conformation changes that facilitates attack of gp41 on the host cell and mediates the fusion of the viral and target cell membrane for the release of viral content into the cell[3]. This mechanism is shown in Figure 1A.

The V3 loop (Figure 1B) is the contact point for initial binding to the receptors and there has been a large amount of background work published that show the high sequence variability and structural flexibility of the loop[2,4]. Despite this variability in sequence and structure as well as the high mutation rate of HIV-1, the V3 loop continues to be capable of recognizing the cell-bound receptors and infecting the cell. The loop also shows a specific preference to either CCR5 or CXCR4 depending on the state of infection or disease, with a preference for co-receptor CCR5 during early infection state and a preference for CXCR4 during late disease states (AIDS)[1,4]. It has been proposed that the physicochemical property important for receptor recognition, selection, and binding is charge complementarity and electrostatic interactions between the positively charged V3 loop and the negatively charged extracellular domain of CCR5 and CXCR4[5]. It has also been proposed that the switch from CCR5 to CXCR4 selectivity as the infection progresses into disease involves certain changes to the protein. These include an increase of the net charge of the loop, the presence of the glycosylation motif, and the presence of positively charged amino acids (residues) at one or more of positions 11, 24, 25, known as the "11/24/25" rule[2]. With the absence of the glycosylation motif N6X7T8|S8X9 (where X ≠ Pro), the loop shows a preference towards CXCR4 while CCR5 is determined by the presence of a positive amino acid at 11/24/25 and the overall net charge[1]. It is also noticed that in the absence of the glycosylation motif, the stem region of the V3 loop is opened and is likely correlated to CXCR4 recognition, whereas a closed structure is likely to promote CCR5 recognition. According to this criteria, one of the structures used in our study is expected to select CCR5 and the other is expected to select CXCR4[2]. There are three conserved mutations in our two V3 loop sequences, N6Q, H13N, F20L of which the N6Q mutation denotes that the glycosylation motif is present (N6) or absent (Q6). We used network analysis to identify the role of amino acids in the various structural communities of the V3 loop to discuss previously determined key amino acids as well elucidate possible new key amino acids that further test the co-receptor selection hypothesis.
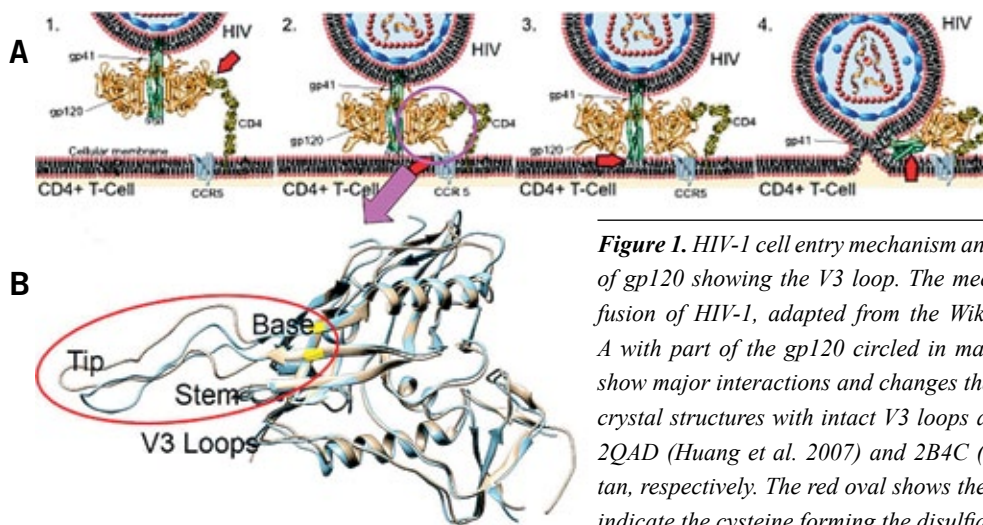
Figure 1. *HIV-1 cell entry mechanism and molecular model of the outer domain of gp120 showing the V3 loop. The mechanism of viral entry and membrane fusion of HIV-1, adapted from the Wikimedia Commons file[21], is shown in A with part of the gp120 circled in magenta and depicted in B. Red arrows show major interactions and changes that occur with cell entry. Two available crystal structures with intact V3 loops are superimposed and have PDB code 2QAD (Huang et al. 2007) and 2B4C (Huang el al. 2005), colored blue and tan, respectively. The red oval shows the V3 loops and the two yellow residues indicate the cysteine forming the disulfide bridge at the base of the loop.*

Network models have become a common way to map out and analyze interactions of physical, biological, and social phenomena and can provide insight on predictive models of these phenomena[6]. Currently, there are many research efforts on HIV prevention and cures, as well as V3 loop characteristics in how HIV attaches to cells. However, we are missing a comprehensive profile of networks of all intra-molecular interactions that occur in the V3 loop to elucidate patterns that would normally not be visible without a mathematical approach. Understanding the role of each residue in the stability and binding of the loop will help in pinpointing the mechanism of co-receptor selectivity. Network analysis involves mathematical analysis and visualization of models consisting of interactions represented by nodes (denoting amino acids in our case) and edges (denoting chemical bonds in our case) that connect pairs of nodes. This approach uses the calculations of degrees, clustering coefficients, optimal paths, and centralities to shed light on the key residues involved in the mechanism of co-receptor selectivity. Community network analysis was used to identify specific groups of residues that are highly intra-connected, but lightly inter-connected to the rest of the protein as well as intra-molecular communication between the three different regions of the loop.

METHODS

Molecular Dynamics (MD) trajectories consisted of 10,000 snapshots saved every 10 picoseconds (ps) for a total 100 nanosecond (ns) simulation. The final 95ns of each MD trajectory were used in our analysis as indicated based on the plateau region of the calculated root mean squared deviation (RMSD) of atomic positions (not shown). Analysis of the trajectories were performed with scripts using the R statistical programming language[9], the Bio3D library[10], and Chimera[11].

In order to generate and view the 3D representations of the interaction networks, NetworkView[12], an extension of the visual molecular dynamics program (VMD)[13], was used. For the network model, each residue of the V3 loop along with atoms within that residue defines one node centered at the Cα atom of the residue. Edges between pairs of nodes are defined by a distance contact map and are drawn

between nodes when atoms corresponding to a node are within 4.5 Å of atoms from another node for at least 50% of the MD trajectory. 4.5 Å was used as it properly represents inter-molecular contacts without creating communities that are single nodes and is not large enough to create edges of interactions that have little to no effect in the molecule. Restrictions were placed to avoid self-edges and edges between covalent bonds to neighboring residues (only non-bonded interactions were looked at). Edges are assigned weights derived from cross-correlation data calculated by the MD analysis program Carma[14] which in turn are used for calculation of edge betweenness, degree, and betweenness centrality. Edge betweenness is defined by the number of optimal paths that cross that edge. A path length is the distance between two nodes and is found by the sum of the edge weights of the consecutive nodes between the two distant nodes with the optimal path being the shortest distance. The weights of the network are treated as distances with shorter paths being strongly correlated or anti-correlated as there is a higher probability of information transfer. Degree centrality is defined by the number of nodes directly connected to the given node and can give an evaluation of the relevance of the node in the network.

The cross-correlation matrix gives the displacement of each C_α atom to every other C_α atom across the MD simulation and defines the probability of correlated motions between two C_α atoms, or the information transfer between two nodes. The matrix elements for two i and j Cα atoms is defined as C_{ij} by the equation $C_{ij} = \dfrac{<\mathbf{r}_i \cdot \mathbf{r}_j> - <\mathbf{r}_i><\mathbf{r}_j>}{[(<\mathbf{r}_i^2> - <\mathbf{r}_i>^2)(<\mathbf{r}_j^2> - <\mathbf{r}_j>^2)]}$, where r denotes the displacement vector, $<>$ denotes the time average over the entire trajectory, the numerator describes covariance, and the denominator describes the variances[2]. Values of C_{ij} range from -1 to 1 with of 1, 0, and -1 corresponding to correlated, uncorrelated, and anti-correlated motions, respectively. The edge weights, w_{ij}, are assigned by the equation $w_{ij} = -\log(|C_{ij}|)$. Weights are used as "strengths" for the edges and change the influence the edges have on nodes in calculations. The equation treats strong correlations and anti-correlations similarly with a value closer to 0 indicating a strong correlation or anti-correlation, and is represented as a thicker line. These

weights were used for the calculation of betweenness since optimal path lengths are found through lower weight values. To account for the calculation of degree centrality, the number of nodes connected to a given node, requiring more influential edges to have larger weight values, the reciprocal of the weight, $1/w_{ij}$, was taken. This was the case because weights used for betweenness centrality is found from optimal path distances with a lower weight (correlation) value corresponding to a higher betweenness.

The VMD extension, NetworkView, utilizes the resulting contact matrix and superimposes it onto the 3D molecular structure. The network is then divided into community subnetworks. Nodes belonging to a community have a stronger connection to each other and a weaker connection to other nodes in the network[15]. Communities are identified using the program *gncommunities* utilizing the Girvan-Newman algorithm which iteratively removes the edge with the highest betweenness until the optimum community structure is found[16].

To calculate network centralities, the network was transferred to a network visualization and analysis program, Cytoscape[17], for a 2D network visualization. Cytoscape uses plugin tools to calculate network features. The plugin CytoNCA was used for the calculation of weighted centralities of degrees and betweenness[18]. Using the correlation data as weights, the weighted degree, C_{Dw}, for each node can be found by the following equation $C_{Dw}(u) = \sum_{v \in N_u} w(u, v),$ where N_u denotes the node set containing all the neighbors of node u. $w(u,v)$ is the weight of the edge connected to node u and node v [18]. Betweenness centrality is a measure of the number of times a node is along the shortest path between two nodes and acts as a bridge connecting different segments of the network. Nodes with high betweenness can indicate importance to maintain node connectivity or overall structure. The shortest path between two nodes is when the sum of the weights connecting the nodes is smallest. From this, the betweenness centrality, $C_B(u)$, is found by the equation $C_B(u) = \sum_{s \neq u \neq t} \frac{\rho(s,u,t)}{\rho(s,t)}$, where $\rho(s,t)$ is the total number of shortest paths from node s to node t. $\rho(s,u,t)$ is the number of those paths that pass through u[18]. The clustering coefficient is a measure of which nodes in the graph tend to cluster together. The clustering coefficient of a node,

C_n, is given by the proportion of edges made between the neighbors of that node over the total number of edges that can exist amongst the neighbors, as given by the following equation $C_n = \frac{2e_n}{k_n(k_n - 1)}$, where k_n is the degree (number of neighbors of n) and e_n is the number of connected pairs between all neighbors of n[18].
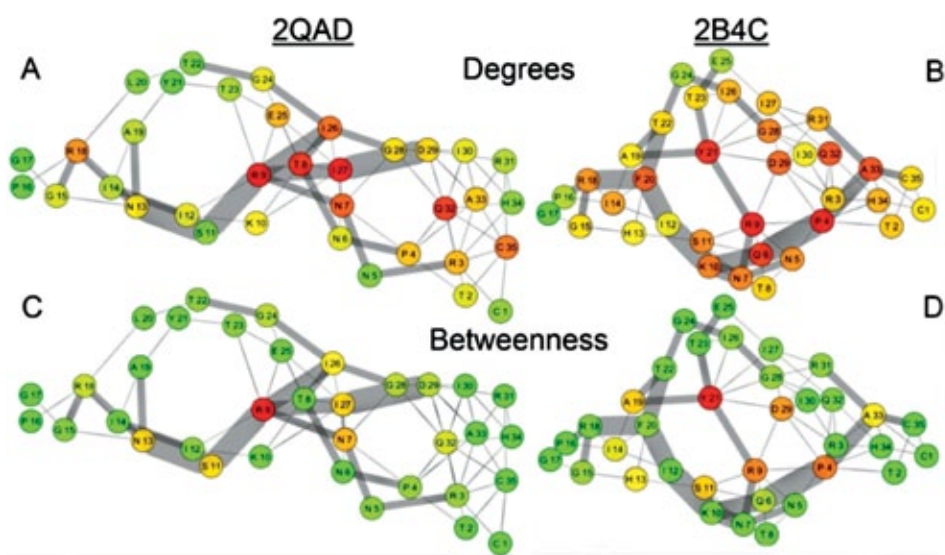
Occupancy networks of hydrogen bonds were also constructed using R, Bio3D, and Chimera. Hydrogen bonds were found using Chimera with a cutoff distance set to 4 Å. Occupancy maps were created and used to generate networks with the occupancy corresponding to the weight and thickness of that particular edge. Weighted degree centrality was calculated and used for the visual representation.

RESULTS AND DISCUSSION

Networks were generated in both a 3D and a 2D representation for each V3 loop structure. The V3 loop possesses three regions: the base which is closer to the core of gp120 and includes the disulfide bridge (residues 1-4, 31-35), the tip at the opposite end of the base (residues 11-20), and the stem between the base and the tip (residues 5-10, 21-30). As shown in Figure 2, the loop also possesses regions that have previously been found to be important: the GPG region, glycosylation motif, and the "11/24/25" rule. The GPG region is a highly flexible and conserved region with residues G15, P16, and G17 in the tip. The mutation from N6 in 2QAD to Q6 in 2B4C causes the absence of the glycosylation motif in 2B4C and the reason for switching between CCR5 to CXCR4 selectivity in 2B4C. As seen in Figure 2 and suggested in [2], 2QAD is a thin structure and 2B4C is and open structure, implicating that the absence of a glycan causes the destabilization of the β-strand of the stem and thus opening of the structure should promote CXCR4 selectivity.

Figure 2 shows the two structures with nodes colored to its respective community. 2QAD (Figure 2A) shows three communities while 2B4C (Figure 2B) shows four communities. Nodes belonging to the same community are more tightly interwoven than the surrounding nodes. Therefore, variation in connectivity between nodes increase local communities within the network. The tip

Figure 2. Network models of the V3 loops for 2QAD (A) and 2B4C (B). Each node (sphere) corresponds to the Cα atom of the residue. Edges represent contacts within 4.5 Å for at least 50% of the trajectory with edge widths corresponding to their weights from the cross-correlation data. Nodes and edges of the same color denote residues belonging to the same community; blue edges denote connection of different communities; cyan denotes the backbone of the loop. Specific side chain residues are shown and are color coded as well: green denotes the GPG motif at the tip of the loop; blue denotes residues involved in the glycosylation motif; red denotes residues involved in the "11/24/25" rule; magenta denotes residues forming the disulfide bridge. Residues belonging to the base (residues 1-4, 31-35), stem (residues 5-10, 21-30), and tip (residues 11-20) are shown.

community is persistent between the two networks with I12 and Y21 in 2QAD joining the stem community for 2B4C and G24 in 2B4C joining the tip community for 2QAD. This persistency in the tip is attributed to the backbone hydrogen bonding of G15 – R18 in both structures. In the open conformation of 2B4C, the tip is stabilized with the F20 strongly interacting with I14, R18, A19, and Y21 and having a π-cation interaction with R18. The absence of the glycan from the N6(2QAD)Q6(2B4C) mutation causes an opening of the structure and in turn a splitting of the stem community. With the splitting, the structure is compressed lengthwise and the stem is involved in more contacts with the base as the structure stays narrow. In turn, residues 3, 28-32 of the base community in 2QAD are switched over to one of the stem communities of 2B4C. 2QAD shows a strong salt bridge between opposite stem strands at R9 – E25 which no longer holds once the structure is opened as seen in Figure 2. Thus this salt bridge no longer stabilizes the structure and allows for the base to move closer to the tip as the stem opens up. With the opening of the stem in 2B4C, the aromatic ring in Y21 moves toward the interior of the protein and forms new contacts with R9, G24, I26, I27, G28, and D29, hence the larger community. Clustering

coefficients of each community have a larger coefficient than the overall average, with the exception of the tip community in 2QAD. This is attributed to the communities, by definition, being a cluster of nodes. The 2QAD tip community is kept narrow through the β-strand of the stem community and thus higher clustering is prevented.

Cytoscape, the 2D network representation program, allowed for the calculation of degree and betweenness centrality and allows for the visual display of the rank directly onto the node. Figure 3 shows two different centrality measurements for both 2QAD and 2B4C. Edge thickness is proportional to the weight according to edge betweenness, ranging from 1 – 333 in 2QAD and 1 – 296 in 2B4C. The thickness of the weights in Figure 3 shows a possible path for long range intra-molecular allosteric communication that may influence interactions with CCR5 or CXCR4. Figure 2 shows that for 2QAD, main path runs through R18, N13, S11, crosses over R9 to I27 and D29. This is also visible in the betweenness centrality calculation with R9 having the largest centrality (Figure 3C). Figure 3A shows nodes with highest degrees belonging to R9, I27, and T8. These residues are the most correlated or anti-

Figure 3. *Cytoscape models showing degree and betweenness centrality. Network centralities visualized in Cytoscape: degree and betweenness centrality calculated using weights from cross-correlation data. The nodes are positioned based on the 3D coordinates from the PDB file. The left and right column represent 2QAD (A, C) and 2B4C (B, D), respectively. The width of the edges are proportional to the betweenness of the edge (number of shortest paths passing through that edge). There are 4 thicknesses with every step up corresponding to 0-25%, 25-50%. 50-75%, and 75-100% of total edge betweenness, respectively. Nodes are labeled by the respective residue and are color coded with a gradient: red denotes highest number; yellow denotes median number; green denotes lowest number.*

correlated to other residues in the loop. Since 2QAD is a thin structure with the collapsed stem community, there are many interactions connecting opposite stem sites, hence the high degree residues belonging to the stem community.

Figure 4 shows the network of hydrogen bonding weighted with occupancy percentage. 2QAD shows the three sites capable of salt bridges having the highest degree centrality: R9, D29, and E25 (Figure 4A). R31, although capable of forming a salt bridge, is only in close vicinity to D29 and thus does not have a large degree centrality. 2B4C displays

a path on one strand of the loop through R18, F20, I12, K10, Q6, P4, and A33. Almost all paths that run from the other strand pass through Y21 to the opposite stem site R9. This is visible in observing the nodes of highest betweenness centrality Y21 and R9 (Figure 3D). Y21 acts as a bridge connecting the opposite site of the stem and shows strong interactions with R9. Degree centrality shows the residue most strongly correlated or anti-correlated to other residues is R9, P4, and Y21 (Figure 3B). Figure 4B shows highest degree centralities in R9, D29, and E32.
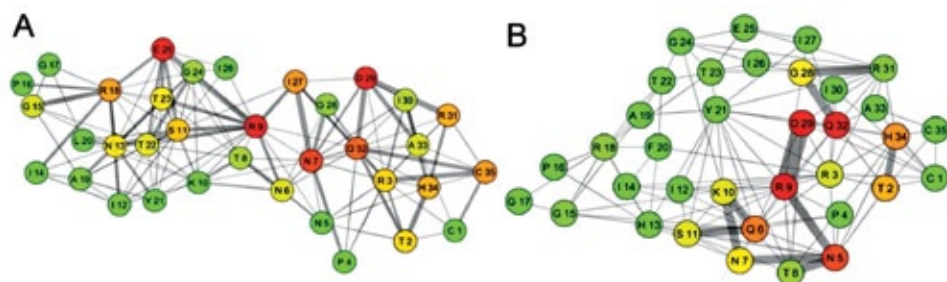
Figure 4. *Hydrogen Bond Occupancy Networks: Cytoscape models of 2QAD (A) and 2B4C (B) based on molecular dynamics occupancies. Network visualizations of occupancy tables derived from 100 ns of a molecular dynamic simulations of 2QAD and 2B4C. Nodes correspond to residues and are colored with a gradient based off the weighted degrees centrality: red denotes the highest number; yellow denotes median number; green denotes the lowest number. Edge thickness corresponds to percent occupancy. Four thicknesses are present with every step up corresponding to 0-25%, 25-50%, 50-75%, and 75-100% occupancy, respectively.*

By any of the measures presented, R9 stays persistent as the critical amino acid in the V3 loop with both CCR5 and CXCR4 selectivity. Arginine is capable of participating in many hydrogen bonds and is central for the stability of the structures as seen in Figure 4. With the opening of the structure, R9 loses its importance in the communication path, but maintains its importance as a critical residue in terms of cross over. Y21 becomes a key residue for the open structure as it holds the opposite stem communities together and creates a bridge for communication across stems through fluctuating strong and weak π-cation interactions with R9. Degree centralities of 2B4C show much greater degree values across all residues, whereas 2QAD shows a more concentrated degree centrality distribution of the stem region. This indicates that with opening of the structure, and preference towards CXCR4, a larger set of residues are required for V3 loop stability than that of CCR5 selectivity where R9 is most critical for stability. Another study by Tamamis and Floudas shows the residues involved in salt bridges when in contact with CXCR4 or CCR5[19,20]. It is shown that with CXCR4 selectivity, R9 has no salt bridges indicating that it is used by the V3 loop to mediate intra-molecular stability of the stem communities. With the CCR5 receptor, R9 is shown to have a salt bridge and indicates that when it is important for intra-molecular communication, it is also important for co-receptor interaction. Sequence logos previously generated show that R9 and Y21 are highly conserved and important for V3 loop co-receptor selectivity (data not shown).

CONCLUSION

This study is based on the hypothesis that the thin structure of the HIV-1 gp120 V3 loop shows preference for CCR5 selection for entry into human cells, whereas the open structure shows preference for CXCR4 selection. The study used network science to determine amino acid residues that are key for intra-molecular structural stability of the V3 loop, and extensions were made for inter-molecular co-receptor selectivity based on the aforementioned hypothesis. The V3 loop interacts with either CCR5 or CXCR4 co-receptors depending on the stage of infection or disease. With the different methods used, R9 has been shown to be crucial in intra-molecular stabilization. We have also provided insight into Y21 being a key amino acid

in the open structure. The switch from a thin structure to an open structure is proposed to promote CXCR4 selectivity and R9 is shown to be highly important in both thin (CCR5 selectivity) and open (CXCR4 selectivity) structures. However, Y21 appears to be a key amino acid with an open structure as it creates a means of communication between opposite, and distant, stem strands in order to contribute to the loop stability. It is also shown that a much larger set of residues are involved in stability with CXCR4 than CCR5 preference. The results have been discussed in view of previous structural and molecular dynamics data. This study offers an intra-molecular understanding of V3 loop interactions for possible drug design studies. Future work will be focused on further testing of the hypothesis, by using patient sequence data to determine if the critical amino acids remain persistent through different sequences.

REFERENCES

1. Wyatt R, Sodroski J (1998) The HIV-1 envelope glycoproteins: fusogens, antigens, and immunogens. Science 280:1884-1888.

2. López de Victoria A, Tamamis P, Kieslich CA, Morikis D (2012) Insights into the Structure, Correlated Motions, and Electrostatic Properties of Two HIV-1 gp120 V3 Loops. PLoS ONE 7(11): e49925.

3. Chan D and Kim P (1998) HIV Entry And Its Inhibition. Cell 93.5: 681-684.

4. López de Victoria A, Kieslich CA, Rizos AK, Krambovitis E, Morikis D (2012) Clustering of HIV-1 subtypes based on gp120 V3 loop electrostatic properties. BMC Biophys. 5: 3.

5. Kieslich CA, Shin D, López de Victoria A, González-Rivera G, Morikis D (2013) A Predictive Model for HIV Type 1 Coreceptor Selectivity. AIDS Res. Hum. Retro 29(10): 1386-1394.

6. Committee on Network Science for Future Army Applications (2006). Network Science. National Research Council. ISBN 0309653886.

7. Huang CC, Lam SN, Acharya P, Tang M, Xiang SH, et al. (2007) Structures of the CCR5 N terminus and of a tyrosine-sulfated antibody with HIV-1 gp120 and CD4. Science 317: 1930–1934.

8.   Huang CC, Tang M, Zhang MY, Majeed S, Montabana E, et al. (2005) Structure of a V3-containing HIV-1 gp120 core. Science 310: 1025–1028.

9.   Foundation for Statistical Computing, Vienna, Austria, 2009; http://www.R-project.org.

10. Grant BJ, Rodrigues AP, ElSawy KM, McCammon JA, Caves LS (2006) Bio3d: an R package for the comparative analysis of protein structures. Bioinformatics 22: 2695–2696.

11. Pettersen EF, Goddard TD, Huang CC, Couch GS, Greenblatt DM, et al. (2004) UCSF chimera - A visualization system for exploratory research and analysis. J. Comput. Chem. 25: 1605–1612.

12. Eargle J, Luthey-Schulten Z (2012) NetworkView: 3D display and analysis of protein·RNA interaction networks. Bioinformatics 28:3000-3001.

13. Humphrey W, Dalke A, Schulten K (1996) VMD: Visual molecular dynamics. J. of Mol. Graph. 14: 33–38.

14. Glykos NM (2006) Software news and updates. CARMA: a molecular dynamics analysis program. J. Comp. Chem., 27(14):1765-1768.

15. Sethi A, Eargle J, Black AA, Luthey-Schulten Z (2009) Dynamical networks in tRNA:protein complexes. PNAS 106(16): 6620-6625.

16. Girvan M, Newman M (2002) Community structure in social and biological networks. Proc. Natl. AcUSA 99:7821–7826.

17. Shannon P, Markiel A, Ozier O, Baliga NS, Wang JT, Ramage D, Amin N, Schwikowski B, Ideker T (2003) Cytoscape: A Software Environment for Integrated Models of Biomolecular Interaction Networks. Genome Res. 13: 2498–2504.

18. Tang Y, Li M, Wang J, CytoNCA: a cytoscape plugin for centrality analysis and evaluation of biological network.

19. Tamamis P, Floudas CA (2013) Molecular Recognition of CXCR4 by a dual tropic HIV-1 gp120 V3 loop. Biophys. J. 105:1502-14.

20. Tamamis P, Floudas CA (2014) Molecular Recognition of CCR5 by an HIV-1 gp120 V3 Loop. PLoS ONE 9: e95767.

21. Adapted from the Wikimedia Commons file "Image: HIV Membrane fusion panel.svg" "http://en.wikipedia.org/wiki/File:HIV_Membrane_fusion_panel.svg".

Enhanced Corrosion Resistance of Magnesium Anodized in a 10 M KOH Electrolyte

Christopher Miller[1], Aaron F Cipriano[1,2], and Huinan Liu[1,2]

[1]Department of Bioengineering
[2]Materials Science and Engineering Program

ABSTRACT

Magnesium is a promising implant material for orthopedic applications due to its biodegradability and desirable mechanical properties. However, in order for Mg to have widespread clinical applications, engineering solutions that address the rapid degradation in physiological environments and promote bone-forming activity are necessary. The objective of this study was to evaluate the corrosion resistance of anodized Magnesium using a previously reported methodology. This methodology utilized an alkaline electrolyte, which offered an alternative to commercial processes that use highly toxic elements. The anodized substrates were annealed to ensure the generation of a corrosion resistant anodic oxide layer. The corrosion resistance of the anodized and annealed substrates was evaluated by performing the Tafel Test, an electrochemical evaluation of corrosion resistance, using Simulated Body Fluid (SBF) as an electrolyte. The results indicated that our anodization and annealing procedures provided significant corrosion resistance along with previously reported nano-scale surface morphology.

Keywords: oxidation of magnesium, potentiostatic anodization, annealing, corrosion resistance

FACULTY MENTOR

Huinan Liu

Department of Bioengineering,
Department of Material Sciences and Engineering

Professor Liu's research is to understand cell-biomaterial and tissue-biomaterial interactions in 2D and 3D and to develop better tissue substitutes and medical implant materials using biodegradable polymers, ceramic nanoparticles, polymer/ceramic nanocomposites and bioresorbable metals.

AUTHOR

Christopher Miller

Department of Bioengineering

Christopher Miller is a senior in Bioengineering. He has participated in undergraduate research in Dr. Huinan Liu's laboratory, the Biomaterials and Nanomedicine Laboratory, since January 2012. He developed an interest in nanotechnology and biomaterials, and has worked closely with Aaron Cipriano, a PhD. candidate, on several projects focused on improving Magnesium's potential as an orthopedic implant material. He plans to pursue graduate study in Bioengineering and a career in industry.

Christopher Miller

INTRODUCTION

Non-degradable metallic materials, such as Titanium (Ti) and Ti-based alloys, are the current preeminent orthopedic implant materials.[1] As described in detail in our prior publication[2], their permanency and high elastic modulus relative to cortical bone imparts these materials with various deficiencies including the need for a subsequent removal surgery, stress shielding and interference with bone growth of pediatric patients.[3] Magnesium (Mg) and Mg-based alloys can provide solutions to these issues due to their inherent ability to degrade in physiological conditions, the human body's capability to metabolize the degradation products of Mg, as well as an elastic modulus and tensile strength closer to cortical bone than that of Ti as shown below in Table 1.[4-6] However, the degradation of Mg in physiological conditions is far too rapid to permit the development of an Mg-based load-bearing biodegradable orthopedic implant.[4]

Table 1: *Mechanical Properties of Cortical Bone, Magnesium and Titanium Alloys.[6]*

Mechanical Property	Cortical Bone	Mg	Ti alloys	PLA
Elastic Modulus (GPa)	3-20	41-45	110-117	2.2-9.5
Tensile Strength (MPa)	100-200	230-250	730-950	16-69

The purpose of this study was to enhance the corrosion properties of Mg by means of a simple and cost-effective anodization and annealing procedure using 10 M Potassium Hydroxide (KOH) as a non-hazardous electrolyte. The KOH-based electrolyte is notably free of toxic and hazardous compounds commonly used in anodization, e.g. flourides and phosphates.[7, 8] Evaluation of the corrosion resistance of the anodized and annealed samples was performed through acquiring potentiodynamic polarization curves and subsequent analysis via the Tafel Test, an *in vitro* electrochemical test. This procedure involved placing the sample and a counter electrode within an electrolyte representative of the natural degradation environment, in this case simulated body fluid (SBF), and performing a voltage sweep surrounding the corrosion potential of the material, or the applied potential at which a metallic substrate begins to corrode within the electrolyte. Performing a voltage sweep surrounding this potential allowed for the observation of current response as anodic and cathodic reactions occurred on the surface of the substrate, which indicated passive oxidation and active dissolution of Mg respectively. Analysis of this data according to the American Society for Testing and Materials (ASTM) Standard G102 allowed for the estimation of the material's corrosion rate under relevant corrosion conditions.[9]

CONCEPTUAL DEVELOPMENT

In this study we investigated the use of potentiostatic anodization of Mg in a KOH electrolyte to generate a barrier-type oxide layer to enhance the corrosion resistance of Mg, in addition to providing the nano-scale surface morphology we have previously reported.[2] Anodization is a versatile electrochemical procedure which has been utilized to generate oxide layers with nano-scale surface features and corrosion resistant properties on several metallic substrates, including Mg.[10-12] The anodization potentials used in this study indicated that the oxide layers generated were formed due to a transpassive process, wherein the current passing through the substrate was large enough to partially dissolve the oxide layer as the surface of the Mg is being oxidized. This concurrent formation and destruction of oxide layers on Mg provided unique nano-scale surface morphologies on Mg depending on the potential applied, as described in a prior publication.[2] We subsequently annealed the Mg substrates after anodization to ensure homogenous presence of Magnesium Oxide (MgO), which can be formed via a dehydration reaction of Magnesium Hydroxide ($Mg(OH)_2$). It has been shown that dense MgO films are stable and improve the corrosion properties of Mg, while $Mg(OH)_2$ is converted rapidly to soluble $MgCl_2$ in physiological conditions.[13] The objective of this study was to investigate the corrosion resistance of anodic oxide films generated using our previously reported anodization and annealing procedures.

MATERIALS AND METHODS

Mg Substrate Preparation and Characterization

Pure Mg as-rolled sheets with a thickness of 1 mm (Alfa Aesar, 99.95%) were cut into 1cm x 0.5 cm rectangles. The samples were mechanically grinded using sequential

increments of 600, 800 and 1200 grit silicon carbide abrasive papers (Ted Pella, Inc.) to remove surface oxides. The samples were subsequently fine polished using sequential increments of 6 µm, 3 µm, 1 µm and 0.25 µm diamond pastes (Physical Test Solutions) applied with a polishing pad (KEMPAD, Allied High Tech Products) to remove surface defects. Each polished pure Mg sample was subsequently ultrasonically cleaned (VWR, Model 97043-036) for 15 minutes in separate baths of pure ethanol and acetone (Sigma-Aldrich) prior to anodization.

Anodization of Mg

Anodization was performed by controlling the applied potential of the anodization circuit with a potentiostat (Model 273A, Princeton Applied Research) and recording the current response with a digital multimeter (GDM-8251A, GWInstek) interfaced with a desktop PC. The Mg working electrode was connected to a copper contact using a custom-made electrode holder that exposed a surface area of 0.65 cm². Platinum (Pt) foil placed cylindrically around the Mg was used as a counter electrode and a silver/silver chloride (Ag/AgCl) electrode was used as a reference. A schematic of the anodization procedure is provided below in Figure 1.

All anodization electrolytes consisted of a 10 M KOH solution prepared using deionized water and analytical-grade reagents. All experiments were carried out at room temperature. Anodization was carried out at constant voltages of 1.5 V and 2.0 V vs. the Ag/AgCl reference electrode. All anodization processes had duration of 2 hours with stirring to ensure homogeneity of the electrolyte. The anodized samples were subsequently ultrasonically cleaned in pure ethanol for 15 minutes and dried in air prior to annealing.

Annealing of Anodized Mg Substrates

The anodized samples were annealed at 450º C for six hours using an inductive furnace (F47915, Thermo Scientific) controlled by a microcontroller (Micromega) to convert $Mg(OH)_2$ surface layers to MgO by a dehydration reaction. The annealing cycle consisted of an initial heating ramp of 100°C/hour to 450°C followed by six hours at the set temperature and cooling to room temperature.

Evaluation of in vitro Corrosion Resistance

The corrosion resistance of the anodized and annealed Mg substrates was evaluated by obtaining potentiodynamic polarization plots and subsequent analysis via the Tafel Test according the ASTM standard G102. The procedure was performed by placing the anodized and annealed substrates back into the anodization electrode holder and placing the electrode holder into an electrolyte of SBF at pH 7.4, prepared using a previously established lab protocol. The potentiostat was utilized to generate a linear voltage sweep from -3 V to 0 V at a scan rate of 100 mV/s to observe the current response indicative of anodic and cathodic reactions occurring on the substrate surface. The corrosion of Mg, and any other metal, by electrochemical
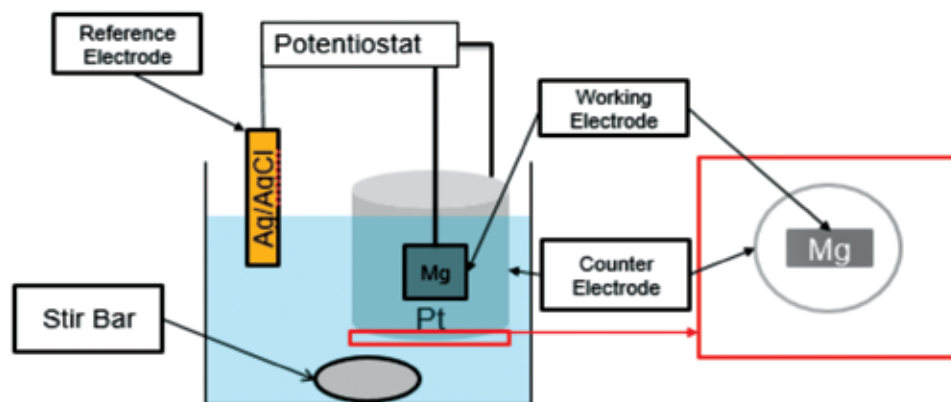
Figure 1: Schematic of the electrode placement for the anodization procedure. *Electrolyte solution consists of 10 M KOH. A) Schematic of the anodization circuit. B) Schematic of Mg and Pt electrode configuration from a bottom-facing view.*

reactions can be defined by partial oxidation (anodic) and reduction (cathodic) reactions. Performing a voltage sweep about the potential acting as the inflection point between these two reactions, or the corrosion potential, allows for quantification of the corrosion properties of that metal within the specified conditions of the simulated electrochemical corrosion through the procedures outlined in ASTM standard G102.[9]

Linear extrapolations of the anodic and cathodic sections of the potentiodynamic polarization plots were performed and the corrosion current (I_{CORR}) was determined. This value was then used to estimate the corrosion rate of the anodized samples using Equation (1), which describes penetration rate according to ASTM Standard G102.[9]

$$\text{Penetration Rate (PR)} = K_1 * (I_{CORR}/\rho) * EW \quad (1)$$

Where:

$K_1 = 3.27 * 10^{-3}$ (mm*g)/(μA*cm*year), I_{CORR} = Corrosion Current Density

ρ = Material Density, EW = Equivalent Weight of Material (Molar Mass/Valence of Element)

RESULTS: EVALUATION OF CORROSION RESISTANCE

Optical photography and characterization by Scanning Electron Microscopy (SEM) and Energy-Dispersive X-Ray Spectroscopy (EDS) of the Mg controls and the anodized and annealed substrates used in this study has

been performed and presented in a previous publication.[2] The obtained potentiodynamic polarization plots of the 1.5 V and 2 V samples post anodization and annealing, as well as of a pure Mg control, are shown below in Figure 2.

As evidenced by the graph in Figure 2 the current response observed in the potentiodynamic polarization plots of both the 1.5 V and 2 V samples is several orders of magnitude smaller than that observed in the Mg control. The I_{CORR} and corrosion rate values quantified through the Tafel Test are shown below in Table 2.

Table 2: Corrosion Current (ICORR) and Corrosion Rate (mm/ year) obtained through the Tafel Test on a pure Mg control and samples anodized at 1.5 V and 2 V for two hours with subsequent annealing treatment.

Substrate	I_{CORR} (mA/cm2)	Corrosion Rate (mm/year)
Mg Control	0.411	9.39
1.5 V	2.11×10^{-4}	4.82×10^{-3}
2 V	3.44×10^{-4}	7.86×10^{-3}

DISCUSSION

The results obtained from the Tafel Test indicated that our anodization and annealing procedures generated barrier-type oxide layers, which provided significant corrosion resistance. The measurements of I_{CORR} and corrosion rate shown in Table 2 indicated that corrosion was slowed by a factor of roughly 1,500 and 1,200 for the 1.5 V and 2
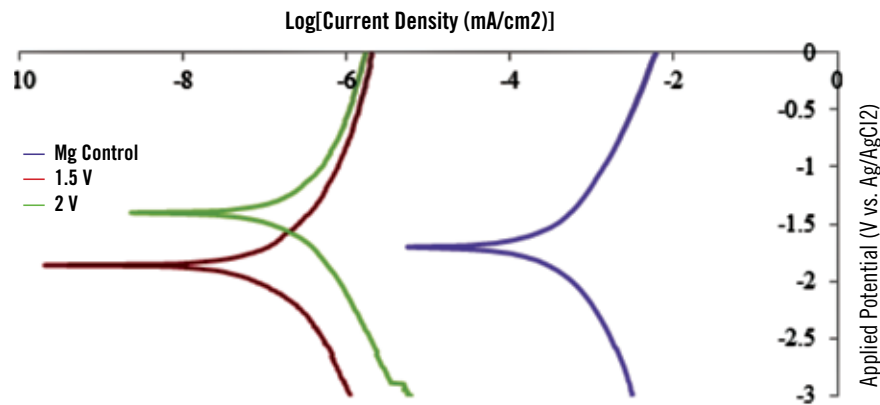
Figure 2: Potentiodynamic polarization curves of Magnesium anodized in 10 M KOH with subsequent annealing treatment. The scan was performed using simulated body fluid (SBF) at pH 7.4 as the electrolyte. Voltage sweep ranged from -3 V to 0 V at a scanning rate of 100 mV/s.

V samples when compared with the pure Mg controls respectively. This result becomes more significant when the ease and low cost of these procedures are considered, as well as their ability to be adapted to a variety of corrosion resistant Mg-based alloys. These procedures could also be combined with strategies such as polymer and composite coatings to further enhance the corrosion resistance of Mg. Enhancing the corrosion resistance of Mg is a necessary step towards taking advantage of its favorable properties in developing biodegradable orthopedic implants, and the results of this study confirmed that our anodization and annealing procedures are promising in achieving this goal. Future work includes the evaluation of the biocompatibility of these anodized and annealed substrates in terms of the osseointegration, anti-bacterial properties, and anti-inflammatory properties.

ACKNOWLEDGEMENTS

REFERENCES

1. Uhthoff, H., Poitras, P., and Backman, D. (2006) Internal plate fixation of fractures: short history and recent developments., *J. Orthop Sci. 11*, 118-126.

2. Miller, C., Cipriano, A., and Liu, H. (2013) Nano-scale surface morphology of Magnesium Anodized in a 10 M KOH Electrolyte, *UC Riverside Undergraduate Research Journal 7*.

3. Shen, C., Jiang, S. D., Jiang, L. S., and Dai, L. Y. (2010) Bioabsorbable versus metallic interference screw fixation in anterior cruciate ligament reconstruction: a meta-analysis of randomized controlled trials, *Arthroscopy 26*, 705-713.

4. Staiger, M., Pietak, A., Huagmai, J., and Dias, G. (2006) Magnesium and its alloys as orthopedic biomaterials: A review, *Biomaterials 27*, 1728–1734.

5. Hort, N., Huang, Y., Fechner, D., Stormer, M., Blawert, C., Witte, F., Vogt, C., Drucker, H., Willumeit, R., Kainer, K. U., and Feyerabend, F. (2010) Magnesium alloys as implant materials--principles of property design for Mg-RE alloys, *Acta Biomater 6*, 1714-1725.

6. Witte, F. (2010) The history of biodegradable magnesium implants: a review, *Acta Biomater 6*, 1680-1692.

7. Koji Murakami, M. H. a. T. K. (2011) Anodization of Magnesium Alloys Using Phosphate Solution, In *Magnesium Alloys - Corrosion and Surface Treatments*, InTech.

8. Bauer, S., Kleber, S., and Schmuki, P. (2006) TiO2 nanotubes: Tailoring the geometry in H3PO4/HF electrolytes, *Electrochemistry Communications 8*, 1321–1325.

9. ASTM. (1999) G102: Standard Practice for Calculation of Corrosion Rates and Related Information from Electrochemical Measurements.

10. Tsuchiya, H., Macak, J. M., Ghicov, A., Taveira, L., and Schmuki, P. (2005) Self-organized porous TiO2 and ZrO2 produced by anodization, *Corrosion Science 47*, 3324–3335.

11. Macdonald, D. D. (1993) On the Formation of Voids in Anodic Oxide Films on Aluminum, *J. Electrochem. Soc. 140*, L27-L30.

12. Lei, T., Ouyang, C., Tang, W., Li, L.-F., and Zhou, L.-S. (2010) Preparation of MgO coatings on magnesium alloys for corrosion protection, *Surface and Coatings Technoogy 204*, 3798–3803.

13. Li, Z., Gu, X., Lou, S., and Zheng, Y. (2008) The development of binary Mg-Ca alloys for use as biodegradable materials within bone, *Biomaterials 29*, 1329-1344.
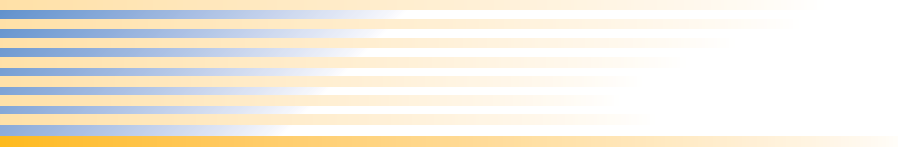
Electrochemical Delamination of MBE-Grown Germanane Film

**Dante J. O'Hara¹, Walid Amamou¹, Patrick M. Odenthal¹, George Floyd¹,
Igor V. Pinchuk², and Roland Kawakami**

¹*Department of Physics & Astronomy, UC Riverside*
²*Department of Physics, Ohio State University*

ABSTRACT

Two-dimensional crystals are an important class of materials for novel physics, chemistry, and engineering. Germanane (GeH), the germanium-based analogue of graphane (CH), is of particular interest due to its direct band gap and spin-orbit coupling. Currently, germanane films are synthesized on conductive Ge(111) wafers making electrical characterization impossible. Transfer to insulating substrates can be achieved through mechanical exfoliation by tape or polymer stamp, however the resulting flakes are small and of low quality. Here, we demonstrate a highly efficient, nondestructive electrochemical route for the transfer of molecular beam epitaxy (MBE) germanane film from Ge(111) surfaces. The electrochemically transferred germanane films are continuous over 95% of the surface and this process affords the advantages of high efficiency and large area transfer.

Keywords: germanane; MBE; electrochemical; bubbling; transfer

FACULTY MENTOR

Roland Kawakami

Professor of Physics, Ohio State University
Research Physicist, UC Riverside

Dr. Kawakami's research explores the physics of nanoscale materials and devices, spintronics, magnetism, and two-dimensional systems. He has undertaken forefront experiments on spin relaxation in graphene; manipulation of pure spin currents in graphene via scattering by magnetic moments; optical pump-probe spectroscopy of spin dynamics in semiconductors; and the first demonstration of electric field control of Verwey transition in magnetite films.

AUTHOR

Dante J. O'Hara

*Department of
Mechanical Engineering*

Dante J. O'Hara is a fourth-year undergraduate student studying Mechanical Engineering. He is a founder of UCR's chapters of Theta Tau Professional Engineering Fraternity and the Professional Fraternity Council, and has been an active member in both the National Society of Black Engineers and the Council for the Advancement of Black Engineers. O'Hara has also participated in the 2012 NSF International Research Experience for Students (IRES) program in China. O'Hara has developed a passion for synthesizing and processing of two-dimensional materials, such as graphene and germanane. O'Hara is continuing his graduate education in the Materials Science and Engineering PhD program at UC Riverside and will continue to work with Professor Kawakami's group.

Dante J. O'Hara

INTRODUCTION

The discovery of monolayer graphene has led to the motivation in nanoscale materials science and engineering to discover and develop materials in two-dimensions (2D) that offer properties not found in graphene, such as a native band gap.[1-4] Of particular interest is germanane, the germanium-based analogue of hydrogen-terminated graphene, or graphane, which has recently been synthesized by molecular beam epitaxy as large area thin films.[5] This was achieved by first synthesizing calcium germanide ($CaGe_2$) films by a molecular beam epitaxy co-deposition technique, then submerging the films in hydrochloric acid (HCl) to de-intercalate the Ca atoms, as shown in Figure 1a.[5,6] This results in stacked layers of 2D germanane sheets, where each sheet consists of monolayer Ge arranged in a hexagonal lattice stabilized by hydrogen as shown in Figure 1b.
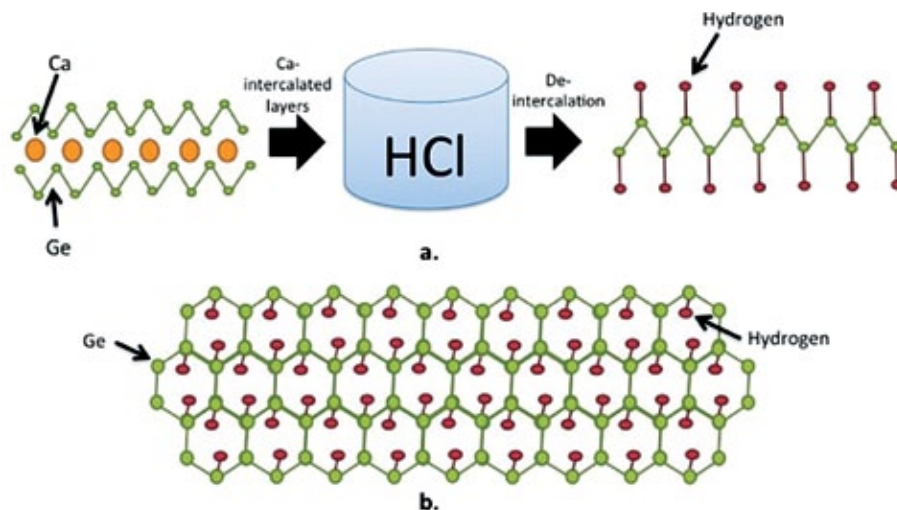
***Figure 1: Synthesis of Germanane. (a)** CaGe₂ de-intercalation in HCl. (**b**) Monolayer Ge stabilized by hydrogen.*

Germanane has several properties that make it extremely attractive. First, it has a direct band gap of approximately 1.5 eV and is theoretically capable of high electron mobility transport (~18,000 cm^2/Vs), which makes it favorable for optoelectronics and nanoscale digital electronics.[5,6] Second, it is thermodynamically stable at room temperature and is resistant to oxidation, which is advantageous for future electronic device applications.[5] Finally, the larger spin-orbit coupling associated with the heavier element Ge (as compared to C in graphene) opens up new opportunities to explore spintronics in 2D.[7-9]

An important challenge, at the conclusion of growth and de-intercalation, is the large area layer transfer of single-crystalline germanane films onto insulating substrates. This is essential for device fabrication to remove parallel conductance through the substrate. The most successful known effort to date has been the mechanical exfoliation of germanane with the usage of polydimethylsiloxane (PDMS). This method produces large flakes with low yield. Another successful method is the mechanical exfoliation by scotch tape, but this method only produces small flakes of germanane.[6] A process for consistent large area transfer is needed to make this material viable for industrial scale.

In this work, we report the successful large area layer transfer of single-crystalline germanane off of Ge(111) substrates by electrochemical delamination. Previously, this method was reported to transfer CVD-graphene grown on Cu.[10-12] We find that this electrochemical delamination is nondestructive to the MBE-grown germanane film and the films are approximately 95% continuous on the transferred substrate.

EXPERIMENTAL METHODS

MBE growth of $CaGe_2$ on Ge(111) for large area germanane

Growth of the germanane precursor, $CaGe_2$, is performed in an ultrahigh vacuum (UHV) chamber with a base pressure of 2×10^{-10} Torr. Elemental Ge and Ca are evaporated from thermal effusion cells with high purity Ge (99.9999%, Alfa Aesar) and Ca (99.99%, Sigma Aldrich) source materials. Growth rates are determined by a quartz microbalance deposition monitor. All films are grown on Ge(111) single-sided mechanically-polished wafers, with an average wafer thickness of 0.35 mm and an orientation tolerance of 0.5 degrees (University Wafer). The starting 2-inch diameter wafer is cleaved into smaller pieces, which then undergo chemical etching to remove the surface oxides/metals and replace them with a thin protective oxide film. Etching involves a sequence of steps beginning with submersion into a 10:1 mixture of $H_2O:NH_4OH$ for

60 seconds followed by 60 seconds in a 10:1 mixture of $H_2O:H_2SO_4$. Finally, substrates are submerged into a 30% H_2O_2 aqueous solution for 60 seconds before being rinsed by de-ionized (DI) water, blow-dried with dry nitrogen and inserted into the UHV chamber. The substrate is annealed at 650 °C for 30 minutes as measured by a thermocouple located near the substrate. *In situ* reflection high-energy electron diffraction (RHEED) is used to monitor the sample surface throughout the growth and annealing process, shown in Figure 2. RHEED utilizes an electron gun that diffracts electrons off of the sample surface and into a camera in order to determine if the material is indeed single-crystal $CaGe_2$. Figure 2a shows RHEED patterns of a Ge(111) surface with a beam along the $[11\bar{2}0]$ in-plane direction at room temperature. Figure 2b shows respective patterns after thermal annealing at 650 °C. Annealing thermally desorbs the protective oxide film from the Ge(111) surface. With the substrate still at 650 °C, a 5 nm Ge buffer layer is deposited with typical rates of approximately 1.5 Å/min as measured by a quartz microbalance deposition monitor. The respective RHEED patterns are shown in Figure 2. An important feature here is the sharpening of the RHEED diffraction streaks, indicating an ordered Ge surface. This procedure is followed for all $CaGe_2$ films grown in this study.

For the co-deposition of $CaGe_2$, we perform adsorption-limited growth with Ge being the limiting species, similar to other semiconducting heterostructure materials.[13-18] First, the substrate is heated to 750 °C then the Ge shutter is opened, with the Ca shutter opening directly after. Approximately 10 seconds after opening the Ca shutter, the RHEED pattern shows a sequence of rapid changes in the surface reconstruction until the stable patterns are shown in Figure 2d after another 20 seconds, which remains throughout the remainder of the growth. The $CaGe_2$ has an atomic layer of intercalated Ca to separate the individual Ge layers.
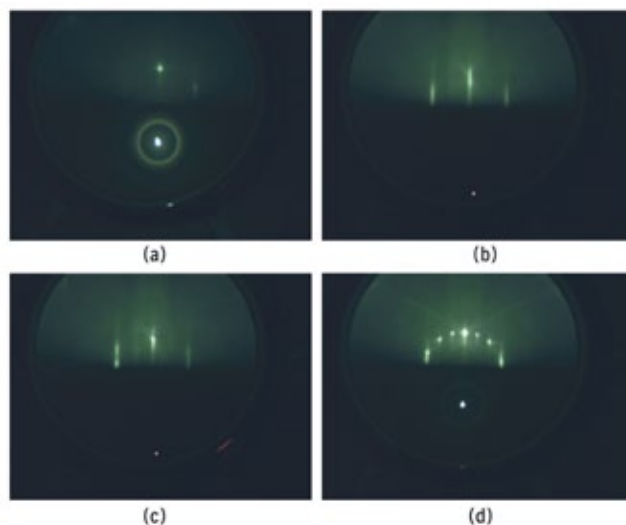
*Figure 2: RHEED patterns of CaGe₂ growth. (a) Ge(111) substrate at RT. (b) Ge(111) substrate post-anneal. (c) 5 nm Ge buffer layer. (d) CaGe₂ growth.*

For the de-intercalation of $CaGe_2$, we submerge the $CaGe_2$ films in 37% HCl aqueous solution at -40 °C for 24 hours to convert the films to germanane. The immersion in HCl de-intercalates the Ca atoms and hydrogenates the Ge atoms, ultimately converting $CaGe_2$ into GeH.[5,6]

Electrochemical transfer from Ge(111) substrates

For germanane grown on Ge(111) substrates, we have developed an electrochemical delamination process, similar to previously reported methods, to transfer the material based on a water electrolysis process.[10-12] Figure 3 shows the procedure performed to transfer the germanane off of Ge(111). After MBE growth and HCl de-intercalation, the germanane was first spin-coated with polymethyl methacrylate (PMMA) at 2,000 rpm for 45 seconds followed by baking the sample on a hotplate at 50
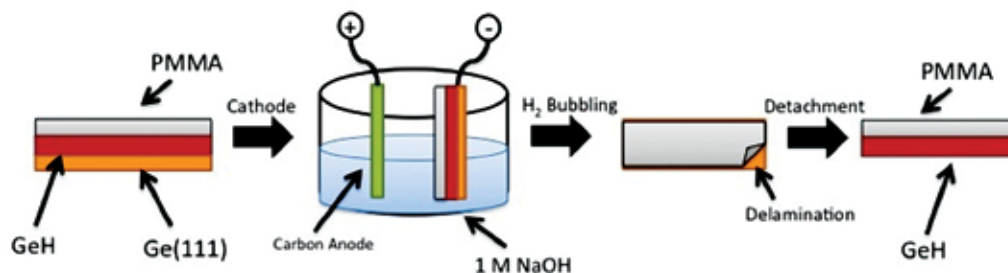

Figure 3: Electrochemical delamination procedure. (a) PMMA spin-coat. (b) Cathode and anode placed in electrolysis solution with constant current supply. (c) Hydrogen bubbling occurs between PMMA and substrate. (d) PMMA/GeH layer separated from substrate.

°C for 120 minutes as shown in Figure 3a. The PMMA-coating of germanane serves as a supporting scaffold so that the germanane film will not roll or tear during the delamination process.[10-12] With its presence, the entire PMMA/germanane layer can be delaminated without any damage to the film, as verified by optical microscopy and scanning electron microscopy (SEM) images shown in Figures 4 and 5, respectively.

Then, the PMMA/germanane/Ge(111) cathode and a graphite anode were dipped into an 1 M NaOH aqueous solution with a constant current supply of 1 A, shown in Figure 3b. The hydrogen bubbling time depends on the size of the germanane film and the constant current applied. For a germanane film of 1×1 cm^2, approximately 10 second bubbling is enough to completely separate the PMMA/germanane layer from the Ge(111) surface under the same conditions in Figure 3b. The corresponding electrolytic voltage was usually 5-10 V. At the negatively charged cathode, a water reduction reaction took place to produce H$_2$ bubbles shown in Figure 3c. The reaction can be represented as follows:

$$2H_2O(l) + 2e^- \rightarrow H_2\ (g) + 2OH^-(aq)$$
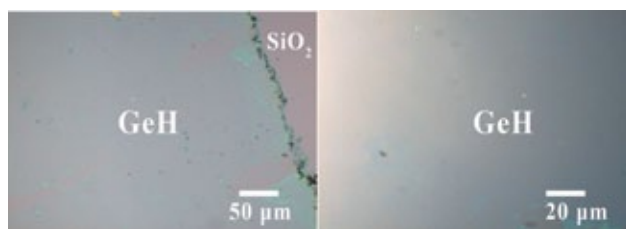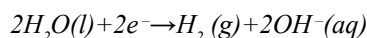
Figure 4: Optical images of 1.5 nm GeH transfer. (a) Transferred sample at 10x objective. (b) Transferred sample at 60x objective.

As a result, the PMMA, with underlying germanane is removed from the Ge(111) substrate as shown in Figure 3d. The PMMA/germanane is then transferred to a bath of DI water, to get rid of the remaining electrolyte on the layer. Next, the PMMA/germanane is transferred to the desired insulating substrate and baked on a hot plate at 50 °C for ten minutes. To remove the PMMA layer, the sample is then immersed in acetone for twenty minutes,
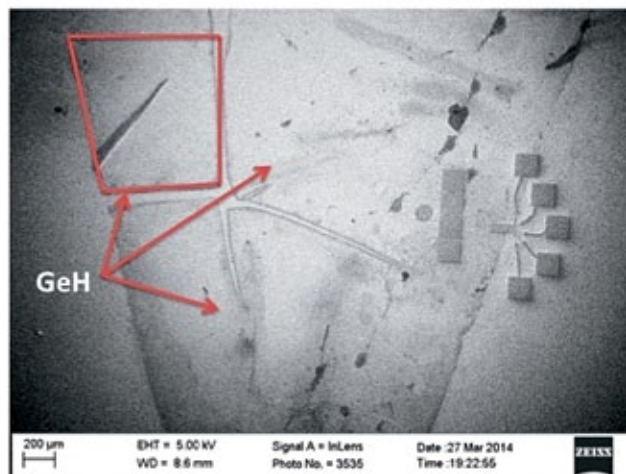

Figure 5: SEM Micrograph of transferred 1.5 nm GeH layer onto Si/SiO2 substrate.

rinsed with isopropyl alcohol (IPA) for one minute, and blow dried with dry nitrogen. The germanane is then ready to be fabricated into a device.

RESULTS AND DISCUSSION

Characterization of transferred single-crystalline germanane films

We characterize the germanane transferred to Si/SiO2 substrates by atomic force microscopy (AFM), shown in Figure 6, to investigate the surface morphology of the transferred film. We show an AFM scan of a 2.5 nm-grown sample in Figure 6b, to observe the step from the transferred substrate to the transferred sample. Figure 6c shows the continuity of the film, yielding relatively the same thickness throughout. Here, we observed significant change in thickness after transfer. We were able to successfully transfer 1.5 nm on to a Si/SiO2 substrate with an rms roughness of 0.26 nm, which is comparable to the germanane on Ge(111) prior to transfer as shown in Figure 6a. We also notice that the terraces from the Ge(111) substrate miscut still remain after transfer, which is similar to the ripples that transfer with graphene grown on Cu foil.[5,10] The germanane film yielded approximately 95% continuous after transfer.
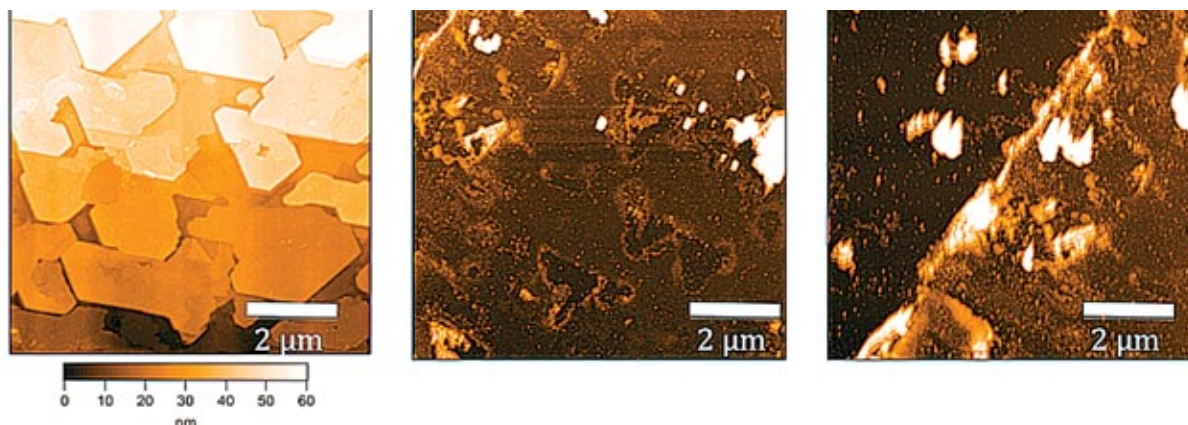
Figure 6: AFM images on the same scale of GeH before and after transfer. *(a) 2.5 nm GeH on Ge(111). (b) 1.5 nm GeH continuous film after transfer. (c) 1.5 nm GeH step to underlying Si/SiO₂ substrate.*

Germanane has a well-known photoluminescence (PL) spectrum.[22] Low-temperature PL measurements further confirm that the transferred film is indeed germanane. Figure 7 compares the PL before and at the conclusion of the electrochemical transfer. The PL wavelength shows a sharp peak at approximately 870 nm after MBE-growth and HCl de-intercalation, shown in Figure 7a. After transfer to another Ge(111) substrate, the PL spectrum has retained its shape and location, shown in Figure 7b. This indicates that the material has not been changed or damaged during the transfer process.
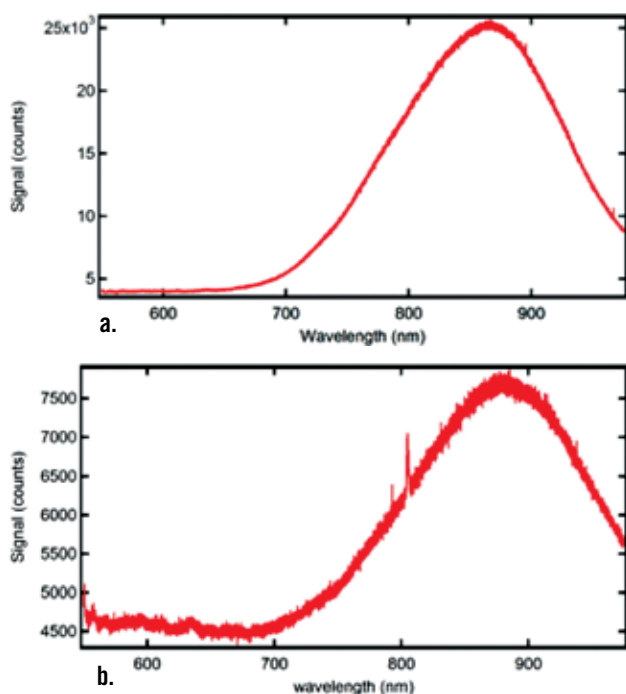
Figure 7: Photoluminescence spectra of germanane films on Ge(111) at 77K. *(a) Pre-transfer. (b) Post-transfer.*

CONCLUSIONS

We have demonstrated the successful large area layer transfer of germanane films by electrochemical delamination. This process maintains the quality and improves the possibility of developing monolayer germanane. With this technique, we have the opportunity to transfer this material to any desired substrate. More importantly, electrical measurements are now possible. This method also gives the ability to produce large area germanane, which is needed for industrial-scale applications. While PL is a useful tool to indicate that our transferred material is indeed high quality germanane further study, such as energy-dispersive X-ray spectroscopy (EDS) or Fourier transform infrared spectroscopy (FTIR), is needed to fully characterize the impurities and defects in the transferred material. These results will provide a significant advance towards large area transfer of high quality, single-crystalline germanane.

REFERENCES

1. K. S. Novoselov, A. K. Geim, S. V. Morozov, D. Jiang, M. I. Katsnelson, I. V. Grigorieva, S.V. Dubonos, and A. A. Firsov: Two-dimensional gas of massless Dirac fermions in graphene. *Nature* 438, 197-200 (2005).

2. Y. Zhang, Y.W. Tan, H. L. Stormer, and P. Kim: Experimental observation of the quantum Hall effect and Berry's phase in graphene. *Nature* 438, 201-204 (2005).

3. A. K. Geim and K. S. Novoselov: The Rise of Graphene. *Nature Materials* 6, 183-191 (2007).

4. S. Butler, S. M. Hollen, L. Cao, Y. Cui, J. Gupta, H. R. Gutierrez, T. F. Heinz, S. S. Hong, J. Huang, A. F. Ismach, E. Johnston-Halperin, M. Kuno, V. V. Plashnitsa, R. D. Robinson, R. S. Ruoff, S. Salahuddin, J. Shan, L. Shi, M. G. Spencer, M. Terrones, W. Windl, and J. E. Goldberger: Progress, Challenges, and Opportunities in Two-Dimensional Materials Beyond Graphene. *ACS Nano* 7, 2898-2926 (2013).

5. I. V. Pinchuk, P. M. Odenthal, A. S. Ahmed, W. Amamou, J. E. Goldberger, and R. K. Kawakami: Epitaxial Co-Deposition Growth of $CaGe_2$ Films by Molecular Beam Epitaxy for Large Area Germanane. *Journal of Materials Research* 29, 410-416 (2014).

6. E. Bianco, S. Butler, S. Jiang, O. Restrepo, W. Windl, and J. E. Goldberger: Stability and Exfoliation of Germanane: A Germanium Graphane Analogue. *ACS Nano* 7, 4414-4421 (2013).

7. Y. Kato, R. C. Myers, A. C. Gossard, and D. D. Awschalom: Coherent Spin Manipulation Without Magnetic Fields in Strained Semiconductors. *Nature* 427, 50-53 (2004).

8. Y. K Kato, R. C. Myers, A. C. Gossard, and D. D. Awschalom: Observation of the spin Hall effect in semiconductors. *Science* 306, 1910-1913 (2004).

9. M. Konig, S. Wiedmann, C. Brune, A. Roth, H. Buhmann, L. W. Molenkamp, X.-L. Qi, and S.-C. Zhang: Quantum Spin Hall Insulator State in HgTe Quantum Wells. *Science* 318, 766-770 (2007).

10. Wang, Y., *et al.* Electrochemical delamination of CVD-grown graphene film: toward the recyclable use of copper catalyst. *ACS Nano* 5, 9927-9933 (2011).

11. Ren, W. C., Gao, L. B., Ma, L. P. & Cheng, H. M. A method for the non-destructive transfer of graphene at a low cost. Chinese patent 201110154465.9 (2011).

12. L. Gao, W. Ren, H. Xu, L. Jin, Z. Wang, T. Ma, L.-P. Ma, Z. Zhang, Q. Fu, L.-M. Peng, X. Bao, H.-M. Cheng: Repeated growth and bubbling transfer of graphene with millimetre-size ingle-crystal grains using platinum. *Nat. Comm*. 3, 699 (2012).

13. J. J. Harris, B. A. Joyce, and P. J. Dobson: Oscillations in the Surface Structure of Sn-doped GaAs During Growth by MBE. *Surf. Sci. Lett.* 103, L90-L96 (1981).

14. J. H. Neave, B. A. Joyce, P. J. Dobson, and N. Norton: Dynamics of Film Growth of GaAs by MBE from RHEED Observations. *Appl. Phys. A* 31, 1-8 (1983).

15. R. W. Ulbricht, A. Schmehl, T. Heeg, J. Schubert, and D. G. Schlom: Adsorption-controlled growth of EuO by molecular-beam epitaxy. *Appl. Phys. Lett.* 93, 102105 (2008).

16. G. Zhang, H. Qin, J. Teng, J. Guo, Q. Guo, X. Dai, Z. Fang, and K. Wu: Quintuple-layer epitaxy of thin films of topological insulator Bi_2Se_3. *Appl. Phys. Lett.* 95, 053114 (2009).

17. A. G. Swartz, J. Ciraldo, J. J. I. W. Wong, Y. Li, W. Han, T. Lin, S. Mack, D. D. Awschalom, and R. K. Kawakami: Epitaxial EuO thin films on GaAs. *Appl. Phys. Lett.* 97, 112509 (2010).

18. A. Palenzona, P. Manfrinetti, and M. L. Fornasini: The phase diagram of the Ca-Ge system. *J. Alloys Compd.* 345, 144-147 (2002).

19. S. Bae, H. Kim, Y. Lee, X. Xu, J. Park, Y. Zheng, J. Balakrishnan, T. Lei, H. R. Kim, Y. Song, *et al.*: Roll-to-Roll Production of 30-Inch Graphene Films for Transparent Electrodes. *Nat. Nanotechnol.* 5, 574-578 (2010).

20. X. S. Li, Y. W. Zhu, W. W. Cai, M. Borysiak, B. Han, D. Chen, R. D. Piner, L. Colombo, R. S. Ruoff: Transfer of Large-Area Graphene Films for High-Performance Transparent Conductive Electrodes. *Nano Lett.* 9, 4359-4363 (2009).

21. Y. Lee, S. Bae, H. Jang, S. Jang, S. Zhu, S. H. Sim, Y. Song, B. H. Hong, J. Ahn: Wafer-Scale Synthesis and Transfer of Graphene Films. *Nano Lett.* 10, 490-493 (2010).

22. G. Vogg, M. S. Brandt, and M. Stutzmann: Polygermyne – a prototype system for layered germanium polymers. *Adv. Mater.* 12, 1278-1281 (2000).

Early Versus Late Bilingual Interhemispheric Interactions

John Simon S. Pangilinan, Tammie M. Tran, Corrin E. Saenz, Monica E. Youssef, Tanya J. Tran, Adam D. Felton, David Vazquez, Adam J. Daily, and Christine Chiarello

Department of Psychology

ABSTRACT

Current research generally accepts that language is specialized in the left hemisphere for right-handed monolinguals and late bilinguals, yet those who acquired two languages before the age of 6 showed bilateral hemispheric involvement for both languages The current study sought to determine the degree to which each hemisphere is involved in early and late bilingual lexical processing and it was predicted that early bilinguals would have a bilateral language advantage as compared to late bilinguals. Sixty-four undergraduate students (32 early and 32 late bilinguals) aged 18-31 performed a lexical decision task (LDT) to discern between Spanish word and non-word stimuli. It was found that within both groups of bilingual speakers, processing in the left hemisphere was faster and more accurate than the right hemisphere. However, only weak support was found between early-and-late bilinguals on reaction time but not on accuracy. Future studies can address native language fluency and interhemispheric differences between monolinguals and early and late bilinguals and multilinguals.

Keywords: language, lexical decision task, early versus late bilingualism

AUTHOR

John Simon S. Pangilinan

Department of Psychology

John is a 4th year Anthropology and Psychology major. John is passionate about helping others and research. He is currently involved with hospital administration and he aims to make that his career. At UCR, John acquired hands-on experience in cognitive n euroscience research while working with Dr. Christine Chiarello, Adam Felton, Adam Daily, and David Vazquez. He thanks everyone involved for their invaluable help and support.

FACULTY MENTOR

Christine Chiarello

Department of Psychology

Through her Cognitive Neuroscience laboratory, Professor Chiarello investigates brain organization for language, with a focus on individual differences in cortical anatomy. The primary methodologies are using measurements of neuroanatomical features obtained from structural MRI scans; and behavioral investigations using the divided visual field techniques, as well as experimental and standardized language, implicit grammatical learning, creativity, executive functioning and reading tasks.

CO-AUTHORS

Corrin E. Saenz, Tammie M. Tran, Monica E. Youssef, Tanya J. Tran (not pictured)

INTRODUCTION

Language for right-handed monolinguals is more specialized in the left hemisphere than the right hemisphere (Gazzaniga 1970); yet both hemispheres communicate with each other via the corpus callosum (Gazzaniga 2000). Moreover, the representation of two languages is different in anatomical distribution (Lucas, McKhann, & Ojemann, 2004). Hull and Vaid (2007) found that early bilinguals, those who acquired two languages before the age of 6, showed bilateral hemispheric involvement for both languages acquired. They also found that monolinguals and late bilinguals, those who acquired a second language after age 6, showed left hemispheric dominance for both languages.

Genesee et al. (1978) defined early bilingualism as having acquired a second language before or around 5 years old; they used an EEG to record participants' brain activity as the participant discerned between English and French words; and found that late bilinguals adopted different processing strategies to accomplish the same task as compared to childhood bilinguals. Adolescent bilinguals used a right hemisphere-based and gestalt-like (processed as a whole) strategy to categorize stimulus words and tell the languages apart. Childhood and infant bilinguals may have used a left hemisphere-based and semantic (word meaning) processing strategy (Genesee et al., 1978).

Early bilinguals were found to process language bilaterally, whereas late bilinguals and monolinguals process language in the left hemisphere (Peng & Wang, 2011). The Composition-Age (CA) model stated that a common Chinese character is processed as a whole in the right hemisphere while English alphabetic words, or Chinese multiple-character words, are synthesized in the left hemisphere (Peng & Wang, 2011). Furthermore, the CA model emphasized the bilateral language processing of early bilinguals.

Peng and Wang (2011) acknowledged that the acquisition and similarity of writing systems such as alphabetic, syllabic, and logosyllabic, could impact hemispheric lateralization. Peng and Wang (2011) tested their model with 14 late Chinese-English bilingual participants that were subjected to a Stroop task to indicate the color of the Chinese-character, and not the written color of the Chinese-character (Peng & Wang, 2011; Stroop, 1935). They found a stronger Stroop effect with Stroop stimuli presented to the right visual field/left hemisphere than the left visual field/right hemisphere for the late bilingual speakers. Therefore, the Stroop stimuli processing was dominated by the left hemisphere for the late bilingual speakers. Peng and Wang (2011) did not compare the late bilingual speakers to early bilinguals.

The current study sought to address the degree to which each hemisphere is involved in early and late bilingual lexical processing by expanding on the findings of Peng and Wang (2011) for early-and-late Spanish bilinguals. The left hemisphere is generally dominant for language processing in right-handed monolinguals, but it is predicted that early bilinguals will have a more bilateral language advantage as compared to late bilinguals.

METHOD

Participants

Participants for the study consisted of 64 undergraduate students (23 males; 41 female; and 32 late bilinguals) with ages ranging 18 to 31 (mean age of 19.4 years) with normal or corrected-to-normal vision. Participants were verified to be proficient both in English and Spanish. Bilinguals were considered "early" if they acquired both languages by the age of 5 and "late" if after the age of 5 (Genesee et al., 1978). All participants were prescreened for right-handedness, as measured by the Edinburgh Handedness Inventory (Oldfield, 1971). Participation was voluntary or served as a partial course credit for an introductory psychology class.

Materials

The experiment was performed on a Macintosh PowerMac G4 computer running OS X. Participants were seated approximately 60 cm in front of a 17" computer monitor. A headrest stabilized and maintained participant head position.

The target stimuli were created by choosing high frequency Spanish nouns. The stimuli were presented in an uppercase, black Helvetica 22-point font on a white background. The non-word stimuli were created by changing one letter of a Spanish noun unused in the word stimuli. This ensured that the non-word stimuli appeared similar to the word stimuli and were pronounceable. PsyScope software controlled the presentation of stimuli and recorded participant responses (Cohen, MacWhinney, Flatt, & Provost, 1993). Participants' responses were registered using an ioLab USB button response box.

Design and Procedure

Participants were presented with an informed consent form, Edinburgh Handedness Inventory, and language history questionnaire. Participants were placed in a sound isolated room. Participants performed a Lexical Decision Task (LDT) task to distinguish quickly and accurately Spanish words from non-words. To formulate the lexical decision, participants determined whether the target is a word by pressing a button indicating the decision made. For the present study, they pressed one button if a Spanish word was recognized and pressed another for a non-word. Spanish words and non-words were presented either to the left visual field (right hemisphere) or the right visual field (left hemisphere).

Participants were acquainted with the task through 10 demonstration (10 stimuli) and practice trials (40 stimuli). Next, three blocks containing 80 stimuli each was presented to the participants. Participants received a break at the end of each block. The stimuli were randomized within each block and counterbalanced across visual fields. For example, half the participants received a Spanish word "PIÑA" in the left visual field and half received it in the right.

The main procedure was adapted from Peng and Wang (2011) with a substitution of Spanish words or non-words as the main stimuli. Visual stimuli presented to the left of a participant's visual field is transmitted to the visual cortex at the back of the right hemisphere while visual stimuli presented to the right of a participant's visual

field is transmitted to the visual cortex at the back of the left hemisphere (Banich, 2003). As such, each trial was designed to present a white screen with a flickering black central fixation "+" for 30 milliseconds (ms). Then the fixation was replaced by a blank screen for 50 ms. The fixation then reappeared for another 300 ms, followed by the stimulus screen for 125 ms presented either to the left or right visual field. The central fixation remained 175 ms after presenting the stimuli. Participants were instructed to respond as quickly and as accurately as possible and had 2000 ms to respond. A lack of response would be considered a "Timeout" with no reaction time or accuracy score recorded; after an additional 250 ms, the fixation '+' appeared to indicate the start of the next trial. Participants were instructed to maintain a fixation on the "+" for the duration of the LDT.

After the LDT, a 10 minute Spanish Proficiency Test, a sample test of grammar and vocabulary adapted from the Spanish Level B1 European Language Certificate, was provided at the end of the study as a supplemental check on Spanish fluency and comprehension (Telc, 2013). Participants completed the experiment in one hour.

RESULTS

The mean proportion of correct responses (accuracy) and reaction time (ms) for visual field and acquisition is shown in Table 1. A 2 x 2 mixed factorial analysis of variance (ANOVA) was conducted on age of acquisition (Early and Late) and visual field (Left Visual Field, LVF; Right Visual Field, RVF). Reaction times (ms) and the proportion of words and non-words identified (accuracy) was assessed in all conditions. A significant main effect was found for visual field on reaction time and accuracy. The reaction time for RVF ($M = 956$, SD = 179) was faster than the reaction time for LVF ($M = 991$, SD = 198), $F(1,62) = 19.814$, $p < .001$, $\eta_p^2 = .242$. Additionally, the accuracy for the RVF ($M = .720$, SD = .105) was greater than the accuracy for the LVF ($M = .645$, SD = .089), $F(1,62) = 46.649$, $p < .001$, $\eta_p^2 = .429$.

John Simon S. Pangilinan

Table 1. *Means of Reaction Time and Accuracy by Age of Acquisition and Visual Field on Reaction Time (ms) and Accuracy (Proportion of Word and Non-Words Correctly Identified).*

Measure	Age of Language Acquisition	Visual Field	Mean *(M)*	*Standard Error of the Mean (SE)*
Reaction Time	Early	LVF	953	35
		RVF	916	31
	Late	LVF	1028	35
		RVF	995	31
Accuracy	Early	LVF	0.659	0.016
		RVF	0.738	0.018
	Late	LVF	0.632	0.016
		RVF	0.703	0.018

A marginally significant effect was found for language acquisition age on reaction time. The reaction time for early bilinguals ($M = 935$, $SD = 145$) was faster than late bilinguals ($M = 1012$, $SD = 216$), $F(1,62) = 2.828$, $p = .098$, $\eta_p^2 = .044$. However, there was no main effect found for language acquisition age on accuracy between early bilinguals ($M = .698$, $SD = .086$) and late bilinguals ($M = .667$, $SD = .086$), $F(1,62) = 2.016$, $p < .161$, $\eta_p^2 = .031$.

An interaction was not found between visual field and language acquisition age for reaction time (Figure 1), $F(1,62) = .058$, $p = .811$, $\eta_p^2 = .001$. Moreover, an interaction was not found between visual field and language acquisition for accuracy (Figure 2), $F(1,62) = .118$, $p = .733$, $\eta_p^2 = .002$). For LVF trials, a one-way ANOVA on accuracy found no difference on language acquisition

age on accuracy, $F(1,63) = 1.450$, $p = .233$. Similarly, for RVF trials, there was no significant results in regards to acquisition age in the RVF on accuracy, $F(1,63) = 1.752$, $p = .191$. For reaction time, the LVF did not differ between acquisition groups, $F(1,63) = 2.362$, $p = .129$, but for RVF trials there was a marginally significant difference between acquisition age on reaction time with early bilinguals being faster than late bilinguals, $F(1,63) = 3.231$, $p = .077$.

DISCUSSION

The current study sought to assess the degree to which each hemisphere is involved in early-and-late bilingual lexical processing as quantified by reaction time and accuracy differences. It was predicted that early bilinguals would have a more bilateral language advantage as compared to
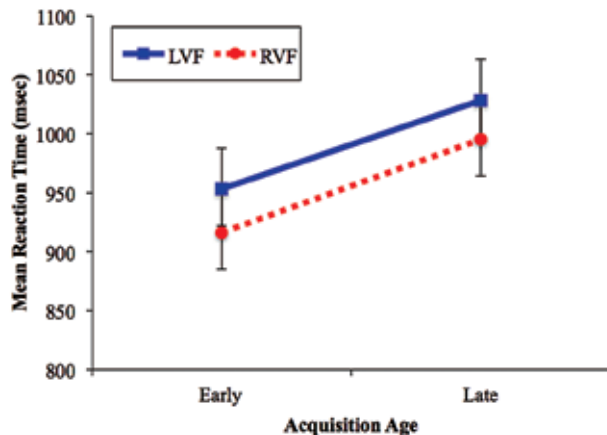
Figure 1. Hemispheric differences of mean reaction times (ms) between early and late bilinguals.
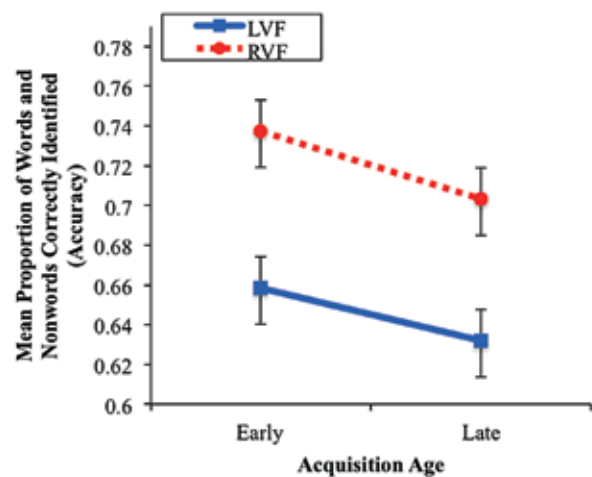
Figure 2. Hemispheric differences of proportion of words and non-words correctly identified (accuracy) between early and late bilinguals.

late bilinguals. The present study neither found such results nor fully supported earlier literature.

However, the present study found early-and-late bilingual differences. Similar to Genesee et al. (1978) and Peng and Wang (2011), the findings of the current study did find a difference between the left and right hemispheres of bilingual speakers with the left hemisphere (RVF) being faster and more accurate than the right hemisphere (LVF). Furthermore, the current study found weak evidence that early bilinguals were faster at identifying words and non-words correctly than late bilinguals, thereby marginally supporting the results of Genesee et al. (1978) and Peng and Wang (2011).

Despite the results of the present study, it was limited in its small sample size. Nevertheless, a potential confound of this study could be that some early and late bilingual participants were multilingual and knew more than two languages. Moreover, English fluency was not thoroughly assessed. As mentioned, Genesee et al. (1978) and Peng and Wang (2011) exhibited the impact of acquiring just two languages between early and late bilinguals. However, acquiring more than two languages early and later in life could be associated with different patterns of brain activation and processing strategies (Vingerhoets et al., 2003).

There are inconsistent results in the literature of multiple languages being localized across various parts of the brain. Vingerhoets et al. (2003) found multiple languages are overlapped in the same brain regions and suggested that acquiring multiple languages requires extensive recruitment of other brain regions for each additional language when compared to the native language. Future studies can address native language fluency and interhemispheric differences between monolinguals and early and late bilinguals and multilinguals.

REFERENCES

Banich, M. T. (2003). The Divided Visual Field Technique in Laterality and Interhemispheric Integration. *Experimental Methods in Neuropsychology*, *21*, 47-63.

Cohen J.D., MacWhinney B., Flatt M., and Provost J. (1993). PsyScope: A new graphic interactive environment for designing psychology experiments. *Behavioral Research Methods, Instruments, and Computers*, *25*(2), 257-271.

Gazzaniga, M. S. (1970). *The bisected brain*. New York: Appleton-Century-Crofts.

Gazzaniga, M. S. (2000). Cerebral specialization and interhemispheric communication: Does the corpus callosum enable the human condition. *Brain*, *123*, 1293–1326.

Genesee, F., Hamers, J., Lambert, W. E., Mononen, L., Seitz, M., & Starck, R. (1978). Language processing in bilinguals. *Brain and Language*, *5*, 1-12.

Hull, R., & Vaid, J. (2007). Bilingual language lateralization: A meta-analytic tale of two hemispheres. *Neuropsychologia*, *45*, 1987–2008.

Lucas, T. H., McKhann, G. M., & Ojemann, G. A. (2004). Functional separation of languages in the bilingual brain: a comparison of electrical stimulation language mapping in 25 bilingual patients and 117 monolingual control patients. *Journal of Neurosurgery*, *101*(3), 449-457.

Oldfield, R.C., 1971. The assessment and analysis of handedness: The Edinburgh Inventory. *Neuropsychologia*, *9*, 97–113.

Peng, G., & Wang, W. S. Y. (2011). Hemisphere lateralization is influenced by bilingual status and composition of words. *Neuropsychologia*, *49*, 1981-1986. doi: 10.1016/j.neuropsychologia.2011.03.027.

Stroop, J. (1935). Studies of interference in serial verbal reactions. *Journal of Experimental Psychology, 18*, 643–662.

Telc. (2013). Modelo de examen 1. *Telc Español B1*. Retrieved 3 April 2013, from http://www.telc.net/en/what-telc-offers/spanish/telc-espanol-b1/.

Vingerhoets, G., Borsel, J. V., Tesink, C., van den Noort, M., Deblaere, K., Seurink, R., Vandemaele, P., & Achten, E. (2003). Multilingualism: an fMRI study. *NeuroImage*, *20*, 2181-2196. doi: 10.1016/j.neuroimage.2003.07.029.
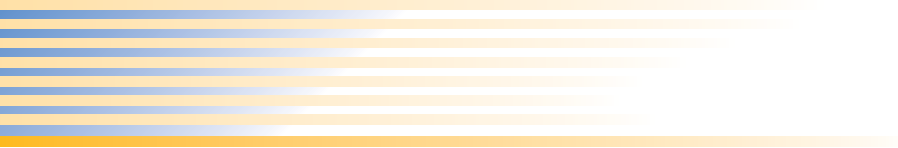
Optimization of Semi-Permeable Conductive Carbon Nanotube-Polymer Thin Films

Julianne Rolf, Kyle Russell, Alexander Dudchenko, and David Jassby

Department of Chemical and Environmental Engineering

ABSTRACT

Membrane bio reactors (MBRs) are becoming the treatment method of choice for wastewater treatment utilities and small-scale wastewater treatment operations. MBRs have a reduced physical footprint, produce higher effluent quality and allow for a greater degree of automation, making these systems preferable to conventional activated sludge wastewater treatment processes. Incorporating a membrane directly into the activated sludge process offers significant advantages such as maintaining a higher microbial concentration and eliminating the need for a clarifier at the end of the wastewater treatment process. MBR performance is inhibited due to bio fouling, where bacteria irreversibly attach to the membrane surface. Air bubbling and turbulent flow are currently used to minimize membrane fouling due to bacteria, but are costly and cannot remove all of the surface bacteria. The application of an electrical potential to a surface has been shown to effectively inhibit biofilm formation. This technology can be applied to MBRs through the use of semi-permeable, electrically conductive thin films. These thin films have been prepared from Poly(vinyl alcohol) and functionalized multi-wall carbon nanotubes that were deposited on industrial membrane supports using a pressure deposition technique. The effect of the cross-linking agent and reaction temperatures on the strength and conductivity of the membranes was studied. Changes in resistivity were used as an indicator of membrane stability under an electrical field through the use of a model flow cell. Highly conductive and robust thin films were developed from this study that could be used in MBRs to eliminate the need for turbulent flow.

Keywords: carbon nanotubes (CNTs); poly(vinyl) alcohol (PVA); membrane; thin film; resistivity; flux

MENTOR

David Jassby

Department of Chemical and Environmental Engineering

Before joining UC Riverside, Professor Jassby was the Executive Director of the Center for the Environmental Implications of NanoTechnology (CEINT) at Duke University. His research focuses on water treatment technologies, environmental microbiology, and membrane separations. David hails from Israel, a country well acquainted with challenging water issues and innovative, technology-driven, solutions.

AUTHORS

Julianne Rolf

Department of Chemical and Environmental Engineering

Julianne Rolf is a junior in Environmental Engineering. As a UC LEADS scholar, she has participated in research in Dr. David Jassby's laboratory since June 2013. Julianne is a member of the University Honors Program, Vice President of Engineers without Borders, and Community Service Co-Captain of Tau Beta Pi, California's Alpha Beta Chapter.

Kyle Russell

Department of Chemical and Environmental Engineering

Kyle Russell is a graduating senior majoring in Environmental Engineering. Kyle was a founding member of various UCR organizations including the Air and Waste Management Association and Vertical Ascent Rock-climbing Club. Kyle plans to join the workforce as a civil engineer in California after graduation.

INTRODUCTION:

Membrane bio reactors (MBRs) are quickly becoming the treatment method of choice for wastewater treatment utilities and small-scale wastewater treatment operations. [1] However, MBR performance is inhibited due to bio fouling, where bacteria irreversibly attach to the membrane surface. [2] Air bubbling and turbulent flow are currently used to minimize the membrane fouling due to bacteria, but are very costly and cannot remove all of the bacteria from the surface. [3] The application of an electrical potential to a surface has been shown to effectively inhibit biofilm formation. [4-6] This technology can be applied to MBRs through the use of semi-permeable, electrically conductive thin films. In this study, the optimal combination of PVA, a soluble thermoplastic resin, and carbon nanotubes (CNTs) with an affective cross-linking agent was sought to create a stable and conductive membrane that can be used in MBRs.

METHODS

Membrane Synthesis for Resistance and Flux Testing

The support used in this study was PS35, a polymer support manufactured by Sepro Membranes (Oceanside, CA), that allows for conductive CNTs to be deposited across the top of it. The support was cleaned with deionized (DI) water to remove any unwanted particles before the PVA and CNTs can be deposited. The PVA and CNTs were deposited on the membrane surface using a pressure deposition device. Two CNT solutions were used in this study. One consisted of just DI water and CNTs while the other was pretreated. The pretreated solution contained CNTs, succinic acid, and hydrochloric acid (HCl) and heated for one hour at 80°C. After the deposition process, the membrane was soaked in the cross-linking agent, which consisted of sulfuric acid and hydrochloric acid, for ten minutes and then heated in the solution for the designated amount of time and at the designated temperature.

All the membranes contained 8.9 milligrams of CNTs across the 142 millimeter diameter membrane. Membranes A, B and C contained 0.5 milliliters of PVA while Membrane D contained 0.25 milliliters of PVA. Membranes A and D were heated for four hours at 80°C. Membrane B was heated for two hours at 80°C and then two more hours at

120°C. The CNT solution was pretreated with 0.2 grams of succinic acid and 0.1 milliliters of hydrochloric acid and heated at 80°C before it was deposited. Then the CNT solution was deposited before the membrane was soaked in the cross-linking solution and heated to 120°C. The components of each CNT membrane are summarized in Table 1. As seen in Figure 1, the CNT membrane is black in color after the total CNT synthesis with the white PS 35 support underneath. Scanning electron microscope (SEM) images of the membrane can be seen in Figures 2 and 3.

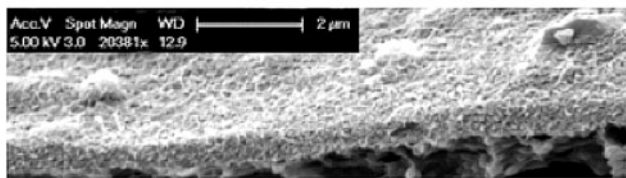**Table 1:** *Membranes for Resistance and Flux Testing*

Membrane	PVA (mL)	CNT Solution (mL)	Heat Time (hrs/Temperature)
A	0.5	75	4/80°C
B	0.5	75	2/80°C, 2/120°C
C	0.5	75 (pretreated)	2/120°C
D	0.25	75	4/180°C

Figure 1: *PS35 support (left, white) and CNT membrane on a PS35 support (right, black with white ring) (scale bar is 12 cm).*
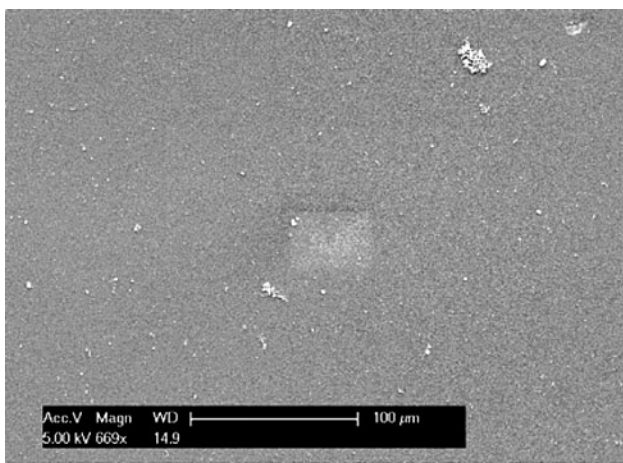
Figure 2: *Top section view of a SEM image of membrane with PVA and CNTs on a PS35 support (scale bar is 100 μm).*

Figure 3: Cross section view of a membrane with PVA and CNTs (scale bar is 2 μm).

Membrane Synthesis and FTIR Testing

Similarly to the membranes used for resistance and flux testing, the membranes for Fourier Transform infrared spectroscopy (FTIR) testing (PVA-CNT-SA-H, PVA-CNT-SA, PVA-CNT) were made with the PS35 polymer support. For all three membranes for this test, the support was cleaned with DI water before deposition, and the same amount of CNTs and PVA were deposited on each one. To identify the effects of heating the membrane and soaking it in the cross-linking solution, the three membranes were either soaked in water or the cross-linking solution and they were either heated or not heated. Membrane PVA-CNT-SA-H was soaked in the cross-linking solution with the succinic acid (SA) and heated for four hours at 80°C. Membrane PVA-CNT-SA was only soaked in the cross-linking solution while membrane PVA-CNT was only soaked in water. All three membranes were dried at room temperature before taking the FTIR samples.
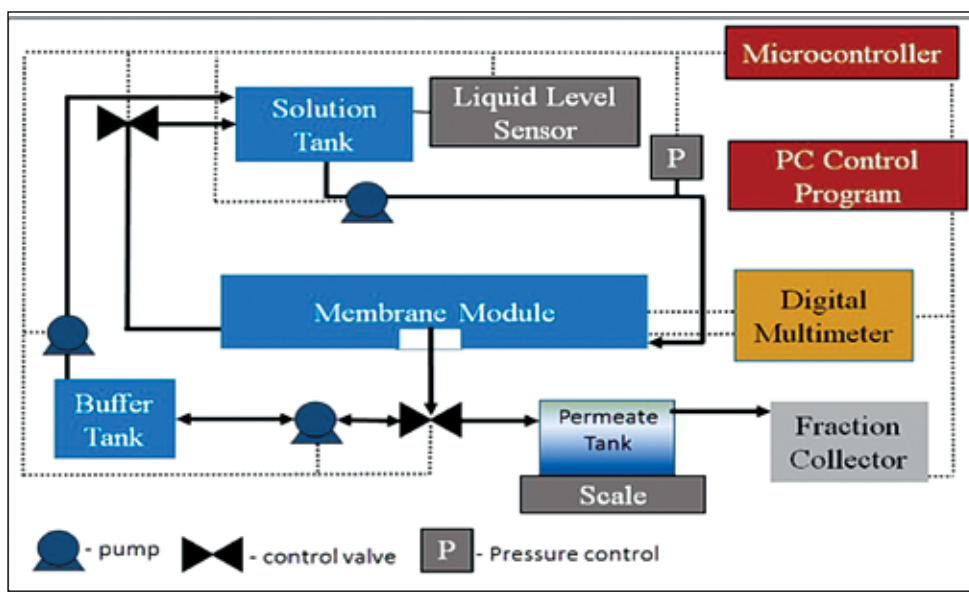
Testing the Membrane

The system used to test the membrane was developed to measure the electric resistance and calculation of resistivity. The system has three main parts: scale, flow cell, and solution tank. The solution tank contained DI water, which was used in the system to conduct the resistance and flux test. A pump was used to move the water through the system into the flow cell. The flow cell contained the membrane, which could have a voltage applied to it so the resistance could be measured. In the flow cell, the cross-sectional flow occurred with high pressure forcing the water through the membrane. The filtered water then moved into the container on the scale. The scale measured the change in mass, which was used to determine the flux. An overview of the membrane testing apparatus can be seen in Figure 4.

DISCUSSION AND RESULTS

Cross-Linking Reaction

The cross-linking solution contained succinic acid as the cross-linking agent, and hydrochloric acid (HCl), the catalyst. Succinic acid links the polymer strands by immobilizing CNTs within the polymer PVA through the creation of ester bonds between hydroxyl and carboxyl groups on the CNT and PVA; this process results in the alteration of the spacing between the PVA and CNTs.


Figure 4: Schematic of the membrane testing process.
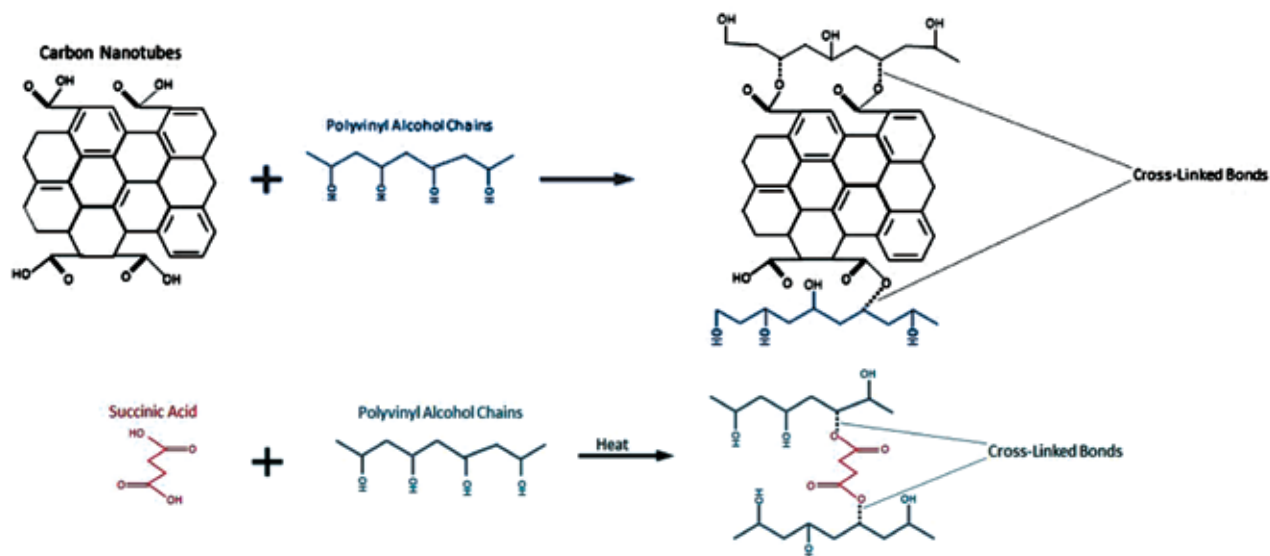
Figure 5: Cross-linking of PVA chains, CNT, and succinic acid through reactions with PVA's hydroxyl groups to immobilize CNT within the PVA chain polymer.

[5] The carbon nanotubes' hydroxyl group reacts with the PVA's hydroxyl to form a covalent bond between carbon and oxygen. The combination of these bonds results in the CNTS being immobilized within the PVA as shown in Figure 5.

The FTIR spectrum of the membrane material can be seen in Figure 6. The peaks in the 1015-1200 cm^{-1} range signify C-OH bonds in alcohols. Membrane PVA-CNT-SA-H, which was soaked in cross-linking solution and heated, has lower intensity peaks in this range. This is due to the C-OH group becoming C-O-C when the CNT cross-links with the PVA. Furthermore, the peak for membrane PVA-CNT-SA-H at 1243 cm^{-1}, which is associated with the C-O-C group, is stronger than the peak for membranes PVA-CNT-SA and PVA-CNT, which were not heated. This indicates that more cross-linking bonds formed when the membrane was heated.
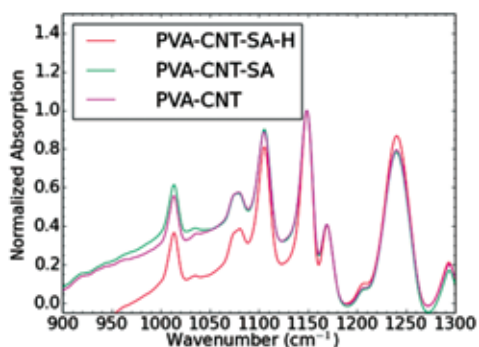
Figure 6: FTIR data for carbon nanotubes membranes.

Membrane Quality

It is preferential for a membrane to have a low electrical resistivity so the current drop across the membrane is minimized. The resistivity should stay constant, which indicates a stable membrane. The permeate flux of a membrane needs to be large enough to keep up with the growing demand for water. Thus, it is important to develop membranes with high flux, low resistivity and high stability. According to Figure 7, Membrane B, which was heated at 80°C for two hours and 120°C for two more hours, has the lowest resistivity around 25 ohms-meter; this membrane resistivity was stable over time. Membrane C, which had the pretreated CNT solution with succinic acid and hydrochloric acid, has the highest resistivity at about 240 ohms-meter. Membrane C has a higher resistivity because the heating time was limited. As a result, less CNTs were cross-linked and a greater number of CNTs lost allowed a greater flux and resistivity over time. In comparison to membrane C, membrane B was heated for twice as long so it has a smaller resistivity. Membrane D had half the amount of PVA as membrane A while both were heated for four hours at 80°C. Having less PVA in membrane D led to a decreased amount of cross-linked CNTs, this allowed for CNT lost and a lack of mobilization. This loss of CNTs caused a greater flux and resistivity over time.
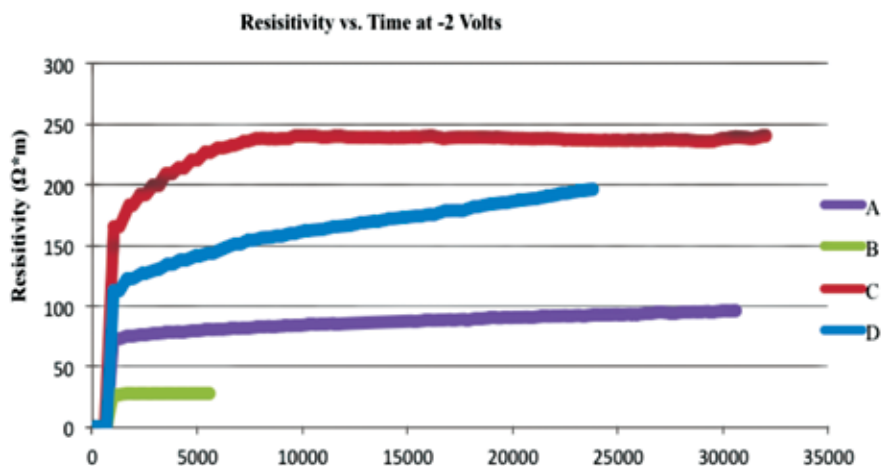
Figure 7: Graph of resistivity change of membrane during experimentation with electrical potential difference of -2 volts. (Membrane A: Heated for 4 hours at 80°C; Membrane B: Heated for 2 hours at 80°C and 2 more hours at 120°C; Membrane C: CNT solution was pretreated and heated at 80°C for 2 hours and the membrane was heated for 2 hours at 120°C; Membrane D: Heated for 4 hours at 80°C)

The pressure was kept constant and the flux was measured over time to determine the effect of the electrical potential on membrane fouling. As seen in Figure 8, the flux of membrane C is about 27 $g/m^2 \cdot s$, which is the largest flux at -2 volts electrical potential. Membrane B has the lowest flux, which was caused by to the increased heating time and temperature allowing for a greater number of cross-linked CNTs. The increased number of cross-linked and immobilized CNTs limits the flux and the PVA crystallization increases the resistivity. With the lack of expansion, the permeability is unable to increase. In comparison, the crystalline structure development in membrane C was limited by the shortened heating time. Membrane D has a high flux because it has less PVA to hold the CNTs together, thus the permeability is much higher than for membrane A.

CONCLUSION

All factors need to be considered before determining the ideal membrane. Having a membrane with a low, stable resistivity and a high flux is crucial for these membranes to be applicable in MBRs for treating wastewater. Of Membranes A through D, Membrane C shows the most promise so far in treating wastewater. This is due to the PVA having greater pore expansion capabilities when the CNT solution was pretreated. Decreasing the amount of PVA caused the electrical resistivity to increase while increase the heating temperature for the same amount time resulted in the flux decreasing significantly. Further investigation into pretreatment synthesis and crystallization time could potentially yield membranes with the desired flux and resistivity.
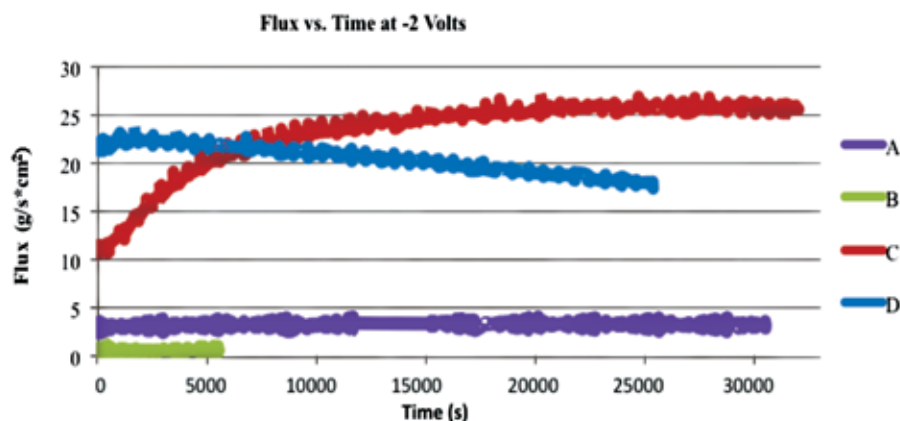
Figure 8: Membrane flux during experiment electrical potential difference of -2 volts.

ACKNOWLEDGEMENTS

REFERENCES

[1] P. Le-Clech, V. Chen, T. Fane, Fouling in membrane bioreactors used in wastewater treatment, J. Membr. Sci. 284 (2006) 17-53.

[2]   H. Huotari, I. Huisman, G. Trägårdh, Electrically enhanced crossflow membrane filtration of oily waste water using the membrane as a cathode, J. Membr. Sci. 156 (1999) 49-60.

[3] Z. Cui, S. Chang, A. Fane, The use of gas bubbling to enhance membrane processes, J. Membr. Sci. 221 (2003) 1-35.

[4] S. Hong, J Jeong, S. Shim, H. Kang, S. Kwon, K. Ahn, J. Yoon, Effect of electric currents on bacterial detachment and inactivation, Biotechnol. Bioeng. 100 (2008) 379-386.

[5] CF. de Lannoy, D. Jassby, D. Davis, M. Wiesner, A highly electrically conductive polymer–multiwalled carbon nanotubes nanocomposite membrane, J. Membr. Sci. 415-416 (2012) 718-724.

[6] H.M. Huotari, I.H. Huisman, G. Tragardh, Electrically enhanced cross flow membrane filtration of oily waste water using the membrane as a cathode, J. Membr. Sci. 146 (1999) 49-60.

Two Faces of Dimethoxyalkanes: Steric Repulsion and Hyperconjugative Stabilization

Erik Romero[1], Brittany Nguyen[2], Juan Sanabria[3], Erika Varady[2], I-Chieh Wang[4], and Thomas Hellman Morton[1]

[1]*Department of Chemistry, [2]Department of Biology, [3]Department of Cell Biology and Neuroscience, [4]Department of Biochemistry*

ABSTRACT

Previous research has explored whether steric effects play the major role in determination of conformational stability, or if there are major factors to consider. One example is 1,2-difluoroethane, where the two fluorine atoms can be either synclinal (approximately 70º dihedral angle) or antiperiplanar (180º dihedral angle) to each other. This becomes a question of whether steric interactions, hyperconjugative, or dipole-dipole and dipole-induced dipole interactions have the largest influence on conformational energies. To determine which of these theories provide a better model, 1-propanol was examined in its neutral and conjugate acid ion forms using the Gaussian 09 program suite. If steric interactions play the larger role, the conjugate acid ion should prefer to be in the antiperiplanar configuration. By contrast, the result has shown that the synclinal conformation is even more favored in the cation than in the neutral alcohol. This finding is consistent with a hyperconjugative model, rather than steric attraction. This research further investigates the extent to which dipole-dipole and dipole-induced dipole interactions are to be weighed in comparison to steric interactions. Through examination of 1,7-dimethoxyheptane, and its isomers, we use DFT (at the B3LYP/6-31G** level) to compare the energetic effects of four types of non-nearest neighbor steric interactions and one electrostatic interaction to ultimately determine whether these effects are additive. Using multiple regression analysis, the outcome shows that of the five interactions examined, three are destabilizing and one is stabilizing. In agreement with previous research, the effects of steric and electrostatic interactions are not additive.

Keywords: magnesium, degradation, corrosion, impedance pump, flow device, mass, pH

FACULTY MENTOR

Tom Morton

Department of Chemistry

Professor Morton's areas of research cover organic chemistry, chemical biology, and computational chemistry. His research consists of concurrent studies of organic reactions in the gas phase and in biological receptors. In this work he and his team make use of (and in some cases, have invented) new techniques in mass spectrometry, as well as novel methods for tagging and purifying receptors.

AUTHOR

Erik Romero

Department of Chemistry

Erik Romero, is a senior in Chemistry and is currently supported by a MARCU fellowship). He, along with Brittany Nguyen, J.C. Sanabria, Jack Wang, and Erika Varady, have analyzed the computations performed by all the Chem 122H students during Fall 2013, to answer systematic questions regarding the shapes of organic molecules and the extent to which pairwise, intramolecular interactions can be simply added together to predict relative stabilities.

CO-AUTHORS

Brittany Nguyen, J.C. Sanabria, Erika Varady, Jack Wang

INTRODUCTION

Every atom has an electronic density and occupies a certain amount of space within a molecule. Often, when two atoms are located in close proximity, unfavorable interactions occur as result of electron-electron repulsions, called steric effects if the affected atoms are not neighbors of one another. One well-known case involves repulsive effects that are referred to as *gauche* interactions. *Gauche* interactions occur when carbons 4 atoms apart are positioned close enough in space that their respective hydrogens repel one another. This represents an example of a pairwise, steric interaction between atoms that are not neighbors.

In other instances, pairwise interactions appear to produce a stabilizing effect. Such is the case with 1,2-difluoroethane. Looking solely at dipole-dipole repulsion and steric interactions for determining an ideal geometry, one would expect the preferred conformation of 1,2-difluoroethane to be antiperiplanar (180°); yet, the favored conformation (99:1) of 1,2-difluoroethane positions the fluorine atoms synclinal to one another, with a dihedral angle of approximately 70°. The stability of the synclinal orientation derives from hyperconjugative donation of the vicinal C-H σ-electron bonding electrons.[1] As the C-F bond is highly polarized, the C-F σ*-antibonding orbital is lowered in energy and can be populated by contribution from the adjacent C-H bonding electrons. The synclinal (*versus* the antiperiplanar) orientation promotes greater orbital overlap between the donor σ-bonding electrons and the accepting σ*-antibonding orbital.

Can a different mechanism operate with less electro-negative atoms having lone pairs of electrons (oxygen, nitrogen, etc.) interacting with nonadjacent C-H bonds through space? Our initial hypothesis examines the two methoxy groups at either end of a 7-carbon chain and then goes on to look at 15 other isomers of $C_9H_{20}O_2$. We ask whether synclinal orientations can lead to an attractive effect, and, if so, what is the origin of such stabilization?

METHODOLOGY

1,7-Dimethoxyheptane and its 15 branched dimethylated isomers having 5 C-C bonds between the methoxy groups were first built using molecular model kits in order to approximate the most stable conformations. Through the use of Gaussview 5.0,[5] the theoretically most stable conformations of each $C_9H_{20}O_2$ isomer were built and optimized at a low level (HF/3-21G). The structures were subsequently uploaded to the UCR WebMO website in order to use the Gaussian 09 program suite[4] to optimize molecular geometries and determine the electronic energies using Density Functional Theory (DFT at the B3LYP/6-31G** level) of each individual conformation. The electronic energies thus obtained were compared among the various conformations for a given structure to determine which is most favored (*i.e.* having the most negative electronic energy). Following geometry optimization, each conformation was examined to assess five different pairwise parameters of interest: the number of *gauche* interactions; of 1,4 synclinal carbon-oxygen interactions; of 1,5 synclinal carbon-oxygen interactions; of 1,5 carbon-carbon interactions; and O-C-C-O dihedral torsion angles. A multiple linear regression analysis was then performed (using Microsoft Excel) on the data set to determine best-fit parameters and the value of R^2. There were two multiple regression analyses performed, with and without the inclusion of the methoxy dihedral angles. The R^2 values obtained were 0.60 and 0.56 respectively.

RESULTS

Using only the four pairwise steric parameters: *gauche*; synclinal O/C; 1,5 O/C; and 1,5 C-C, the regression analysis gives only moderate fit with a correlation coefficient R^2=0.56. The linear regression assumes no other outside contributions to give the conformational energy relative to the most stable geometry for a given isomer. This equation (with variables defined in Table 1) tests the extent to which simple addition of non-neighbor, pairwise interactions can accurately predict the electronic energy of a given molecule:

Energy (in kJ/mol) = $2.13X_1 - 1.18X_2 + 1.42X_3 + 18.8X_4$ **(1)**

Table 1. *Regression analysis data for the sample set of our four initial parameters not including dihedral torsion angles.*

	R^2	0.561
	Observations	n = 45
X_1	Gauche	2.13
X_2	Syn O/C	-1.18
X_3	1,5 O/C	1.42
X_4	1,5 C-C	18.8
	Y-intercept	0

From Table 1, one can determine qualitatively whether a given interaction is stabilizing or destabilizing. As expected, *gauche* and 1,5 carbon-carbon interactions are destabilizing, while synclinal carbon-oxygen interactions are stabilizing, consistent with the inference from the lowest conformations of 1,7-dimethoxyheptane. It turns out that 1,5 carbon-oxygen interactions are destabilizing. The generally accepted value of a *gauche* is 3.5 kJ/mol, a value greater than the value from our fit. We therefore re-examined the 1,7-dimethoxyheptane to see if there were any other parameters that could be incorporated to improve the data correlation. For 1,7-dimethoxyheptane, it turns out that the two lowest energy conformations contain the same number of steric interactions. Looking at the optimized geometries for these two conformations, the only difference is the orientation of the methoxy groups relative to the plane of the methylene chain. The higher energy conformer contains a methylene chain in which the methoxy groups are on the same side of the carbon chain (*syn*) while the more stable conformation positions the methoxy groups facing on opposite sides from one another (*anti*). The difference between the two conformations is 0.22 kJ/mol. In this example, it would appear that orientation of the methoxy groups plays an important role in determining conformational stability. We set out to test whether the incorporation of O-C-C-O dihedral torsion angles would give a better correlation.

To test this second hypothesis, the dihedral angles for each conformation were tabulated and used as another variable that can influence the stability of a given conformation. There are two ways that cosines of the dihedral angles can be incorporated into the multiple regression analysis: absolute dihedral angle vs. relative dihedral angle. On the one hand,

Table 2. *Regression analysis data for the incorporation of the fifth parameter in addition to the previous four to test the new hypothesis.*

	R^2	0.602
	Observations	n = 44
X_1	Gauche	1.95
X_2	Syn O/C	-1.03
X_3	1,5 O/C	1.21
X_4	1,5 C-C	17.6
X_5	Torsion angle	1.2
	Y-intercept	0

if absolute dihedral angles are used in the analysis, the correlation coefficient does not change significantly. On the other hand, Table 2 shows that if the dihedral angles are tabulated as a value relative to the most stable conformation for each of the 15 isomers, there is a positive change in the correlation coefficient. In order to incorporate the dihedral angles, we can take either the $\cos(\Theta/2)$ or the $\cos^2(\Theta/2)$. This correction allows us to compare the values across the different isomers. Both functions for the absolute dihedral angles provide a poor fit, but the $\cos^2(\Theta/2)$ function for the relative dihedral angles gives the fit shown in Table 2. For this new data set, the equation used to describe the aforementioned steric effects plus the pairwise electrostatic effects can be expressed as:

$$\text{Energy (in kJ/mol)} = 1.948X_1 - 1.034X_2 + 1.212X_3 + 17.648X_4 - 1.246\cos^2(X_5/2) \qquad \textbf{(2)}$$

Note that the value for *gauche* repulsion decreases slightly relative to the value for the 4-parameter fit. In either case, the qualitative outcome remains the same. That is to say**,** *gauche*, 1,5 O/C, and 1,5 C-C interactions are all destabilizing by approximately the same numerical value as in the 4-parameter fit, while synclinal C/O interactions remain stabilizing by approximately 1 kJ/mol apiece. From these data, however, as previously noted by Houk *et al.*, the pairwise effects are not additive.[2]

DISCUSSION

Why are synclinal conformations of electronegative groups more favored relative to the antiperiplanar conformation? To make this determination, 1-propanol was analyzed**,**

where the oxygen is either synclinal or antiperiplanar to the methyl. DFT confirms the results of computational studies by Houk et al[2]: in neutral 1-propanol, the synclinal geometry is preferred by 0.47 kJ/mol (B3LYP/6-31G**). Houk et al[2] describe this result as a result of steric attraction between the electronegative oxygen and the methyl group, which acquires a slight positive charge. Our results suggest a different interpretation.

When 1-propanol is protonated on oxygen, such steric attraction ought to become repulsion, forcing the oxygen and the methyl to become antiperiplanar to alleviate steric repulsion (because the protonated alcohol and the methyl now both have positive charges). By contrast, an explanation based on hyperconjugation would predict that the synclinal preference should increase for the conjugate acid, since the σ*-energy of the CO bond decreases in the cation. Our calculations show that, as in the nonprotonated case, the synclinal conformation of $CH_3CH_2CH_2OH_2^+$ is indeed favored, with a greater preference (1.35 kJ/mol at B3LYP/6-31G**) than in the neutral alcohol. To confirm this result, calculations were done on protonated 1-propanol at a higher level (B3LYP/aug-cc-pVTZ), which yielded a similar value. Consequently, we infer that hyperconjugation leads to the preference for the synclinal conformation rather than steric attraction.

Houk et al[2] report that compounds with multiple synclinal interactions impede one another, causing stabilizing effects to cancel.[2] The implication of this result indicates that the effects of dipole-dipole and dipole-induced dipole interactions are not additive. The goal of the present effort

has been to investigate whether placing ether functionalities sufficiently far apart can render hyperconjugative and electrostatic effects additive.

In the case of 1,7-dimethoxyheptane, we find that the most stable conformation is not fully extended, but rather has both of the methoxy groups oriented synclinally on opposite sides of the fully extended hydrocarbon chain. This result is in qualitative agreement with that of both Houk et al.[2] and Wiberg and Murcko[3], although we attribute this result to hyperconjugation rather than steric attraction. The remaining 15 molecules under investigation are diether compounds where the oxygen atoms are five methylene units apart. As noted above, our objective to see if the distance between the oxygen atoms is sufficient to see additive effects.

Figure 1 shows four of the six examples of 1,5 carbon-oxygen interactions that were explored in this research. Like the molecules illustrated in Figure 1, the examples not shown contain variations which do not include any fully extended conformations. Unlike the 1,4 synclinal carbon-oxygen interactions, the interactions pictured in Figure 1 turn out to have a destabilizing effect on the conformation. Such a result is consistent with the hyperconjugative model. As distance increases, hyperconjugation can no longer play an important role in conformational stability. Linear regression shows the 1,5 carbon-oxygen interactions to be destabilizing by slightly more than 1 kJ/mol.

The last variable left to consider is 1,5 carbon-carbon interactions, which exert a large destabilizing effect, as
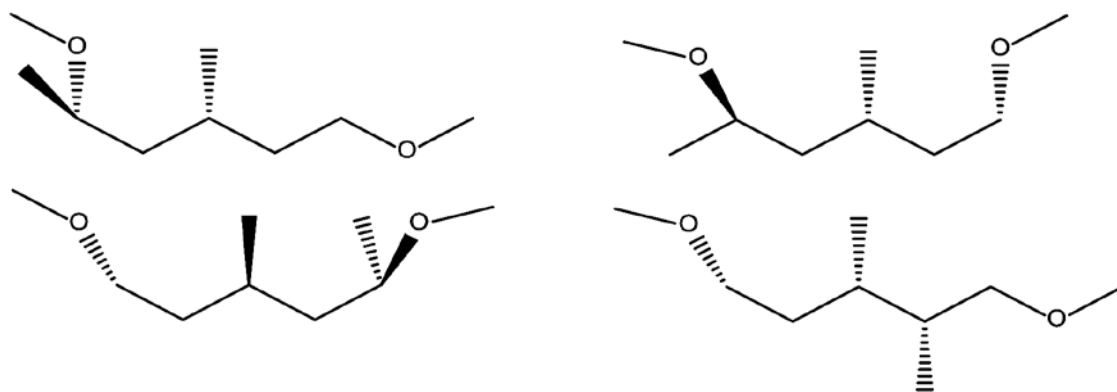
Figure 1. *Four examples showing 1,5 carbon-oxygen interactions. All of the above cases involve the methoxy oxygen interacting with the hydrogen attached to the methyl 4 atoms from itself.*

noted numerous times in the scientific literature. There is only one instance of this interaction examined during the course of this research. The conformation involving this type of interaction is shown below in Figure 2.
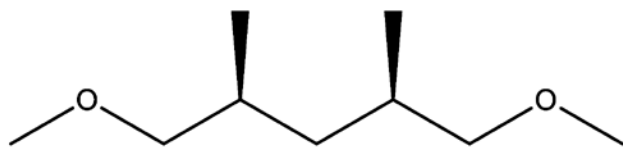
Figure 2. The lone example of a 1,5 carbon-carbon interaction

As the 4-parameter fits are far from perfect, re-examination of 1,7-dimethoxyheptane, as noted above, shows that two conformations with differing energies have the same steric effects. The orientation of the methoxy groups within space must also play an important role in the stability of a given conformation. This effect in 1,7-dimethoxyheptane has led us to formulate a more elaborate version of the initial hypothesis. We specifically wanted to see whether the inclusion of the dihedral angles for the methoxy groups would increase the correlation of the data. Using the same isomers of 1,7-dimethoxyheptane, all the dihedral angles were tabulated as differences from the most stable. (One important point to note is that 1,7-dimethoxyheptane is not included in the multiple regression data) The purpose for the exclusion is to maintain a constant distance between the two methoxy groups. All isomers included in the analysis contain five carbon atoms between them (whereas the 1,7 has 7 carbon atoms). This added distance could have other unaccounted for effects that we wished to avoid.

After inclusion of the antiperiplanar *versus* synclinally oriented methoxy groups, the correlation coefficient increases slightly. Thus, we conclude that the pairwise effects of sterics and electrostatics are still not additive.

CONCLUSIONS

Examination of the effects of steric interactions versus electrostatic effects gives two main conclusions. The first conclusion is that synclinally oriented ether functionalities better stabilize a given conformation based on a hyperconjugative model rather than the previously

proposed notion of steric attraction. The calculations done with protonated1-propanol show that the idea of steric attraction is not the major consideration for an optimized geometry, but rather the stability associated with σ-donation into antibonding orbitals from nearest neighbor interactions. Expanding this result to include non-nearest neighbor interactions does not yield the same result when the electronegative functionalities are spaced farther apart. Secondly, the incorporation of the cosines of dihedral angles does not make the pairwise effects of electrostatics and sterics additive, as evidenced by the marginal increase in the correlation coefficient upon addition of this variable. This last result is in agreement with previous research done by Houk et al.[2]

This work gives insight into the validity of alternative explanations for the conformations of organic molecules. These explanations deviate from the previously accepted explanation of steric attraction, put forth by Houk et al[2]. As of yet, there has not been a set of parameters that can fully explain the total conformational energies observed, which also accounts for all stabilizing and destabilizing interactions, thereby allowing them to be additive. This research provides a start in the direction of determining which interactions give the greatest impact on conformational energy. By adding non-pairwise parameters to equation 2, it may be possible to increase the correlation of the data and yield an additive result.

ACKNOWLEDGEMENTS

REFERENCES

[1] P. R. Rablen, R. W. Hoffmann, D. A. Hrovat, W. T. Borden, "Is Hyperconjugation Responsible for the 'gauche Effect' in 1-Fluoropropane and other 2-Substituted-1-fluoroethanes?" J. Chem. Soc., Perkin Trans. 1999, 2, 1719-1726.

[2] K. N. Houk, J. E. Eksterowicz, W. Yun-Dong, C. D. Fuglesang, D. B. Mitchell, "Conformational Preferences of the O-C-C-C Unit in Acyclic and Cyclic Systems. The Exo-Deoxoanomeric Effect and Related Phenomena" J. Am. Chem. Soc. 1993,115, 4170-4177.

[3] K. B. Wiberg, M. A. Murcko, "Rotational Barriers. 4. Dimethoxymethane. The Anomeric Effect Revisited" J. Am. Chem. Soc. 1989, 111, 4821-4828.

[4] Gaussian 09, Revision B.01, M. J. Frisch, G. W. Trucks, H. B. Schlegel, G. E. Scuseria, M. A. Robb, J. R. Cheeseman, G. Scalmani, V. Barone, B. Mennucci, G. A. Petersson, H. Nakatsuji, M. Caricato, X. Li, H. P. Hratchian, A. F. Izmaylov, J. Bloino, G. Zheng, J. L. Sonnenberg, M. Hada, M. Ehara, K. Toyota, R. Fukuda, J. Hasegawa, M. Ishida, T. Nakajima, Y. Honda, O. Kitao, H. Nakai, T. Vreven, J. A. Montgomery, Jr., J. E. Peralta, F. Ogliaro, M. Bearpark, J. J. Heyd, E. Brothers, K. N. Kudin, V. N. Staroverov, T. Keith, R. Kobayashi, J. Normand, K. Raghavachari, A. Rendell, J. C. Burant, S. S. Iyengar, J. Tomasi, M. Cossi, N. Rega, J. M. Millam, M. Klene, J. E. Knox, J. B. Cross, V. Bakken, C. Adamo, J. Jaramillo, R. Gomperts, R. E. Stratmann, O. Yazyev, A. J. Austin, R. Cammi, C. Pomelli, J. W. Ochterski, R. L. Martin, K. Morokuma, V. G. Zakrzewski, G. A. Voth, P. Salvador, J. J. Dannenberg, S. Dapprich, A. D. Daniels, O. Farkas, J. B. Foresman, J. V. Ortiz, J. Cioslowski, and D. J. Fox, Gaussian, Inc., Wallingford CT, 2010.

[5] GaussView, Version 5, R. Dennington, T. Keith and J. Millam, Semichem Inc., Shawnee Mission KS, 2009.

Effects of parental condition on immune response in male California mice

Ashwin R. Sharma, Eric Kung, Juan Pablo Perea-Rodriguez, and Wendy Saltzman

Department of Biology

ABSTRACT

Trade-offs between physiological processes are an important component of life-history theory. Many studies have demonstrated trade-offs in females with regard to the costs of reproduction. Males may also make a large investment in paternal care. Though only 5 to 10% of mammalian species are known to be biparental, studies of those species in which males do invest in parental care suggest that large costs may be present. We tested the hypothesis that fathers have a dampened immune response, as compared to non-fathers, in the biparental California mouse (*Peromyscus californicus*). Three groups of male mice (fathers, housed with a female and their first litter of pups; nonbreeding males, housed with a tubally ligated female; and virgin males, housed with another male) underwent an inflammatory response caused by lipopolysaccharide injection (n=7-8 per housing condition); saline-injected males within each housing condition served as controls (n=7-10). LPS-treated males in all three housing conditions showed significant decreases in consumption of sweetened water, body temperature, and activity levels as compared to controls (P's < 0.05). Fathers consumed significantly more sweetened water (P < 0.05) than virgin males prior to treatment. After treatment, LPS-injected fathers tended to have lower body temperatures and had significantly lower activity levels (P < 0.05) when compared to LPS-treated virgin males. Contrary to our hypothesis, these results suggest that fathers have a more pronounced immune response as compared to non-fathers.

Keywords: immune response; lipopolysaccharide; trade-off; life-history theory; paternal care; *Peromyscus*

FACULTY MENTOR

Wendy Saltzman

Department of Biology

Professor Saltzman's research focuses on the behavioral neuroendocrinology of mammalian parenting. Currently her lab investigates the neural, hormonal, and sensory mechanisms that contribute to the expression of paternal behavior, as well as possible effects of parenthood on stress responsiveness, anxiety, and physiology in fathers.

Ashwin Sharma

INTRODUCTION

Trade-offs refer to situations in which a positive change in one system has an unfavorable effect in a different one (Stearns, 1989). The trade-offs between physiological processes are an important component of life-history theory. Proper allocation of energy and other resources is necessary to manage the components of life-history such as reproduction, growth, and development (Speakman, 2000, 2008). The pleiotropic effects of hormones have been observed to be crucial mediators of trade-offs between reproduction and other life-history traits (Harshman & Zera, 2007).

Many studies have demonstrated trade-offs in females with regard to the energetic costs of reproduction. Studies of placental mammals have revealed an increased average resting metabolic rate during gestation and lactation (Thompson & Nicoll, 1986). In addition, the hormones that mediate reproduction can simultaneously influence other physiological systems. For example, prolactin, which promotes lactation, also influences immune responses. Prolactin can reverse components of immunosuppression and promote survival in mice experiencing severe responses to bacteria and other pathogens (Yu-Lee, 2002; Zellweger et al., 1996). Conversely, estrogen has been found to induce thymus (an organ of the immune system) atrophy; and during pregnancy, when estrogen and progesterone levels are high, thymic involution is accelerated (Olsen & Kovacs, 1996). Importantly, immune responses may have a substantial cost through increased energetic demands and behavioral changes (Lochmiller & Deerenberg, 1999; Martin et al., 2008).

In addition to females, males may also make a large investment in caring for their young. Though only 5 to 10% of mammalian species are known to be biparental, studies of these species suggest that paternal care may have significant costs (Clutton-Brock et. al., 1981; Woodroffe & Vincent, 1994). Hormones that change with fatherhood are known to also affect immune responses. In California mice (*Peromyscus californicus*), prolactin levels in fathers are significantly higher than those in expectant fathers and isolated virgin males (Gubernick & Nelson, 1989), which could potentially affect immune function as discussed

above. Furthermore, testosterone (T) has been reported to maintain paternal behavior in California mice (Trainor & Marler, 2001) and to have an immunosuppressive effect in other rodent species (Klein, 2000; Martin, 2008). In the biparental prairie vole (*Microtus ochrogaster*), fathers show decreases in body weight and in circulating leptin concentrations over time (Campbell et al., 2009). Leptin is involved in metabolic resource allocation by influencing appetite, metabolism, and ultimately body mass; leptin also appears to improve immune responses (Friedman & Halaas, 1998; Grunfeld et al., 1996; Lord et al., 1998). Therefore, paternal care may entail trade-offs with immune function in fathers (Lochmiller & Deerenberg, 2000; Martin et al., 2008; Speakman, 2008); however, virtually nothing is known about the effects of fatherhood on immune responses in mammals.

In this study, we tested the hypothesis that fathers have a suppressed immune response, as compared to non-fathers, in the biparental California mouse. Mice underwent an inflammatory infection caused by treatment with lipopolysaccharide (LPS), an endotoxin derived from the cell wall of gram-negative bacteria (Raetz & Whitfield, 2002). Behavior and body temperature following LPS treatment, as well as under baseline conditions, were compared among fathers, non-breeding males pair-housed with a female, and virgin males.

METHODS

Experimental Design – Male California mice born and housed in our breeding colony at UC Riverside were maintained as previously described (Harris et al., 2011). Fifty adult males were randomly assigned to three groups prior to isolation: **new fathers** (NF; n=16) that were housed with a mate and, eventually, their first litter of pups; **non-breeding males** (NBM; n=18) that were paired for the first time with a tubally ligated female and therefore could not produce a litter despite mating; and **virgin males** (VM; n=16) that were pair-housed with another male. Breeding males were tested when their first litter of pups was 12-14 days old; virgin and non-breeding males were tested at a comparable age and time point. On the day of testing, male mice were isolated in a clean cage at 14:15 h with food,

water, and sweetened water available *ad lib* (see below). Four hours later, males were injected intraperitoneally with either 1mg/kg lipopolysaccharide (LPS; derived from *E. coli*) dissolved in 5ml of sterile saline (n=23), or 5ml of sterile saline alone (n=27). The LPS dose was determined on the basis of pilot tests (Sharma et al., unpub. data) and a published study on California mice (Martin et al., 2008). After injection, behavioral data, as well as ingestion of food and water, were recorded for 4h. Lastly, mice were euthanized 4h post-injection (22:15 h), and body temperature was measured. Specific procedures are described below.

Behavioral Data Collection – Beginning immediately after injection, each mouse was video-recorded continuously for 4h. Recorded behavior was subsequently scored through instantaneous scans at 5-min intervals. Sickness behavior in this species is evident mostly through instances of continued lethargy and hunched posture (Martin et al., 2008).

Body Temperature – Rectal body temperature was measured 4h post-injection using a thermocouple as previously described (Harris et al., 2011). A decrease in body temperature is indicative of sickness in California mice, as this species has been shown to exhibit hypothermia after treatment with LPS (Martin et al., 2008).

Anhedonia Tests – Animals' intake of food and water was monitored to evaluate possible anorexia following injection, and their intake of sweetened water (3.2% *Sweet & Low* by weight) to evaluate possible anhedonia (i.e., failure to carry out pleasurable acts, a common symptom of acute-phase immune responses (Martin et al., 2008)). The animals' standard diet, as well as water and sweetened water, was available *ad libitum* throughout the experiment. Each type of water was presented in a 60ml syringe fitted with a bearingless nozzle to prevent dripping and allow accurate measurement of fluid intake. To monitor consumption of each substance before and after injection, we weighed each animal's food and water syringes immediately before the animal was isolated, at the time of injection, and again at the time of euthanasia. A decreased intake of each substance suggests sickness.

Statistical Analysis – Analyses were completed using R statistical software (2012; R Foundation for Statistical Computing, Vienna, Austria). Normality was tested using Shapiro-Wilk tests, and homogeneity of variance was determined through Bartlett's tests. We compared the differences within (Paired T tests) and among reproductive conditions and between pre- and post-injection values for consumed sweet water, body temperature, and activity levels between LPS-treated and saline-treated mice using 2-way ANOVAs with treatment (LPS or saline) and reproductive condition (breeders, non-breeders, or virgins) as factors. If ANOVAs were significant, Tukey HSD post-hoc tests were used.

RESULTS

Within-group Comparisons

Sweetened Water Consumption – Within each of the three reproductive conditions, consumption of sweetened water did not differ between experimental (LPS-treated) and control (saline-treated) males prior to injection. Following injection, however, LPS-treated males consumed significantly less sweetened water than their respective controls (NF: T=-3.87, df=14, P=0.0038; NBM: T=1.05, df=16, P<0.001; VM: T=-3.16, df=14, P=0.01; T-tests; Table 1).
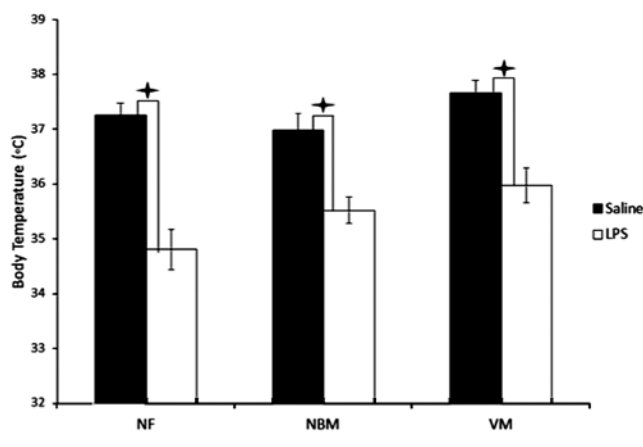
Figure 1. *Body temperature (mean ± SE) in °C for new fathers (NF), non-breeding males (NBM), and virgin males (VM) under each treatment. Symbols indicate significant differences between LPS- and saline-treated mice within conditions (P's<0.05).*

Table 1. *Body temperature, consumption of sweetened water, and activity levels in new fathers (NF), non-breeding males (NBM), and virgin males (VM) under different treatments. Activity is represented as the proportion of 5-min instantaneous scans in which the mouse was active, out of 45 scans across 4h. Within treatments, values with the same superscript are significantly different from one another.*

Reproductive Cond.	Body Temp. (∘C, mean ± SE)		Consumption of Sweetened Water (g, mean ± SE)				Activity (mean ± SE)	
	Post-Treatment		Pre-Treatment		Post-Treatment		Post-Treatment	
	Saline	LPS	Saline	LPS	Saline	LPS	Saline	LPS
NF	38.10 ± 0.20	34.81 ± 0.37	5.12 ± 1.17	4.17 ± 1.03[a]	5.82 ± 1.53	0.37 ± 0.09	0.90 ± 0.025[b,c]	0.051 ± 0.013[d]
NBM	36.99 ± 0.30	35.52 ± 0.23	2.09 ± 0.38	3.28 ± 1.05	4.65 ± 0.81	0.37 ± 0.14	0.78 ± 0.034[b]	0.063 ± 0.032[e]
VM	37.66 ± 0.22	35.98 ± 0.31	2.45 ± 1.04	1.50 ± 0.52[a]	4.86 ± 1.44	0.73 ± 0.37	0.81 ± 0.019[c]	0.25 ± 0.10[d,e]

Body Temperature – In all three reproductive conditions, experimental mice had significantly lower body temperatures 4h after injection than control mice (NF: T=-6.05, df=14, P<0.001; NBM: T=-3.23, df=13, P=0.0065; VM: T=-4.70, df=15, P=0.0028; T-tests; Table 1, Figure 1).

Activity – In all three reproductive conditions, LPS injection led to significantly lower activity levels than saline injection (NF: T=-7.65, df=7, P<0.001; NBM: T=-6.06, df=8, P<0.001; VM: T=-6.06, df=7, P<0.001; T-tests; Table 1, Fig. 2).

Between-groups Comparisons

Sweetened Water Consumption – We found a significant effect of reproductive condition on consumption of sweetened water in LPS-treated mice (F=4.88, df=2, P=0.012; ANOVA). Prior to injection with LPS, NFs consumed more sweetened water than VMs (P=0.01; Tukey HSD test; Table 1); NBMs did not differ significantly from either VMs or NFs. No significant differences among reproductive conditions were found following LPS injection.

Body Temperature – There was a significant effect of reproductive condition on body temperature (F=61.57, df=1, P<0.001; ANOVA test; Table 1, Fig. 1). Specifically, VMs tended to have higher body temperature than NFs independent of treatment (P=0.083; Tukey HSD test). LPS-treated VMs also tended to have higher body temperature than LPS-treated NFs (P=0.085; Tukey HSD test); however,

these differences were not statistically significant. Body temperature of NBMs did not differ significantly from that of either VMs or NF.

Activity – Following LPS injection, VMs were significantly more active than both NFs and NBMs (P's<0.001; Tukey HSD tests; Table 1, Fig. 2). In contrast, among saline-treated mice, we found NFs to be significantly more active than both NBMs and VMs (P's<0.001; Tukey HSD tests).
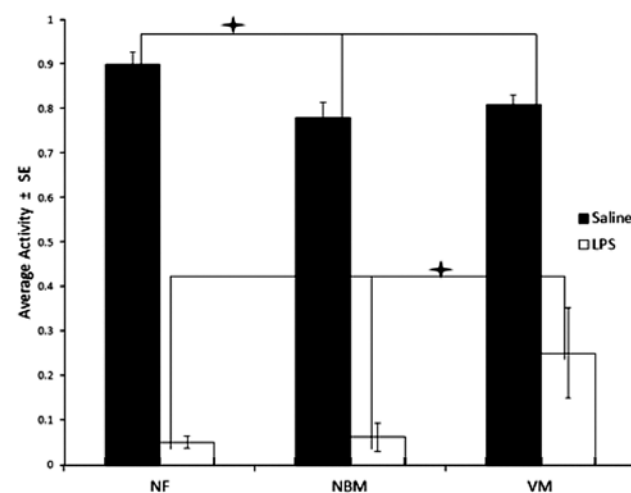
Figure 2. *Mean ± SE activity levels (proportion of 5-min instantaneous scans across 4 hours) in new fathers (NF), non-breeding males (NBM) and virgin males (VM) following saline or LPS injections. Among saline-treated mice, NFs were significantly more active than both NBM and VMs. Following treatment with LPS, VMs were significantly more active than NFs and NBMs. Symbols indicate significant differences among breeding conditions within treatments (P<0.05).*

DISCUSSION

Our data indicate that LPS treatment was successful in inducing sickness in California mice. This was seen in the significant reductions in sweetened-water consumption, body temperature, and activity levels in LPS-treated mice as compared to controls. Similar results were found in a previous study on LPS-treated California mice (Martin et al., 2008); however, our results are novel in characterizing differences in immune response associated with paternal condition. We hypothesized that fathers would have a diminished immune response compared to non-fathers, due to the hormonal changes and energetic costs associated with paternity. In contrast, our results suggest that breeding males have increased sickness behavior in terms of anhedonia, activity levels, and, to some extent, body temperature. New fathers showed a larger fall in the consumption of sweet water and significantly lower activity levels following LPS treatment, as well as a tendency toward lower body temperature, compared to virgin males.

Sickness behavior refers to behavioral changes that presumably function to combat any present diseases or localized infections; these behaviors are thought to represent an attempt to allocate energy toward recovery (Hart, 1988). Several changes associated with fatherhood might account for the observed effects of reproductive condition on sickness behavior. For example, the adipocyte hormone leptin, which has been found in prairie voles to be lower in fathers than in virgin males (Campbell et al., 2009), can influence and be influenced by proinflammatory cytokines, and can mediate energy allocation (Carlton et al., 2012), which are important to the behaviors involved in paternal care (Woodroffe & Vincent, 1994). The results of our study touch on these effects. New fathers consumed significantly more sweetened water than virgin males prior to LPS infection, which might indicate the need for higher caloric intake. Additionally, fathers were significantly less active after LPS injection, and tended to have lower body temperature, than virgin males, which may be due to more energy being allocated to the immune response.

One limitation of our study is that we collected data from LPS-treated animals only during the period immediately following treatment rather than at later time points.

In addition, we used only a single dose of LPS. More comprehensive approaches might reveal additional differences among reproductive groups.

It is difficult to determine whether the increased sickness behavior in fathers constitutes an enhanced or diminished immune response. One possibility is that the enhanced sickness behavior in fathers reflects a greater need to conserve energy, compared to non-fathers. Conversely, fathers might have a greater capacity to respond to an immune challenge through adaptive changes in behavior and physiology. It is also possible that cohabitation and the hormonal and behavioral changes associated with pair-bonding with a female may prove to have an effect, as non-breeding males housed with tubally ligated females had intermediate results. Although males in this study were isolated for 4 h prior to treatment, this acute change in housing condition is not expected to alter the physiological effects of long-term housing conditions (Campbell et al., 2009). One way to address these questions is by quantifying circulating cytokine concentrations. Cytokines are chemical messengers that are released through the activation of macrophages, mast cells, and dendritic cells, and that help mediate the inflammatory response (Owen et al., 2013). We plan to determine concentrations of cytokines in blood samples collected in this study, to further characterize possible effects of reproductive condition on the response to an immune challenge and to clarify whether these changes reflect an enhanced or suppressed immune response. Together, these studies will significantly advance our understanding of the costs, or possibly the benefits, of fatherhood in biparental mammals.

REFERENCES

Campbell, J. C., Laugero, K. D. & Van Westerhuyzen, J. A. 2009. Costs of pair-bonding and paternal care in male prairie voles (*Microtus ochrogaster*). Physiology & Behavior, 98, 367–373.

Carlton, E. D., Demas, G. E. & French, S. S. 2012. Leptin, a neuroendocrine mediator of immune responses, inflammation, and sickness behaviors. Hormones and Behavior, 62, 272–279.

Clutton-Brock, T. H., Albon, S. D. & Guiness, F. E. 1981. Parental investment in male and female offspring in polygynous mammals. Nature, 289, 487–489.

Friedman, J. M. & Halaas, J. L. 1998. Leptin and the regulation of body weight in mammals. Nature, 395, 763–770.

Grunfeld, C., Zhao, C., Fuller, J., Pollack, A., Moser, A., Friedman, J. & Feingold, K. R. 1996. Endotoxin and cytokines induce expression of leptin, the ob gene product, in hamsters a role for leptin in the anorexia of infection. Journal of Clinical Investigation, 97, 2152–2157.

Gubernick, D. J. & Nelson, R. J. 1989. Prolactin and paternal behavior in the biparental California mouse, Peromyscus californicus. Hormones and Behavior, 23, 203–210.

Harris, B. N., Perea-Rodriguez, J. P. & Saltzman, W. 2011. Acute effects of corticosterone injection on paternal behavior in California mouse (*Peromyscus californicus*) fathers. Hormones and Behavior, 60, 666–675.

Harshman, L. G. & Zera, A. J. 2007. The cost of reproduction: the devil in the details. Trends in Ecology & Evolution, 22, 80–86.

Hart, B. L. 1988. Biological basis of the behavior of sick animals. Neuroscience & Biobehavioral Reviews, 12, 123-137.

Johnson, M. S., Thomson, S. C. & Speakman, J. R. 2001. Limits to sustained energy intake I. Lactation in the laboratory mouse *Mus musculus*. Journal of Experimental Biology, 204, 1925–1935.

Klein, S. L. The effects of hormones on sex differences in infection: from genes to behavior. 2000. Neuroscience and Biobehavioral Reviews, 24, 627–638.

Lochmiller, R. L. & Deerenberg, C. 2000. Trade-offs in evolutionary immunology: just what is the cost of immunity? Oikos, 88, 87–98.

Lord, G. M., Matarese, G., Howard, J. K., Baker, R. J., Bloom, S. R. & Lechler, R. I. 1998. Leptin modulates the T-cell immune response and reverses starvation-induced immunosuppression. Nature, 394, 897–901.

Martin, L. B., Weil, Z. M. & Nelson, R. J. 2008. Seasonal changes in vertebrate immune activity: mediation by physiological trade-offs. Philosophical Transactions of the Royal Society of London. Series B, Biological Sciences, 363, 321–339.

Martin, L. B., Weil, Z. M. & Nelson, R. J. 2008. Fever and sickness behavior vary among congeneric rodents. Functional Ecology, 22, 68–77.

Olsen, N. J. & Kovacs, W. J. 1996. Gonadal Steroids and Immunity. Endocrine Reviews, 17, 369–384.

Owen, J. A., Punt, J. & Stranford, S. A. 2013. Kuby Immunology. New York: WH Freeman.

Speakman, J. R. 2000. The cost of living: field metabolic rates of small mammals. Advances in Ecological Research, 30, 178–294.

Speakman, J. R. 2008. The physiological costs of reproduction in small mammals. Philosophical Transactions of the Royal Society of London. Series B, Biological Sciences, 363, 375–398.

Stearns, S. 1989. Trade-offs in life-history evolution. Functional Ecology, 3, 259–268.

Raetz, C. R. H. & Whitfield, C. 2002. Lipopolysaccharide endotoxins. Annual Reviews of Biochemistry, 71, 635-700.

Thompson, S. D. & Nicoll, M. E. 1986. Basal metabolic rate and energetics of reproduction in therian mammals. Nature, 321, 690–693.

Trainor, B. C. & Marler, C. 2001. Testosterone, paternal behavior, and aggression in the monogamous California mouse (*Peromyscus californicus*). Hormones and Behavior, 40, 32–42.

Woodroffe, R. & Vincent, A. 1994. Mother's little helpers: patterns of male care in mammals. Trends in Ecology & Evolution, 9, 294–297.

Yu-Lee, L.-Y. 2002. Prolactin modulation of immune and inflammatory responses. Recent Progress in Hormone Research, 57, 435–455.

Zellweger, R., Zhu, X. H., Wichmann, M. W., Ayala, A., DeMaso, C. M. & Chaudry, I. H. 1996. Prolactin administration following hemorrhagic shock improves macrophage cytokine release capacity and decreases mortality from subsequent sepsis. Journal of Immunology, 157, 5748–5754.

Effects of Gatorade and Red Bull on Voluntary Wheel Running in Genetically Selected High Runner Lines of Mice

Kristianna Wi[1], Gerald C. Claghorn[1], Layla Hiramatsu[1], Jarren C. Kay[1], Zoe Thompson[2], and Theodore Garland, Jr. [1]

[1]*Department of Biology*
[2]*Neuroscience Graduate Program*

ABSTRACT

Mice (*Mus domesticus*) from four replicate High Runner (HR) lines have been selectively bred for 20 years (69 generations) for the trait of voluntary running on wheels (1.1 m circumference). HR mice run approximately three times as many revolutions per day as do mice from four non-selected Control (C) lines, but each of the HR lines reached a selection limit more than 40 generations ago, after which running within the HR lines has not increased despite continued selection. We tested the hypothesis that Gatorade or Red Bull might cause or allow mice to run more. On days 5 and 6 of wheel access, as is used to choose breeders, HR mice ran 3.28-fold more than C ($p < 0.0001$), and females ran 1.21-fold more than males ($p = 0.0290$), with no linetype by sex interaction ($p = 0.2821$). On day 7, mice were administered fresh water, Gatorade or Red Bull. During the subsequent 19-hour period, Gatorade had no statistical effect on running, but Red Bull increased distance run by 22% in both sexes and in both HR and C lines (no interactions were statistically significant). The increase in distance caused by Red Bull was attributable to an increase in the amount of time spent running, not a change in mean (or maximum) running speed. In future studies, we plan to determine which component(s) of Red Bull are biologically active (i.e., caffeine or taurine); previous studies have found that sucrose alone does not increase wheel running.

Keywords: artificial selection, behavior, exercise physiology, experimental evolution, locomotion, sports drinks

FACULTY MENTOR

Theodore Garland

Department of Biology

Professor Garland's research program focuses on the evolution of physiological systems, as well as their phenotypic plasticity. The three main areas of research are selective breeding for high voluntary wheel running; phylogenetically based statistical methods; and ecological and evolutionary physiology of squamate locomotion.

INTRODUCTION

Red Bull and Gatorade are marketed as energy and performance enhancers. Red Bull contains a stimulant, caffeine, as well as taurine, B-group vitamins, sodium, glucose, and sucrose. Gatorade contains only sugar, sodium, and potassium. The marketing scheme for Gatorade and Red Bull targets active individuals with advertisements including images of extreme sports and sponsorships granted to popular athletes and adrenaline seekers promoting their enhanced ability to achieve these goals by use of one of these drinks. We wanted to test the claims of improved athletic performance for both of these sports drinks.

We used mice (*Mus domesticus,* original population from outbred Hsd:ICR strain) from an ongoing artificial selection experiment that breeds mice based on high voluntary wheel running (Figure 1). The mouse model consists of four replicate High Runner (HR) lines that voluntarily run up to 3-fold more revolutions per day than four non-selected Control (C) lines (Swallow et al., 1998). The difference in total wheel revolutions is caused primarily by an increase in average speed of running, rather than an increase in the amount of time spent running (Koteja et al., 1999), although male HR mice do run for significantly longer per night than male controls (Garland et al., 2011). The HR mice have been viewed as animal models of elite human athletes, exhibiting elevated endurance (Meek et al., 2009) and maximal aerobic metabolic rate during exercise (Rezende et al., 2006), whereas the Control mice are seen as representing less-athletic humans (Meek et al., 2010). HR mice voluntarily run faster in the wheels, but are not significantly better (or worse) sprinters (unpublished data), so no "trade-off" (Garland, 2014) in locomotor abilities is apparent.

Mice in the selected HR lines reached an evolutionary plateau and have remained at this plateau for about 40 generations (Figure 1, Careau et al., 2013); however, previous studies have shown they are physiologically capable of running more than their voluntary amount under some conditions (Meek et al., 2010). We hypothesized that the putative performance enhancers, Red Bull and Gatorade, would increase voluntary wheel running in both HR and C mice.
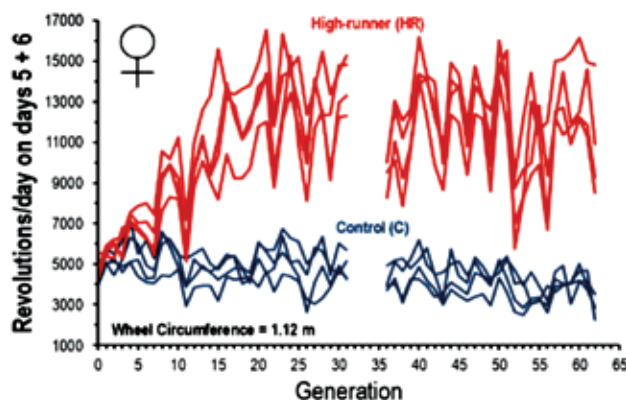
Figure 1. *Average daily wheel running of 4 replicate lines of selectively bred High Runner mice (red) as compared with 4 non-selected Control lines (blue). HR lines evolved to voluntarily run more on wheels until a plateau at approximately generations 16-20.*

Both Gatorade and Red Bull contain sugars, and additionally Red Bull contains the psychologically and/or physiologically active compounds caffeine (0.32 mg/ml), taurine (4 mg/ml), and a mixture of B vitamins (Table 1). Of the advertised ingredients, caffeine has received the most study in the exercise literature, and has been shown to increase wheel running in gerbils (Pettijohn, 1979) and to improve some measures of endurance exercise in humans (reviewed in Kalmar and Cafarelli, 2004). The primary psychomotor effect of caffeine is apparently competitive inhibition of adenosine receptors in the striatum, a region that integrates signals crucial to the execution of voluntary movements (Fisone et al., 2004). Taurine alone also has the effect of increased endurance in rats (Miyazaki et al., 2004), and combinations of the active ingredients in Red Bull have been shown to increase aerobic endurance performance in non-athlete humans (Alford et al., 2001). The psychomotor effect of taurine is also likely due to its actions on the striatum, as large doses of taurine increase extracellular dopamamine in the striatum (Salimäki et al., 2003). However, no previous study has examined the effect of Red Bull or Gatorade specifically on mammals that are genetically predisposed for high exercise abilities and high motivation to exercise, such as the HR mice.

Table 1. *Active ingredients in Red Bull and Gatorade. All units given are mg/mL.*

	Caffeine	Sugar	Taurine	Sodium	Potassium
Red Bull	0.32	110	4	0.40	0
Gatorade	-	59	-	0.45	0.13

METHODS

During the routine procedures of the artificial selection experiment, mice are given access to a 1.1 m circumference wheel for six consecutive days to acclimate to wheel use; on the fifth and sixth day, the voluntary wheel running is measured as the selection criterion for future breeders according to the amount of revolutions completed (Swallow et al., 1998). We studied mice of both sexes from generation 69. After 6 days of wheel exposure, 398 mice were randomly assigned to one of three treatments: tap water, Gatorade or Red Bull. Each water bottle was filled with 50-ml of a treatment around 12:00 hours and then administered in the early afternoon. Wheel revolutions were measured automatically in one-minute bins using photocells attached to wheels from 17:00-12:00 the following day. From the revolutions recorded every minute, total revolutions, number of active minutes (minutes with revolutions greater than 0), average speed (revolutions per active minute) and maximum speed (highest revolutions during a single minute) were calculated. Lights were off 19:00-07:00 the following day, and nocturnal *Mus domesticus* are known to be most active during the dark phase of the daily cycle (Girard et al., 2001).

Fluid consumption was measured by weighing water bottles as they were placed on cages on day 6 and when they were taken off cages on day 7 (reported as "Fluid Change Day 6-7"). The difference in mass between days 6 and 7 cannot simply be interpreted as fluid consumption because of spilling and evaporation. To test for differential spillage between different treatment types, 10 bottles per treatment were placed on empty mouse cages overnight. Any difference in these bottles between nights 6 and 7 could only be interpreted as spillage or evaporation. The average difference between drink types was subtracted from "Fluid Change Day 6-7" to adjust measured consumption values (reported as "Fluid Consumption").

We used the Mixed Procedure in SAS 9.1.3 (SAS Institute, Cary, NC, USA) to apply nested analysis of covariance (ANCOVA) to our data for wheel running. The main factors were drink type, sex, and linetype (HR vs. C), with replicate lines nested within linetype. The statistical interactions of sex by linetype, sex by drink, drink by linetype, and sex by drink by linetype were also tested, but were never statistically significant. Degrees of freedom were 1 and 6 for testing the effect of linetype. Analyses of fluid consumption were similar, but used body mass and amount of running (revolutions) as covariates. Analyses of spillage in control bottles were performed with a one-way ANOVA and post-hoc Tukey tests in JMP Pro 10 (SAS Institute, Cary, NC, USA).

Table 2. *Least squares means ± standard errors from the SAS 9.1.3 Mixed Procedure. Red Bull significantly increased voluntary wheel running in both High Runner and Control male and female mice (see text for significance levels [p values]).*

		Female		Male	
		HR	C	HR	C
Wheel Running					
	Water	14057 ± 849	3342 ± 1261	12224 ± 849	2611 ± 1163
	Gatorade	14173 ± 832	3531 ± 1093	11561 ± 824	2928 ± 1124
	Red Bull	15573 ± 839	5718 ± 1171	13849 ± 831	4131 ± 1312
Wheel-Active minutes					
	Water	542 ± 40.6	375 ± 49.2	489 ± 40.6	297 ± 46.9
	Gatorade	555 ± 40.2	399 ± 45.4	521 ± 40.3	304 ± 46.0
	Red Bull	620 ± 40.4	523 ± 47.2	578 ± 40.1	414 ± 50.3
Max Speed (RPM)					
	Water	40.4 ± 1.98	18.6 ± 2.76	38.6 ± 1.98	18.3 ± 2.56
	Gatorade	38.8 ± 1.91	18.2 ± 2.43	38.6 ± 1.94	20.6 ± 2.49
	Red Bull	39.4 ± 1.97	21.5 ± 2.59	37.8 ± 1.92	19.6 ± 2.73
Average Speed (RPM)					
	Water	26.7 ± 1.49	8.5 ± 1.87	24.7 ± 1.49	8.5 ± 1.77
	Gatorade	25.5 ± 1.47	8.6 ± 1.70	22.7 ± 1.46	9.2 ± 1.73
	Red Bull	25.3 ± 1.47	10.6 ± 1.78	24.0 ± 1.46	9.9 ± 1.85

RESULTS

On days 5 and 6 of wheel access, HR mice ran 3.28-fold more revolutions than C (p < 0.0001), and females ran 1.21-fold more revolutions than males (p = 0.0290), with no linetype by sex interaction (p = 0.2821). On the 7th day, drink type had a significant effect on total wheel revolutions (p = 0.0251, Figure 2) in both High Runner and Control lines, with no statistical interaction between drink and linetype, or drink and sex (least squares means presented in Table 2). The effects of drink type were through increases in the amount of time spent running (p = 0.0002), with no statistically significant effect on the average speed of wheel running (p > 0.05) or the maximum running speed (highest 1-minute interval; p > 0.05). The effect of treatment type was driven by a 22% increase in wheel running between Red Bull and the other two drinks. Gatorade did not have any statistically significant effects compared with water on distance run, amount of time spent running or running speeds (p > 0.05 for all measurements).

Raw values for fluid change from day 6-7 showed a significant effect of drink type (p = 0.0001) after adjusting for body mass and running amount (Table 3). Bottles with Red Bull lost the most mass, followed by Gatorade, and then water. Loss of fluid due to spillage or evaporation acquired from test bottles was significantly different among drink types by a one-way ANOVA (p < 0.0001), and post-hoc Tukey tests revealed a significantly higher loss in Red Bull than water (p < 0.0001) and in Red Bull than Gatorade (p = 0.0002), but no significant difference between Gatorade and water (p > 0.05, values for spillage in Table 3). Adjusted fluid consumption (difference between night 6 and 7 minus average loss in control bottles) was significantly different among drink types after adjusting for body mass and running amount (p = 0.0468; Table 3,
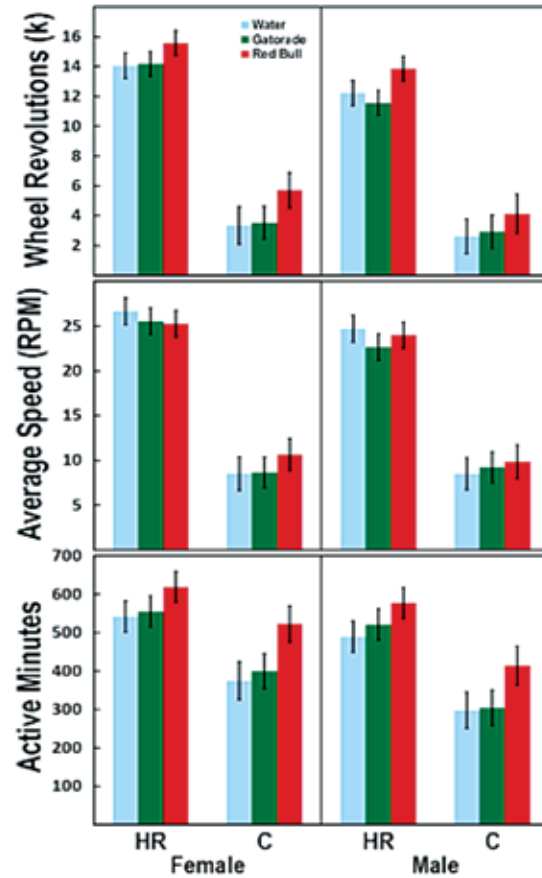
Figure 2. Red Bull significantly (p<0.05) increased voluntary wheel running in both High Runner (HR) and Control (C) lines, with no statistical interaction between drink and linetype, or drink and sex. Drink type affected total wheel revolutions by increasing the average time spent running (p=0.0002). This difference is driven by an increase in wheel running in the Red Bull group, and Gatorade did not have a statistically significant effect on voluntary wheel running Drink type did not have a statistically significant effect on the average speed of wheel running (p=0.4643). Results for maximum running speed (highest 1-minute interval) were similar to average speed.

Table 3. *Fluid consumption. Change from Day 6 to 7 and the Adjusted Fluid Consumption are least squares means ± standard errors from the SAS 9.1.3 Mixed Procedure, whereas the Control Spillage values are simple means.*

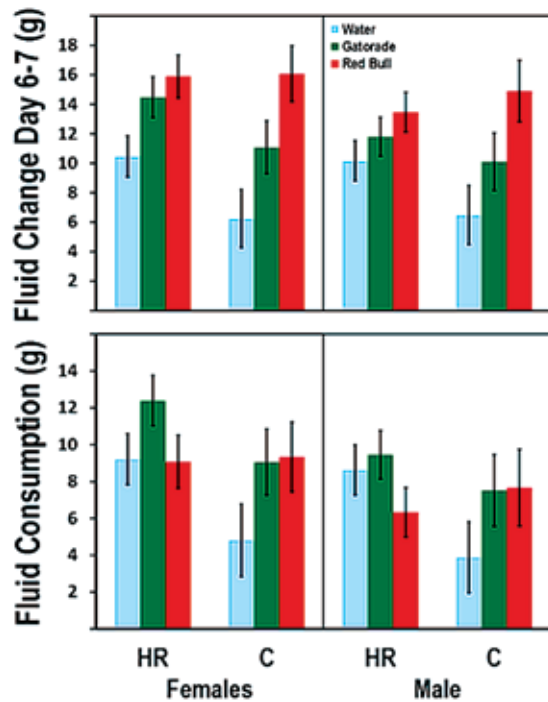|	Change Day 6-7	Control Spillage	Adjusted Fluid Consumption
Water	8.3 ± 0.96	1.4 ± 0.66	6.6 ± 0.95
Gatorade	11.9 ± 0.92	2.2 ± 0.71	9.6 ± 0.92
Red Bull	15.1 ± 0.94	7.0 ± 0.66	8.1 ± 0.94

Figure 3), and post-hoc pairwise comparisons reveal fluid consumption to be higher for Gatorade than for water (p = 0.0153, Bonferroni corrected a = 0.0167 for multiple comparisons), but no other significant pairwise differences between drinks.

Figure 3. *Upper panel*: Raw values of fluid change from day 6-7 shows a significant difference between drink types (p = 0.0001) after adjusting for body mass and running amount. Red Bull lost the most mass, followd by Gatorade, and water had the smallest fluid loss. Fluid spillage/evaporation measured from bottles on cages with no mice indicated a significant difference in fluid loss between drinks (one-way ANOVA, p < 0.0001) with a post-hoc tukey test revealing Red Bull spillage to be greater than water (p < 0.0001) and Gatorade (p = 0.0002), but no significant difference between Gatorade and water (p > 0.05). *Lower panel*: Fluid consumption was caclulated as fluid change from day 6 to day 7 minus the average spillage/evaporation for the drink type. Fluid consumption was significantly different between drink types after adjusting for (p = 0.0468), and post-hoc pairwise comparisons reveal fluid consumption to be higher for Gatorade than for water (p = 0.0153, a = 0.0167 for multiple comparisons), but no other significant pairwise differences between drinks.

DISCUSSION

Red Bull increased the voluntary wheel running (total revolutions) of both High Runner and Control mice by a similar amount (about 22%, Figure 2). The increase in total distance run was caused by a greater amount of time spent running, not an increase in running speed (p = 0.0002, p > 0.05, respectively; Figure 2). However, Gatorade did not show a statistically significant effect on voluntary wheel running in either HR or C mice, thus indicating that components of Red Bull other than carbohydrates (glucose and sucrose) are responsible for the behavioral and/ or physiological change in both HR and C lines of mice (Table 1).

From the significant increase in wheel revolutions of both HR and C mice administered Red Bull, we conclude that active ingredients in Red Bull increased the motivation or ability for voluntary wheel running. As Gatorade did not have a statistically significant effect on voluntary wheel running, we conclude that the ingredients unique to Gatorade or in common between Red Bull and Gatorade did not alter the motivation or ability for wheel running in HR or C mice.

Future experiments will lead us to break down the components of Red Bull to understand which active ingredient(s) (caffeine, taurine, and/or B-vitamin groups) is (are) responsible for the increase in voluntary wheel running and how this or these ingredient cause(s) increased wheel running. Red Bull or its components possibly affect aspects of locomotor abilities (e.g., maximum endurance); therefore, future testing of this hypothesis will include direct measurement of endurance capacity, such as in Meek et al. (2009). In addition, we hope to assess possible motivational changes in both HR and C mice (e.g., Belke and Garland, 2007).

ACKNOWLEDGEMENTS

REFERENCES

Alford, C., Cox, H. and Wescott, R. (2001). The effects of Red Bull Energy Drink on human performance and mood. *Amino Acids* 21, 139-150.

Belke, T. W. and Garland, T. (2007). A brief opportunity to run does not function as a reinforcer for mice selected for high daily wheel-running rates. *J. Exp. Anal. Behav.* 88, 199-213.

Careau, V., Wolak, M. E., Carter, P. A. and Garland, T. (2013). Limits to behavioral evolution: the quantitative genetics of a complex trait under directional selection. *Evolution* 67, 3102-3119.

Fisone, G., Borgkvist, A. and Usiello, A. (2004). Caffeine as a psychomotor stimulant: mechanism of action. *CMLS, Cell. Mol. Life Sci.* 61, 857-872.

Garland, T. (2014). Quick guide: Trade-offs. *Current Biology* 24.

Garland, T., Kelly, S. A., Malisch, J. L., Kolb, E. M., Hannon, R. M., Keeney, B. K., Van Cleave, S. L. and Middleton, K. M. (2011). How to run far: multiple solutions and sex-specific responses to selective breeding for high voluntary activity levels. *Proceedings of the Royal Society B-Biological Sciences* 278, 574-581.

Girard, I., McAleer, M. W., Rhodes, J. S. and Garland, T. (2001). Selection for high voluntary wheel-running increases speed and intermittency in house mice (Mus domesticus). *Journal of Experimental Biology* 204, 4311-4320.

Kalmar, J. M. and Cafarelli, E. (2004). Caffeine: A valuable tool to study central fatigue in humans? *Exercise and Sport Sciences Reviews* 32, 143-147.

Koteja, P., Garland, T., Sax, J. K., Swallow, J. G. and Carter, P. A. (1999). Behaviour of house mice artificially selected for high levels of voluntary wheel running. *Animal Behaviour* 58, 1307-1318.

Meek, T. H., Eisenmann, J. C. and Garland, T. (2010). Western diet increases wheel running in mice selectively bred for high voluntary wheel running. *International Journal of Obesity* 34, 960-969.

Meek, T. H., Lonquich, B. P., Hannon, R. M. and Garland, T. (2009). Endurance capacity of mice selectively bred for high voluntary wheel running. *Journal of Experimental Biology* 212, 2908-2917.

Miyazaki, T., Matsuzaki, Y., Ikegami, T., Miyakawa, S., Doy, M., Tanaka, N. and Bouscarel, B. (2004). Optimal and effective oral dose of taurine to prolong exercise performance in rat. *Amino Acids* 27, 291-298.

Pettijohn, T. F. (1979). Effects of alcohol and caffeine on wheel running activity in the Mongolian gerbil. *Pharmacology Biochemistry and Behavior* 10, 339-341.

Rezende, E. L., Kelly, S. A., Gomes, F. R., Chappell, M. A. and Garland, T. (2006). Effects of size, sex, and voluntary running speeds on costs of locomotion in lines of laboratory mice selectively bred for high wheel-running activity. *Physiol. Biochem. Zool.* 79, 83-99.

Salimäki, J., Scriba, G., Piepponen, T. P., Rautolahti, N. and Ahtee, L. (2003). The effects of systemically administered taurine and N-pivaloyltaurine on striatal extracellular dopamine and taurine in freely moving rats. *Naunyn-Schmiedeberg's Arch Pharmacol* 368, 134-141.

Swallow, J. G., Carter, P. A. and Garland, T. (1998). Artificial selection for increased wheel-running behavior in house mice. *Behavior Genetics* 28, 227-237.

Quantitative Modeling of the Alternative Pathway in Complement Immune System

Nehemiah Zewde[1], Angel Dorado[2], Ronald D. Gorham Jr.[1], and Dimitrios Morikis[1]

[1]Department of Bioengineering
[2]Department of Mechanical Engineering

ABSTRACT

The complement system is the body's first line of defense that targets invading pathogens and prompts a series of inflammatory responses which aids or "complements" antibodies to fight infections. This is accomplished by three distinct pathways known as the classical, lectin, and alternative pathway. The alternative pathway mediates up to 80 percent of all complement activation, owed to an amplification loop that rapidly generates the protein C3b in response to pathogens. We have developed a quantitative model of the alternative pathway, in order to better understand the kinetics of C3b production during infection. Our model incorporates a system of rate equations that describe the steps in the alternative pathway amplification cascade, and provides kinetic data for all proteins involved. Kinetic rate constants and plasma concentrations of complement proteins were obtained from literature, and implemented to the rate equations. Our model yields a series of time-dependent concentration data for all alternative pathway proteins, protein fragments, and protein complexes. We show that C3b is rapidly produced upon initiation of the alternative pathway amplification cascade, a fact that is supported by experimental evidence of rapid complement-mediated elimination of pathogens. Our model also demonstrates the relation between complement proteins before and during amplification steps, which aids in our understanding of the mechanisms of interaction and kinetics of complement proteins during infection. Furthermore, this model provides a framework for development of a diagnostic tool for the prediction of C3b generation and infection fighting in pathological situations that involve deficiencies or mutations in complement precursors.

Keywords: complement system, alternative pathway, mathematical modelling, rate equations, kinetic rates

FACULTY MENTOR

Dimitrios Morikis

Department of Biology

Professor Morikis' work focuses on immune system function and regulation, structure-dynamics-activity/function relations, design of peptides and proteins with tailored properties, structure-based drug discovery, and development of structural bioinformatics and *in silico* diagnostic methods. His research is predominantly computational, with emphasis on molecular dynamics simulations, electrostatic calculations, free energy calculations, pharmacophore modeling, virtual screening, and protein-ligand docking, and has an experimental component, with emphasis on binding and biochemical assays and NMR spectroscopy.

AUTHOR

Nehemiah Zewde

Department of Biology

Nehemiah Zewde is a senior in Bioengineering. He joined the Biomolecular Modeling and Design Lab, led by Professor Dimitrios Morikis, in his sophomore year. His research is focused on modelling the quantitative interactions of the complement system to better understand the dynamics involved in the body's defense mechanism. He has worked closely with Dr. Ronald Gorham Jr., a post-doctoral fellow in Morikis's lab, on several projects focused on comprehensive modelling of different complement pathways. Thanks to the support and guidance of Professor Dimitrios Morikis, Nehemiah plans to pursue a PhD in bioengineering.

Nehemiah Zewde

INTRODUCTION

The complement system is part of the body's immune system that plays a major role in the fight against pathogens. It is made up of a large number of distinct plasma proteins that react with one another to induce a series of inflammatory responses, lysis, and opsonization. The system is able to achieve this by three distinct pathways known as the classical, lectin, and alternative pathway. Classical pathway is mainly activated by C1q reacting with antibodies bound to antigen [1,2] and also by other agents, such as C-reactive protein (CRP) [3,4]. This will lead to the production of C4b and C2a, which together form the C3 cleaving enzyme of the classical pathway, called C3 convertase, resulting in C3 cleavage and formation of C3a and C3b. C3b leads opsonization and recognition for phagocytosis while C3a initiates a local inflammatory response. The lectin pathway is mainly activated by mannose-binding lectin (MBL) interacting with carbohydrate structures on microbial surfaces and by ficolins with different carbohydrate binding specificity [5]. This pathway is homologous to the classical pathway since the lectin pathway initiates complement cascade using a protein similar to C1q. The lectin pathway also forms the C3 convertase by the interaction between C4b and C2a. Finally, the alternative pathway activation starts in the fluid phase by the spontaneous and continuous turnover of fluid-phase C3. This can be seen in Figure 1 in which hydrophobic C3 is converted into a hydrophilic $C3(H_2O)$ thus initiating the alternative pathway. The subsequent cascade of biochemical reactions will lead to a distinct C3 cleaving enzyme comprised of $C3(H_2O)$ and Bb, initiating the pre-amplification step of the alternative pathway in the fluid phase as shown in the blue color scheme of Figure 1.

C3b and Bb will later form a complex on the surface of the pathogen, commencing the alternative pathway amplification loop that results in rapid C3b production. The massive deposition of C3b by the amplification reaction leads to removal of pathogens by opsonization phagocytosis, and to the formation of additional of C3 convertase enzyme. The red color scheme in Figure 1 shows the amplification loop of the alternative pathway present on the surface of

the pathogen. The cleavage of C3 is the convergence point of all three activation pathways, and the initiation point of the common pathway, which ends with the formation of the membrane attack complex, a pore-making multi-protein assembly that lyses pathogen surfaces. The amplification cascade is down-regulated on host cells by complement proteins that tightly regulate complement activation to avoid immune attacks against own tissues. In cases of impaired complement regulation, excessive complement activation can harm host cells and tissues, resulting to autoimmune and inflammatory diseases.

Our quantitative model of the alternative pathway is an indispensable tool in understanding the kinetics of C3b production during infection. Emphasis was placed on the amplification loop of the alternative pathway since the loop mediates up to 80 percent of all complement activation that rapidly generates C3b in response to pathogens. However, modelling of the complement system is not a new occurrence. Mathematical models have been presented by placing focus on the terminal step of the alternative pathway or the other two pathways (classical and lectin) [6]. Our model is the first of its kind to solely place emphasis on the amplification loop of the alternative pathway during the mass production of C3b on the surface of the pathogen.

METHODS

Our model incorporates governing equations that can be used to demonstrate the relation between complement proteins before and during amplification steps, which aids in our understanding of the kinetics of complement proteins during infection. Our mathematical model mirrors the biochemical reactions of the alternative pathway presented in Figure 1. The nomenclature used for the complement proteins involved in the alternative pathway is presented in Table 1. The interactions of the complement proteins and their rate constants involved in alternative pathway are listed in Table 2. First–order non-linear differential equations were used to represent the model, shown in Table 3. The equations denote mass balances for a single protein complex involved in the biochemical reactions of the alternative pathway. Furthermore, the resulting differential equation model consists of 14 reactions and 14 kinetic parameters
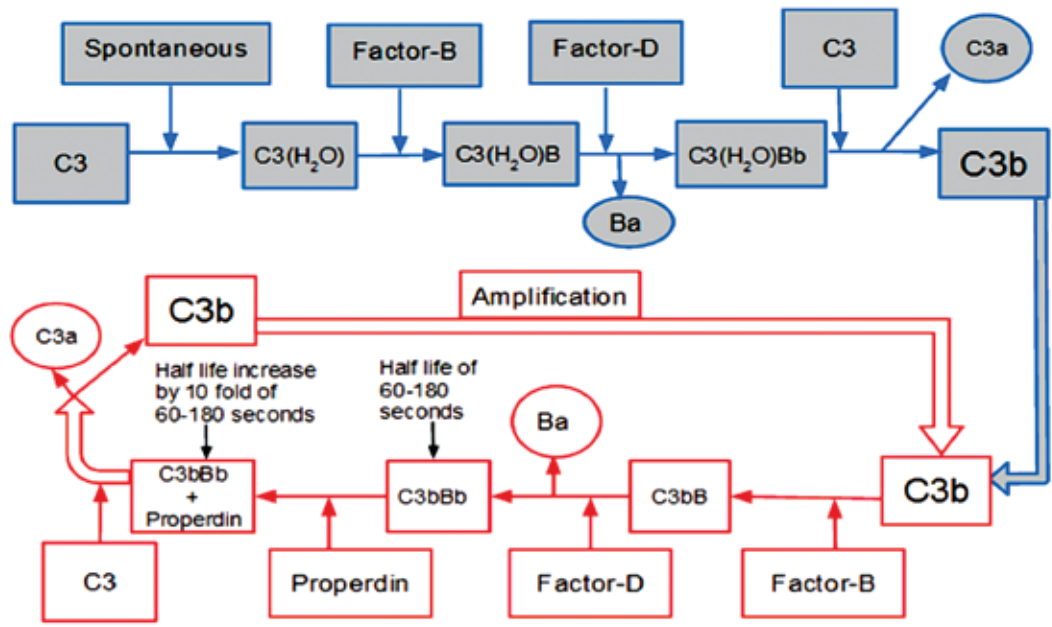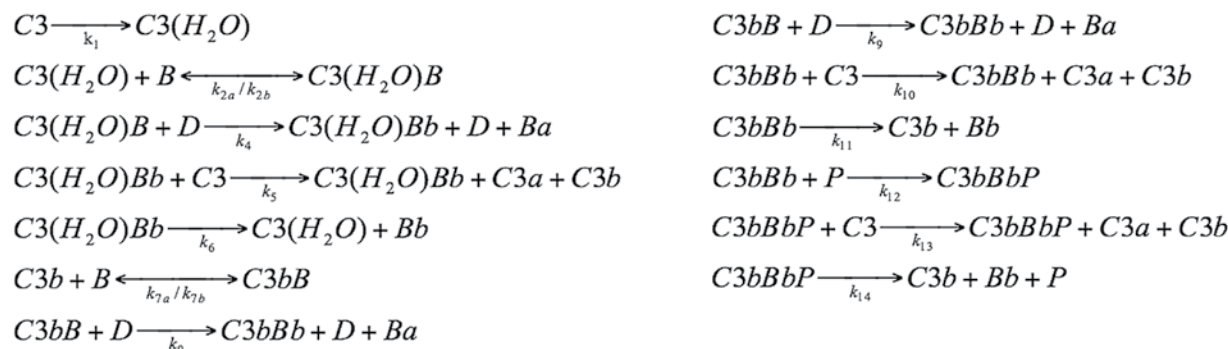
Figure 1. *Complement protein interactions of the alternative pathway. The pathway is initiated by the spontaneous turnover of C3, resulting in C3b deposition on pathogen surfaces. This leads to a set of reactions that will amplify C3b on the surface of the pathogen. The blue color scheme represents the pre-amplification step of the alternative pathway in the fluid phase. The red color scheme shows the amplification loop of the alternative pathway present on the surface*

with 4 unknowns. The concentrations for C3, properdin, Factor-D, Factor-B, and enzymatic rate constants were taken directly from the literature and are shown in Tables 4 and 5. However, mathematical estimations were implemented for the 4 unknown kinetic rate constants. In Table 5, estimations were made based on structural and functional homology. For instance, the kinetic rate constants for $C3(H_2O)$ association to Factor-B was estimated to be equal to the kinetic rate constants for C3b association to Factor-B. This is because the spontaneous tick-over of C3 generates $C3(H_2O)$ molecules which is considered to have C3b-like structure and function. Rate constants were also mathematically calculated based on the physiologically observed ranges of experimental kinetic values (k_{on} and k_{off}) from literature. Once all the concentration and kinetic rate constants were acquired, they were implemented into the differential equations. Matlab (MathWorks Inc., Natick, Mass., USA) was then used to solve our model equations for the alternative pathway, using the ode23tb ordinary differential equation solver. The results were then plotted as presented in Figures 2 and 3.

***Table 1.** Complement nomenclature.*

Abbreviations	Proteins
C3	Complement Component 3
$C3(H_2O)$	The thioster-hydrolized form of Complement Component 3
B	Factor-B
D	Factor-D
Ba	Factor-B noncatalytic chain
Bb	Factor-B catalytic subunit
C3b	Complement Component 3b
C3a	Complement Component 3a
$C3(H_2O)Bb$ C3bBb C3bBbP	Complement C3 Convertase

Table 2. *List of reactions in the alternative pathway.*

$$C3 \xrightarrow{k_1} C3(H_2O)$$

$$C3(H_2O) + B \underset{k_{2a}/k_{2b}}{\longleftrightarrow} C3(H_2O)B$$

$$C3(H_2O)B + D \xrightarrow{k_4} C3(H_2O)Bb + D + Ba$$

$$C3(H_2O)Bb + C3 \xrightarrow{k_5} C3(H_2O)Bb + C3a + C3b$$

$$C3(H_2O)Bb \xrightarrow{k_6} C3(H_2O) + Bb$$

$$C3b + B \underset{k_{7a}/k_{7b}}{\longleftrightarrow} C3bB$$

$$C3bB + D \xrightarrow{k_9} C3bBb + D + Ba$$

$$C3bB + D \xrightarrow{k_9} C3bBb + D + Ba$$

$$C3bBb + C3 \xrightarrow{k_{10}} C3bBb + C3a + C3b$$

$$C3bBb \xrightarrow{k_{11}} C3b + Bb$$

$$C3bBb + P \xrightarrow{k_{12}} C3bBbP$$

$$C3bBbP + C3 \xrightarrow{k_{13}} C3bBbP + C3a + C3b$$

$$C3bBbP \xrightarrow{k_{14}} C3b + Bb + P$$

Table 3. *Rate equations of alternative pathway divided into reactants, intermediates, and products.*

Rate Equations (Reactants):

1. $$\frac{d[C3]}{dt} = -k_1[C3] - k_5[C3(H_2O) - Bb][C3] - k_{10}[C3b - Bb][C3] - k_{13}[C3b - Bb - P][C3]$$

2. $$\frac{d[Factor - B]}{dt} = -k_{2a}[C3(H_2O)][B] - k_{7a}[C3b][B]$$

3. $$\frac{d[Factor - D]}{dt} = 0$$

4. $$\frac{d[P]}{dt} = -k_{12}[C3b - Bb][P] + k_{14}[C3b - Bb - P]$$

Rate Equations (Intermediates):

5. $$\frac{d[C3(H_2O) - B]}{dt} = -k_{3b}[C3(H_2O) - B] - k_4[C3(H_2O) - B][D]$$

6. $$\frac{d[C3(H_2O) - Bb]}{dt} = k_4[C3(H_2O) - B][D] - k_6[C3(H_2O) - Bb]$$

7. $$\frac{d[C3b - B]}{dt} = -k_{8b}[C3b - B] - k_9[C3b - B][D]$$

8. $$\frac{d[C3b - Bb]}{dt} = k_9[C3b - B][D] - k_{11}[C3b - Bb] - k_{12}[C3b - Bb][P]$$

9. $$\frac{d[C3b - Bb - P]}{dt} = k_{12}[C3b - Bb][P] - k_{14}[C3b - Bb - P]$$

Rate Equations (Intermediates):

10. $$\frac{d[C3(H_2O)]}{dt} = k_1[C3] - k_{2a}[C3(H_2O)][B] + k_6[C3(H_2O) - Bb]$$

11. $$\frac{d[C3a]}{dt} = k_5[C3(H_2O) - Bb][C3] + k_{10}[C3b - Bb][C3] + k_{13}[C3b - Bb - P][C3]$$

12. $$\frac{d[C3b]}{dt} = -k_{7a}[C3b][B] + k_5[C3(H_2O) - Bb][C3] + k_{10}[C3b - Bb][C3] + k_{13}[C3b - Bb - P][C3]$$

13. $$\frac{d[Ba]}{dt} = k_4[C3(H_2O) - B][D] + k_9[C3b - B][D]$$

14. $$\frac{d[Bb]}{dt} = k_6[C3(H_2O) - Bb] + k_{11}[C3b - Bb] + k_{14}[C3b - Bb - P]$$

Table 4. *Concentrations and molecular masses for complement proteins in plasma.*

Complement	Molecular Mass (kDa)	Plasma Concentration (μM)	Sources	Concentrations used in model (μM)
C3	185	5.3 - 8.6	[6],[7]	5.3
Properdin	53	0.38 - 0.47	[6],[7]	0.47
Factor-B	93	2.1 - 2.2	[6],[7]	2.2
Factor-D	24	0.08	[6],[7]	0.08

Table 5. *Kinetic associations and dissociations rate constants, and enzymatic cleavage rate constants for the alternative pathway. Estimations were made for unknown kinetic rate constants.*

Complement Species	Kinetic Constant	Kinetic Value	Sources
Hydrolysis of C3	k_1	8.33×10^{-7} s^{-1}	[8]
C3(H$_2$O) association to Factor-B	k_{2a}	2.13×105 M^{-1}s^{-1}	Estimation[a]
C3(H$_2$O) dissociation from Factor-B	k_{2b}	1.55×10^{-1}s^{-1}	Estimation[a]
Factor-D cleavage of C3(H$_2$O)-B	k_4	2.00×10^6 M^{-1}s^{-1}	[9]
C3(H$_2$O)-Bb cleavage of C3	k_5	1.60×10^5 M^{-1}s^{-1}	[10]
C3(H$_2$O) dissociation from Bb	k_6	9.00×10^{-3} s^{-1}	[10]
C3b association to Factor-B	k_{7a}	2.13×10^5 M^{-1} s^{-1}	[11]
C3b dissociation from Factor-B	k_{7b}	1.55×10^{-1} s^{-1}	[10]
Factor-D cleavage of C3b-B	k_9	1.00×10^6 M^{-1}s^{-1}	Estimation[a]
C3b-Bb cleavage of C3	k_{10}	3.11×10^5 M-1s^{-1}	[10]
C3b dissociation from Bb	k_{11}	7.70×10^{-3} s^{-1}	[10]
P association to C3b-Bb	k_{12}	1.0×10^6 M^{-1}s^{-1}	Estimation[a]
C3b-Bb-P cleavage of C3	k_{13}	3.10×10^5 M^{-1}s^{-1}	[10]
C3b-Bb-P dissociation	k_{14}	7.70×10^{-4} s^{-1}	[12]

[a]Rate constants estimated based on structurally homologous molecules
[b]Mathematical estimation

RESULTS AND DISCUSSION

Our model incorporates a set of rate equations that describe the biochemical reactions shown in Tables 2 and 3. Our results for the alternative pathway are summarized in Figure 2. Figures 2A and 2B show the response of the system at different time intervals of 300 and 3000 seconds. The pathway starts with the spontaneous C3 turnover, resulting in a slow gradual decrease in C3 concentration. This was expected since the spontaneous rate conversion is 0.005% per minute [8]. However, as stated in literature, the C3 concentration will substantially decrease when the C3b-Bb and C3b-Bb-P cleaving enzymes are formed. In Figure 2A, the C3 concentration rapidly decreases after 50 seconds. However, right after 50 seconds is also when the C3 cleaving enzymes begin to form. The production of two rather than one cleaving enzymes also contributes to the rapid consumptions of C3. The cleavage will result in the production of C3a and C3b. The concentration of C3a increases rapidly as more enzymes of C3b-Bb and C3b-Bb-P are formed. The production of C3a is important since it is potent mediator of inflammation. Even though C3a

Nehemiah Zewde

production rapidly reaches it maximum after 100 seconds, C3b production does not reach maximum until 3000 seconds. In Figures 3A and 3B, both complement proteins increase at the same rate, however C3b decreases slightly after 110 seconds. The massive production of C3b comes from the amplification cascade generated by the same C3 cleaving enzymes: C3b-Bb and C3b-Bb-P. Since C3b-Bb has a shorter half-life than C3b-Bb-P, it will dissociate faster. In Figure 3C, C3b-Bb and C3b-Bb-P are produced at the same time but C3b-Bb starts to dissociate at little after 150 seconds. However, C3b-Bb-P reaches its maximum and shows no sign of dissociation within the same time frame. In Figure 3D, we can see this complex is so stable, even at 3000 seconds it has not fully dissociated. Importantly, C3b increases more slowly than C3a, since it reacts with other complement proteins such as Factor-B, Factor-D, and

properdin. This will reduce the concentration of free C3b. The interaction of C3b with other complement proteins will lead to the production of more C3 cleaving enzymes: C3b-Bb and C3b-Bb-P. However, as more C3 cleaving enzymes assemble, the rate at which C3b is produced also increases. This can be seen in Figures 3A and 3B where the C3b production increases after 150 seconds, but reaches its maximum concentration at 3000 seconds.

After modelling the alternative pathway, we decided to compare the results generated from our model to experimental data from literature. For the comparison, we choose the two C3 cleaving enzymes, C3b-Bb and C3b-Bb-P. It has been shown that C3b-Bb is naturally labile and dissociates with a half-life of ~60-180 seconds [12,13]. In Figure 3C, the results from our model show that this complex dissociates with a
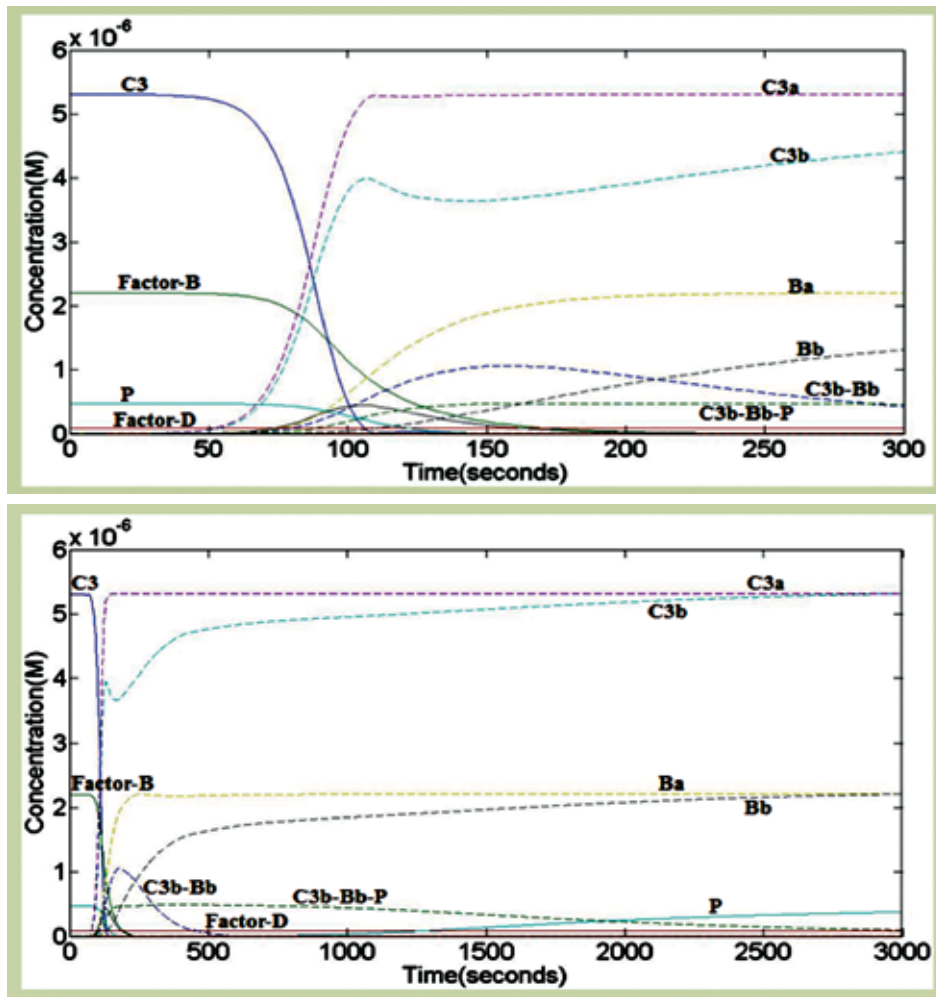

Figure 2. The Panels A and B show an overview of the response of alternative pathway proteins at different time scales of 300 and 3000 seconds.

half-life of ~110 seconds, which is within the experimental range from literature. Furthermore, the interaction between C3b and Bb is stabilized the complement protein properdin. This will increase the half-life of C3b-Bb-P by 10-fold [12]. The results generated in Figure 3D shows C3b-Bb-P has a half-life of 1300 seconds, which also coincides with experimentally determined half-life for C3b-Bb-P. This shows our model has the capability to accurately predict the response of complement proteins under physiological conditions.

The mathematical model we generated will be an indispensable tool for understanding the dynamics of the complement system. In addition, by taking advantage of the wealth of knowledge generated here from the mathematical modelling of the alternative pathway, we aim to develop a comprehensive model by incorporating the classical, lectin, and common pathways, as well as negative feedback by the regulators of complement activation. Furthermore, the augmented mathematical model will make it possible to study the effects of complement factor deficiencies, which will yield an enhanced pattern of time-dependent intermediate and terminal complement product formation. This information can be useful in diagnosis and treatment of complement-mediated diseases.
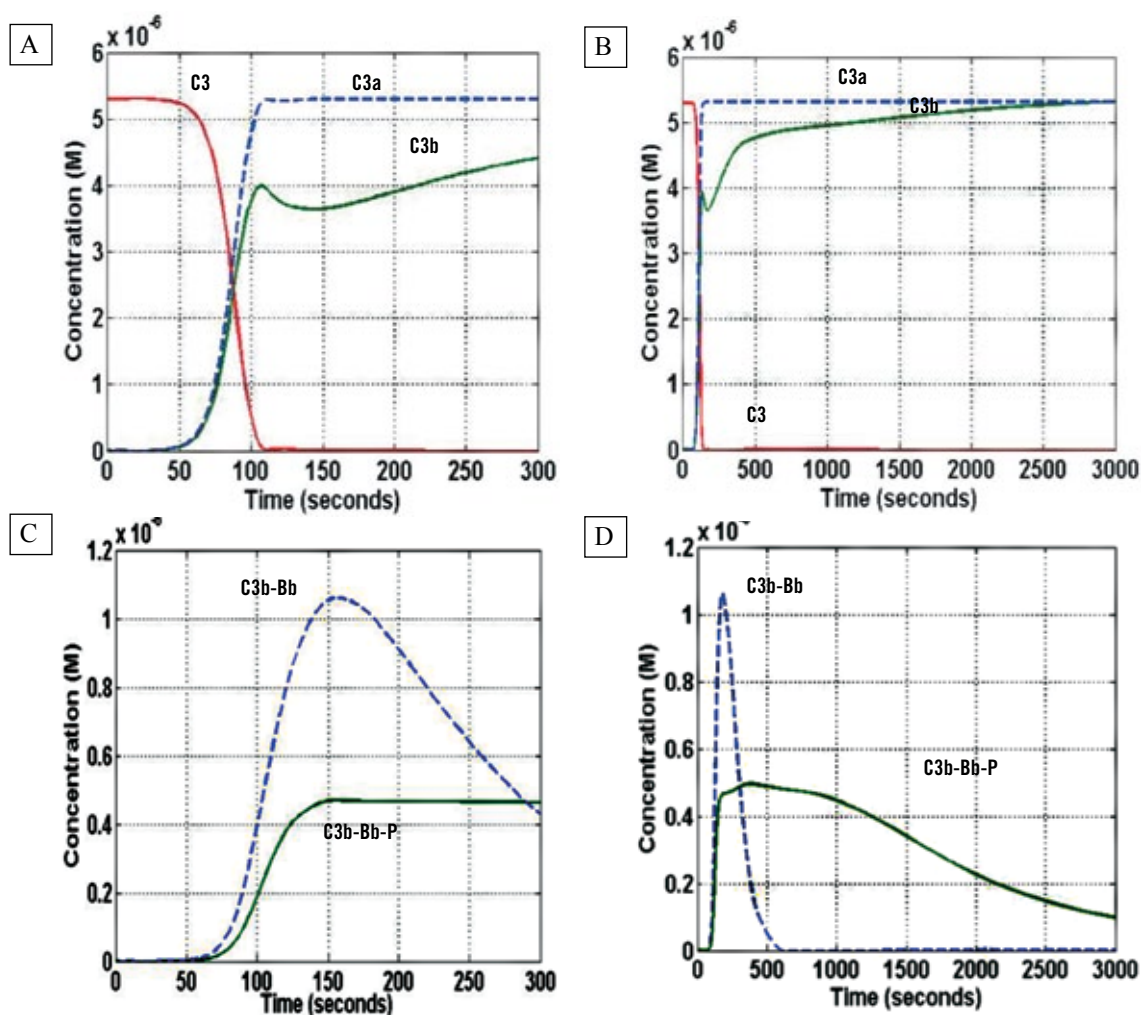
Figure 3. *Panels A and B show the reactant, C3 and the two key products of the amplification cascade, C3a and C3b. C3a reaches maximum production within the first 100 seconds while C3b reaches its maximum in 3000 seconds. This is due to free C3b binding to other complement proteins such as Factor-B and Factor-D. The C3 cleaving enzymes, C3b-Bb and C3b-Bb-P, have different half-lives. The latter enzyme has a longer half-life than the first one. Their relationship is shown in Panels C and D.*

REFERENCES

[1] M. J. Walport, "Complement. First of two parts," *N. Engl. J. Med.*, vol. 344, no. 14, pp. 1058–1066, Apr. 2001.

[2] T. E. Mollnes, W.-C. Song, and J. D. Lambris, "Complement in inflammatory tissue damage and disease," *Trends Immunol.*, vol. 23, no. 2, pp. 61–64, Feb. 2002.

[3] J. E. Volanakis and M. H. Kaplan, "Interaction of C-reactive protein complexes with the complement system. II. Consumption of guinea pig complement by CRP complexes: requirement for human C1q," *J. Immunol.* vol. 113, no. 1, pp. 9–17, Jul. 1974.

[4] A. Bíró, Z. Rovó, D. Papp, L. Cervenak, L. Varga, G. Füst, N. M. Thielens, G. J. Arlaud, and Z. Prohászka, "Studies on the interactions between C-reactive protein and complement proteins," *Immunology*, vol. 121, no. 1, pp. 40–50, May 2007.

[5] M. Harboe and T. E. Mollnes, "The alternative complement pathway revisited," *J. Cell. Mol. Med.*, vol. 12, no. 4, pp. 1074–1084, Aug. 2008.

[6] A. A. Korotaevskiy, L. G. Hanin, and M. A. Khanin, "Non-linear dynamics of the complement system activation," *Math. Biosci.*, vol. 222, no. 2, pp. 127–143, Dec. 2009.

[7] P. F. Zipfel, "Complement: Alternative Pathway," in *Encyclopedia of Life Sciences*, John Wiley & Sons, Ltd, Ed. Chichester: John Wiley & Sons, Ltd, 2001.

[8] M. K. Pangburn and H. J. Müller-Eberhard, "The C3 convertase of the alternative pathway of human complement. Enzymic properties of the bimolecular proteinase," *Biochem. J.*, vol. 235, no. 3, pp. 723–730, May 1986.

[9] G. T. Le, G. Abbenante, and D. P. Fairlie, "Profiling the Enzymatic Properties and Inhibition of Human Complement Factor B," *J. Biol. Chem.*, vol. 282, no. 48, pp. 34809–34816, Sep. 2007.

[10] M. K. Pangburn, "Formation of the initial C3 convertase of the alternative complement pathway. Acquisition of C3b-like activities by spontaneous hydrolysis of the putative thioester in native C3," *J. Exp. Med.*, vol. 154, no. 3, pp. 856–867, Sep. 1981.

[11] H. Chen, D. Ricklin, M. Hammel, B. L. Garcia, W. J. McWhorter, G. Sfyroera, Y.-Q. Wu, A. Tzekou, S. Li, B. V. Geisbrecht, V. L. Woods, and J. D. Lambris, "Allosteric inhibition of complement function by a staphylococcal immune evasion protein," *Proc. Natl. Acad. Sci.*, vol. 107, no. 41, pp. 17621–17626, Oct. 2010.

[12] D. E. Hourcade, "The Role of Properdin in the Assembly of the Alternative Pathway C3 Convertases of Complement," *J. Biol. Chem.*, vol. 281, no. 4, pp. 2128–2132, Nov. 2005.

[13] S. H. M. Rooijakkers, J. Wu, M. Ruyken, R. van Domselaar, K. L. Planken, A. Tzekou, D. Ricklin, J. D. Lambris, B. J. C. Janssen, J. A. G. van Strijp, and P. Gros, "Structural and functional implications of the alternative complement pathway C3 convertase stabilized by a staphylococcal inhibitor," *Nat. Immunol.*, vol. 10, no. 7, pp. 721–727, Jul. 2009.

Survival of Bacteria in Bamboo Tobacco Pipe Water

Vivek S. Patel, Katie E. Curnyn, and Marylynn V. Yates

Department of Biology

ABSTRACT

Nearly two million deaths annually worldwide are due to respiratory infections caused by *Mycobacterium tuberculosis* (TB). Regions in which TB is endemic include Laos, Cambodia, and Vietnam. Tobacco, and other drug use, has been found to increase the probability of contracting TB by 100- to 1,000,000-fold. Communal smoking of tobacco through bamboo water pipes remains a tradition of tribes indigenous to Laos and other Asian countries. Testing of water samples from Laotian pipes found contamination by coliform bacteria at concentrations up to 7.00×10^4 cfu/ml. The purpose of this study was to investigate the potential for microorganisms in bamboo tobacco pipe water to pose a risk to human health. *Escherichia coli*, an indicator bacterium, was added to buffer at concentrations of approximately 10^4 cfu/ml, and incubated with the bamboo tobacco pipe. Subsamples were withdrawn and analyzed daily using the EPA membrane filtration method. The bacterium grew in the presence of the bamboo pipe, reaching concentrations up to three orders of magnitude higher than those in the buffer without the pipe material. These data suggest that there may be a risk of acquiring a microbial infection to users of tobacco water pipes. More studies, using disease-causing microorganisms, are needed to better define this risk. Ultimately, it is hoped that these results can be used to influence pipe use by indigenous peoples, as well as to inform the creation of guidelines for hookah lounges in the United States.

Keywords: *mycobacterium tuberculosis* (TB), bamboo, tobacco water pipe

FACULTY MENTOR

Marylynn V. Yates

Department of Environmental Sciences
Dean, College of Natural & Agricultural Sciences

Professor Yates' research interests include characterizing and predicting the fate and transport of human enteric pathogenic microorganisms in soils, water, and wastewater; development of methods for rapid, sensitive detection of infective enteric viruses in water samples; human pathogen considerations associated with wastewater reuse and biosolids application to land; and the use of indicators for predicting pathogen occurrence and behavior in the environment. She also serves as the Chair of the University of California Global Health Institute's Education Committee.

AUTHOR

Vivek Patel

Department of Biology

Vivek Patel is a sophomore working towards a bachelor degree of biology, with a focus on Microbiology. In 2013, he was awarded the USDA Higher Education Challenge Grant to work in Dr. Marylynn V. Yates' lab. Vivek presented his research on the survival of bacteria in bamboo tobacco pipe water at the UCR Symposium of Undergraduate Research on August 28, 2013. He is an active member of the Sigma Alpha Epsilon fraternity as well as Future Dental Club. Through these organizations he contributes to outreach and volunteer activities on and off campus providing him inspiration to continue research. Performing research in a field that directly affects individual's lifestyles and health motivates him as he has seen and experienced some of the hardships of third world countries such as India.

INTRODUCTION

Water pipes are commonly used in some cultures, including tribes indigenous to Laos and other Asian countries, as a means of smoking tobacco (1). Smoke is pulled through the water as the user inhales from the mouthpiece (Figure 1). The pipes are commonly shared among members of the community and therefore have the potential for the transmission of infectious diseases, either via ingestion of contaminated water, or inhalation of aerosols created during the process, is of concern (2). Properties of the pipe, specifically frequency of use and number of individuals, were not available while we know the common practice is conducted by the youngest of children to oldest tribesmen (3).

Figure 1. *Traditional Bamboo Tobacco Water Pipe image was taken from goo.gl/lW9Xgw*

A colleague at Loma Linda University, Dr. Ryan G. Sinclair, obtained and analyzed water samples from both used water tobacco pipes and source water in Laos and found them to be contaminated with 10^2-10^4 colony-forming units (cfu)/ml fecal indicator organisms. These findings provided the basis for this investigation, because published studies on microbial interactions with bamboo wood were not found, rendering this field of research unchartered.

In addition to concerns regarding the ingestion of microorganisms from the water in the bamboo tobacco pipes, the possibility of exposure through aerosolization (*i.e.,* breathing in water droplets containing disease-causing microorganisms) is also of concern (2). Dr. Sinclair demonstrated the potential for this mode of microbial transmission by conducting an experiment using a smoking simulation apparatus, in which he showed the ability of *E. coli* to become aerosolized (3). The results of this experiment suggest the potential for other microorganisms, including pathogenic microorganisms such as *Mycobacterium tuberculosis* (TB) (2) to become aerosolized.

There are numerous microorganisms that could be introduced to, and therefore transmitted by, the water in the pipes. In order to obtain preliminary information regarding the potential for microorganisms to be transmitted in this manner, common indicator bacteria, rather than pathogenic bacteria, were used (4). Numerous advantages over pathogens because they can be analyzed rapidly and inexpensively, without posing a hazard to the investigator (5). Another advantage of using indicator microorganisms is that there are literally hundreds of extremely diverse potential pathogens that could be transmitted in this manner, so it would be difficult to choose just a few representative pathogens for studies of this nature. Use of indicators allows one to gather data, relatively rapidly and inexpensively, that can then be used as the basis to design studies using pathogenic microorganisms.

Escherichia coli (*E. coli*) is a bacterium that naturally occurs in the intestines of humans and other animals, and therefore is present in fecal material. Thus, its presence in water is indicative of fecal contamination and potentially indicates increased risks of exposure to pathogenic microorganisms (such as *Salmonella*) that are transmitted by the fecal-oral route of transmission (6). The facts that *E. coli* is an enteric bacterium (*i.e.,* it is transmitted via fecally-contaminated water and food), and that it can also be aerosolized similarly to that of TB, made it a logical choice for this study. One of the advantages of using *E. coli* as an indicator bacterium is its rapid growth: it can be detected and quantified within 24 hours, whereas TB can take weeks to months to form visible colonies (7).

The primary goal of this study was to make an assessment of the potential for disease transmission through the use of a bamboo tobacco pipe for smoking. The specific objectives were to:

1) Assess the survival and growth of indicator bacteria in tobacco pipe water.

2) Determine whether different indicator bacteria exhibited different behavior in the tobacco pipe water.

Because these pipes are made of bamboo, we hypothesize that there exists the possibility that organic compounds in the pipe material may leach into the water, thereby providing nutrients for bacterial growth. Lastly, the information gained from this study may be applicable to the development of regulations for water in hookah pipes.

METHODS AND MATERIALS

Experimental Design

A water pipe that had been used extensively for smoking by people in Laos was obtained from Dr. Ryan Sinclair, a faculty member in the School of Public Health at Loma Linda University.

Escherichia coli (ref #214884) was added to a phosphate-buffered saline (PBS) at concentrations of 10^6 colony-forming units (cfu)/ml. Phosphate-buffered saline does not contain any nutrients and therefore cannot promote growth of E. coli, while its buffered pH protects the cell (8). The bottom portion of the Laotian pipe where water is contained was cut into 5-cm rings, placed into a glass beaker and autoclaved to remove any possible microbial contamination (Figure 2). Then, 200 ml of bacterial PBS solution was added and the beaker was covered with foil and stored in an incubator at 29°C in the dark for 26 days.

Figure 2. Bamboo tobacco pipe ring soaking in bacterial solution.

A beaker of the bacterial solution, but without the pipe, was used as our control (Figure 3). This allowed us to observe the behavior of the bacteria without the pipe and determine the effect of the pipe on the bacteria. Subsamples were withdrawn daily for 14 days, then every other day for the next 12 days and analyzed as described below. Preliminary studies were conducted in the same manner using a different piece of the same pipe, however, these preliminary trials were only five days in duration (9).

ANALYTICAL METHODS

E. coli was detected and quantified using the Environmental Protection Agency (EPA) method 1603 (6). Briefly, a

Figure 3. PBS bacterial solution soaking in a beaker (control).

series of 10-fold dilutions of the water samples were made to ensure that colonies in the countable range were obtained. EPA protocol states that the countable E. coli range is between 20 and 80 colonies per petri plate (3). Petri plates containing a number of bacterial colonies either higher or lower than this countable range are not in accord with such protocol and were not used. In the case of plates with colonies below the countable range, statistically there are too few colonies to rely on the data. In the cases in which the colony count is above the range, it is difficult to distinguish colonies from one another, and the availability of nutrients may limit the number of bacteria that can grow, resulting in an underestimate of the true number of bacteria. 10-fold dilutions were plated in triplicate. Samples were filtered through an S-Pak Millipore 0.45-µm membrane filter by a vacuum filtration system, then placed on Modified Thermotolerant Escherichia coli (mTEC) Agar and incubated overnight at 37°C. The agar is both selective and differential, meaning that it only permits growth of coliform bacteria and differential because E. coli colonies will be magenta in color, due to the metabolization of specific nutrients in the media by the bacteria. *E. coli* were enumerated by dividing the volume of sample plated and

Summary of important membrane filtration steps
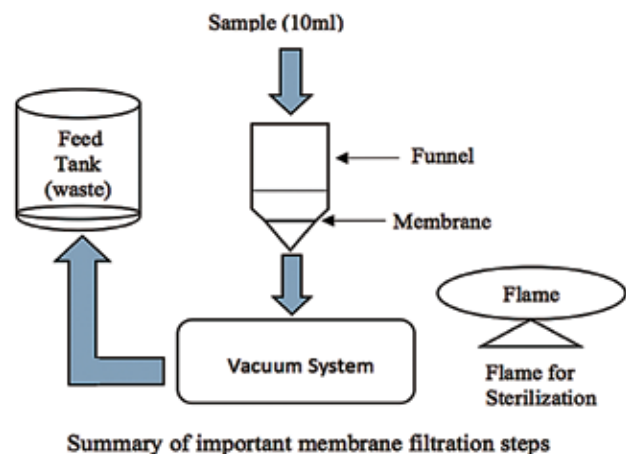
multiplied by the dilution factor. EPA method 1600 (10) was used to detect *Enterococcus faecalis* using membrane-Enterococcus Indoxyl-β-D-Glucoside Agar (mEI).

STATISTICAL ANALYSES

Data were normalized by calculating log (C_t/C_0), where C is the concentration at time $_t$, and C is the concentration at time zero. A two-sample T-test assuming unequal variance was used in this case (11). The T-test was used to determine whether there were significant differences between the log growth of bacteria in the presence of the pipe and control samples (12).

RESULTS

Escherichia coli was found to grow exponentially in the presence of the bamboo pipe material. Rapid growth of *E. coli* was observed for 13 days, at which time the concentration reached its peak at 5.90×10^{11} cfu/ml, roughly 3 orders of magnitude more than the control solution at that time (Figure 4). The difference in the concentrations was found to be significant (P <0.0001). The control solution reached its highest concentration of 2.10×10^9 cfu/ml at day 1 and then continued to decrease from day 3 through the remainder of the experiment.

Stagnation of growth was reached after 16 days of incubation with the tobacco pipe and was sustained for the remainder of the experiment. In the case of the control, the concentration of bacteria continued slowly and steadily decreased. The concentration of the bacteria in the control remained relatively constant throughout the experiment, only showing very slight initial growth in the first three days of the experiment.

DISCUSSION

These experiments demonstrate that bamboo tobacco pipes promote the growth of bacteria. The significant difference between the growth

rates of the bacteria in the presence of the pipe and without support our hypothesis that the bacteria are able to utilize nutrients from the pipe. The ability of bacteria to grow in the pipe suggests that there is a risk of contracting disease by the pipe user. This is especially of concern because, when the bamboo pipes were collected, locals informed Dr. Sinclair and colleagues that the water was not emptied out between uses of the pipe; this would tend to further promote the growth of bacteria, as nutrients would continue to leach out of the pipes over time. While our experiments were designed in a manner to mimic this situation, there are certainly differences that we were not able to include in our experiments. These include
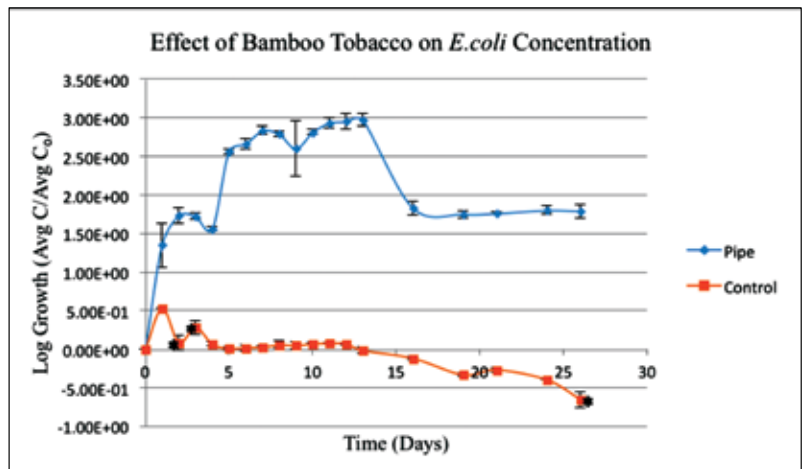

Figure 4. *Effect of bamboo tobacco pipe on* Escherichia coli *concentration. Each data point represents an average. Rapid growth of* E. coli *to a concentration of 5.90×10^{11} cfu/ml. Control (no pipe) to a concentration of 6.00×10^8 cfu/ml. Asterisks indicate the three days where data out of the countable range was used. These were consist with the trend.*
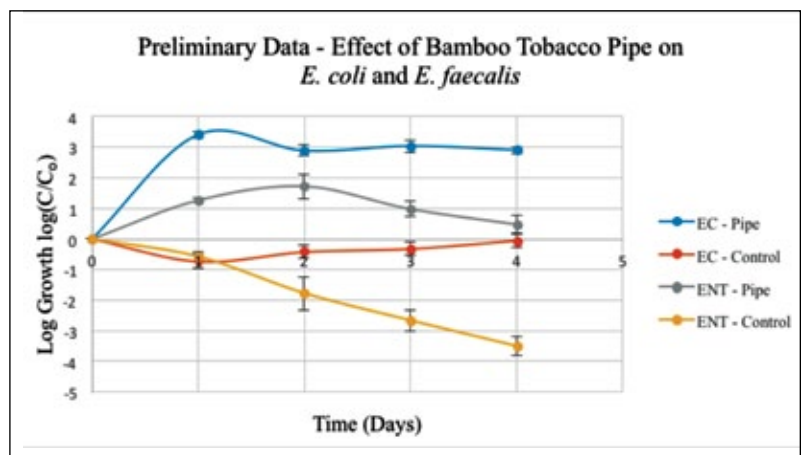

Figure 5. *Preliminary data displaying the effect of bamboo tobacco pipe vs. control on Escherichia coli and Enterococcus faecalis concentration over time. Graph shows the average log growth of three preliminary trials.*

the effects of different users on the microbial population in the water, the manner in which the pipes are stored, changes in environmental conditions and their effects on the bacterial growth, and other factors.
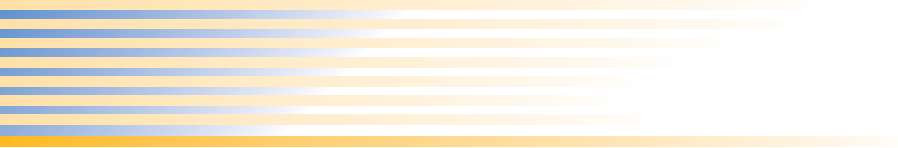
Preliminary experiments using *Enterococcus faecalis*, another fecal indicator microorganism, indicate that different microorganisms react differently to the presence of the pipe material (Figure 5). *E. faecalis* growth showed a similar trend to that of *E. coli*, however, the growth rate was less rapid. This demonstrates the need to continue this research in order to assess the relationship between the effects of tobacco bamboo pipes on the behavior of different microorganisms. Our plan is to conduct further, longer-term studies using *E. faecalis* to test the effect of tobacco bamboo pipe on the growth of this bacterium.

However, there are numerous pathogens that could be transmitted in this system, and we do not know how representative our results are. Therefore, further research should be conducted to determine if pathogenic bacteria such as *Mycobacterium tuberculosis*, *Staphylococcus aureus*, *Streptococcus pneumonia* and *pharyngitis* can grow in the pipe and, if so, to what extent. These pathogenic bacteria are known to cause respiratory infections, pneumonia, toxic shock syndrome, and sinusitis (13), and as such have the potential to be transmitted via smoking tobacco using the bamboo pipes.

Contaminated water poses the risk of spreading enteric diseases while the shared use of the pipe introduces the possibility of spreading respiratory and various diseases. Together, the contaminated water and the rapid growth of bacteria in the pipe demonstrate the necessity of further experiments, as well as the increasing awareness of and providing education to communities for the prevention of water contamination and safe practices for the use of tobacco water pipes. Because the use of bamboo tobacco pipes remains a tradition, measures such as treating water with chlorine tablets or using sand filters to remove microbial contaminants from the water may be practical strategies to reduce risk of infection (14). In addition, measures to prevent cross-contamination from one person to another may also need to be developed. The establishment of guidelines for the safe use of these pipes can potentially be applied to other smoking practices, such as hookah lounges, artificial cigarettes and any other liquid inhalation apparatus.

REFERENCES

1. Lauper, B. "Tobacco and Its Use in Asia." Field Museum of Anthropology. Department of Anthropology 1924. <http://archive.org/stream/tobaccoitsuseina18lauf/tobaccoitsuseina18lauf_djvu.txt>. (accessed: April 16, 2014).

2. Thomas, R.J. , D. Webber, R. Hopkins, A. Frost, T. Laws, P.N. Jayasekera and T. Atkins. "The Cell Membrane as a Major Site of Damage During Aerosolization of *Escherichia coli*." *Applied & Environmental Microbiology* 77(3):920-925 (2011).

3. Dr. Ryan Sinclair, Loma Linda University, personal communication

4. Haack, S. "Fecal Indicator Bacteria and Sanitary Water Quality." USGS. U.S. Department of the Interior, U.S. Geological Survey Water Resources Division, Michigan District 2007. <http://mi.water.usgs.gov/h2oqual/BactHOWeb.html>

5. United States Environmental Protection Agency. "National Beach Guidance and Required Performance Criteria - Appendix 1c1: Indicator Organisms." Water: Beach Grants. 2013. <http://water.epa.gov/grants_funding/beachgrants/app1c.cfm>. (accessed: April 22, 2014)

6. United States Environmental Protection Agency. Method 1603: *Escherichia coli* (*E. coli*) in Water by Membrane Filtration Using Modified Membrane-Thermotolerant *Escherichia coli* Agar (Modified mTEC). Washington, DC (2009).

7. Hett, C. E., and J. E. Rubin. "Bacterial Growth and Cell Division: A Mycobacterial Perspective." *Applied & Environmental Microbiology* 72.126-156 (2014).

8. "Bdtm Phosphate Buffered Saline (Ph 7.2) Bdtm Saline Solution (0.9%) " 2003. <http://www.bd.com/europe/regulatory/Assets/IFU/HB/CE/BA/BA-257204.pdf>. (accessed: April 23, 2014)

9. Ilstrup, D M. "Statistical Methods in Microbiology." American Society for Microbiology 3.3 (2014): 219.

10. U.S Environmental Protection Agency. Method 1600: *Enterococci* in Water by Membrane Filtration Using Membrane-Enterococcus Indoxyl-B-D-Glucoside Agar (mEI). Washington, DC (2002).

11. Microsoft. Microsoft Excel. Redmond, Washington: Microsoft, 2014.

12. Sokal, Robert R., and F. James Rohlf. Biometry. 4th ed. San Francisco: Freeman, 1969.

13. Baorto, P. E. "Staphylococcus Aureus Infection." WebMD LLC 2014. (accessed April 22 2014)

14. «Regulating Public Water Systems and Contaminants under the Safe Drinking Water Act.» Water: Regulation Development. 2013. http://water.epa.gov/lawsregs/rulesregs/regulatingcontaminants/basicinformation.cfm>. (accessed: April 23, 2014)